SEARCHING FOR FIREBALL PRE-DETECTIONS IN SKY SURVEYS

(Spine Title: SEARCHING FOR FIREBALL PRE-DETECTIONS)

(Thesis format: Monograph)

by

David L. <u>Clark</u>

Graduate Program in Astronomy

A thesis submitted in partial fulfillment
of the requirements for the degree of
Master of Science

The School of Graduate and Postdoctoral Studies
The University of Western Ontario
London, Ontario, Canada

THE UNIVERSITY OF WESTERN ONTARIO

SCHOOL OF GRADUATE AND POSTDOCTORAL STUDIES

CERTIFICATE OF EXAMINATION

Supervisor   Examiners

_____   _____
Dr. Paul Wiegert   Dr. Peter Brown

                                                    _____
Supervisory Committee   Dr. Martin Houde

_____   _____
Dr. Peter Brown   Dr. Gordon Osinski

_____
Dr. Pauline Barmby

The thesis by

David L. Clark

entitled:

SEARCHING FOR FIREBALL PRE-DETECTIONS IN SKY SURVEYS

is accepted in partial fulfillment of the
requirements for the degree of
Master of Science

Date_____   _____
                                                    Chair of the Thesis Examination Board

ABSTRACT

The Fireball Retrieval on Survey Telescopic Image (FROSTI) project seeks to locate meteoroids on pre-existing sky survey images. Fireball detection systems, such as the University of Western Ontario's ASGARD system, provide fireball state vector information used to determine a pre-contact trajectory. This trajectory is utilized to search databases of sky survey image descriptions to identify serendipitous observations of the impactor within the hours prior to atmospheric contact. Commonly used analytic methods for meteoroid orbit determination proved insufficient in modeling meteoroid approach, so I have developed a RADAU based gravitational integrator. I have also developed code to represent the description of an arbitrary survey image in a survey independent fashion, with survey specific plug-ins periodically updating a centralized image description catalogue. Pre-processing of image descriptions supports an innovative image search strategy that easily accounts for arbitrary object and observer position and motion. Meteor event selection is described and search results are provided.

Keywords: meteor, meteoroid, pre-detection, sky survey, NEO, Near Earth Object, NEA, Near Earth Asteroid, modelling, frustum, image search.

ACKNOWLEDGEMENTS

Zdeněk Ceplecha et al. In addition, Dr. Spurný provided unpublished European Network meteor event data which contributed significantly to the pool of data with which I could work.

Finally, I thank my wife Angela for the patience and understanding as the venture into a Masters program consumed many hours of my time. I also thank Angela for her time in proof reading this thesis and its many supporting documents.

TABLE OF CONTENTS

LIST OF TABLES

LIST OF FIGURES

LIST OF SYMBOLS AND ABBREVIATIONS

α	Phase angle
α_R	Apparent right ascension of an object's radiant at atmospheric contact
a	Semimajor axis (orbital element)
A	Object albedo
ASGARD	All Sky and Guided Automatic Real-time Detection
$B(a,e,i,H)$	Observational bias function dependent on orbital elements an visual magnitude
C	Programming language, used for system software and portable application development
C++	Programming language, object-oriented evolution of C-language.
CFHT	Canada-France-Hawaii Telescope
CFHTLS	Canada-France-Hawaii Telescope Legacy Survey
ClearSky	Pre-existing astronomical simulation software, developed by the author and enhanced for the purposes of this project.
δ_R	Apparent declination of an object's radiant at atmospheric contact
Δ	Earth-object distance
$\Delta\varepsilon$	Nutation in obliquity
$\Delta\psi$	Nutation in longitude
Δt	The adjustment between Dynamical Time and Universal Time
D	Asteroid diameter
DE405	NASA JPL planetary position ephemerides available as tables of Chebyshev coefficients and supporting code
ε	Specific orbital energy
ε	True obliquity
ε_0	Mean obliquity
e	Eccentricity (orbital element)
$\vec{e}$	Eccentricity vector

f	True anomaly (orbital element)
FRM	Fast Rotating Model
FROSTI	Fireball Retrieval on Survey Telescopic Images
FTP	File Transfer Protocol
G	Slope parameter
GUI	Graphical User Interface
$\vec{h}$	Orbital angular momentum vector
H	Absolute magnitude
h_B	Geographic height of an object at the beginning of atmospheric interaction
HTTP	Hypertext Transfer Protocol
i	Inclination (orbital element)
IS	Intermediate source (of asteroids)
JD	Julian Day
λ_B	Geographic longitude of an object at the beginning of atmospheric interaction
L_{SUN}	Solar longitude
LINEAR	Lincoln Near Earth Asteroid Research (a search program)
LLSF	Linear Least Squares Fit
μ	Standard gravitational parameter
m	Visual magnitude
MILIG	Meteor Trajectory Solver code by Jiri Borovicka
MORB	A meteor orbit determination code by Ceplecha et al.
MORP	Meteor Observation and Recovery Project
MPC	Minor Planet Center
$\vec{n}$	Ascending node vector
n(a,e,i,H):	Magnitude and orbital element dependent frequency distribution
$N_{NEA}(H)$	Near Earth Asteroid magnitude frequency distribution
NEA	Near Earth Asteroid
NEAT	Near Earth Asteroid Tracking (a search program)
NEATM	Near Earth Asteroid Thermal Model

NEO	Near Earth Object
O(...)	The order of a method or algorithm, a measure of the number of operations as a function of the number of objects being manipulated (N). E.g. O(N), O(N^2), O(N log N).
$P(\alpha)$	Phase function over phase angle α
PFM	Pre-fireball meteoroid
r	Sun-object distance
$\vec{R}$	Position vector
$R_{NEA}(a,e,i)$	Relative Near Earth Asteroid distribution binned by orbital elements a, e and i
$R_{NEO}(a,e,i)$	Relative Near Earth Object distribution binned by orbital elements a, e and i
RADAU	A publically available numerical integrator which utilizes Gauss-Radau spacings for sequence sub-steps
SFD	Size frequency distribution
SMETS	Standard Meteor Trajectory Solver, code by Wayne Edwards
STM	Standard Thermal Model
T	Time
TAI	International Atomic Time
TD	Dynamical Time
TDB	Barycentric Dynamical Time
TDT	Terrestrial Dynamical Time
USNO	United States Naval Observatory
USNO A2.0	USNO stellar database
UT	Universal Time
v_∞	Geocentric object velocity at atmospheric contact
$\vec{V}$	Velocity vector
φ_B	Geographic latitude of an object at the beginning of atmospheric interaction
WGS84	World Geodetic System 1984, a standard coordinate frame and spheroid model for the Earth

Ω	Longitude of the ascending node (orbital element)
ω	Argument of perihelion (orbital element)

1 INTRODUCTION

The association of in-space and in-atmosphere images provides a unique opportunity to correlate results from different observation and modelling techniques. In-space and in-atmosphere observations both directly and indirectly yield conclusions as to object size, composition and dynamics. With the two observations of the same object, one is able confirm consistency, or highlight discrepancies, in existing methods. One would hope as well that the discovery of a pre-fireball meteoroid (PFM) would add to the understanding of the visual properties of Earth-impacting objects. The discovery of a PFM in space would serve to confirm or suggest refinements to methods used to calculate heliocentric orbits from fireball observations.

When work began on the FROSTI project in the summer of 2007, there had not been a single fireball object that had both been recorded in space on its approach to Earth, and recorded in the atmosphere as a fireball. The goal of FROSTI is to discover such dual observations through a systematic search of historical sky survey images for objects detected in all-sky camera systems. The initial data sets targeted were the fireball observations from the University of Western Ontario's All Sky and Guided Automatic Real-time Detection system ASGARD (Weryk, et al., 2008), Weryk (2009), and the Canada-France-Hawaii Telescope Legacy Survey (CFHTLS) image catalogue (CFHT, 2009). A lofty goal of FROSTI was to be the first to relate in-space and in-atmosphere observations of a common object. However, that accomplishment was met with the pre-contact discovery of object 2008 TC3 by the Catalina Sky Survey (Jenniskens, et al., 2009) prior to the object's atmospheric entry over Sudan, and its subsequent meteorite deposit. Regardless, the FROSTI project continued with the intent to systematically arrive at further like observations.

Figure 1-1 provides an overview of the original project as first conceived. Existing code within the ASGARD system would provide Keplerian orbital

elements and related error bars for a number of fireball objects. A probability cloud of probable objects would be generated, with each cloud point having orbital elements taken from the calculated orbit adjusted by random selections from the various orbital element error bars. The probability point positions would then be calculated back over the prior 48 hours using standard Keplerian to heliocentric rectangular conversions. The rectangular coordinate positions at each time step would be checked against an image catalogue. A simple asteroidal magnitude model would be used to gauge visibility of each cloud point within an image. The time frame of 48 hours was selected as an arbitrary first guess when all objects would cease to be visible in the CFHTLS.
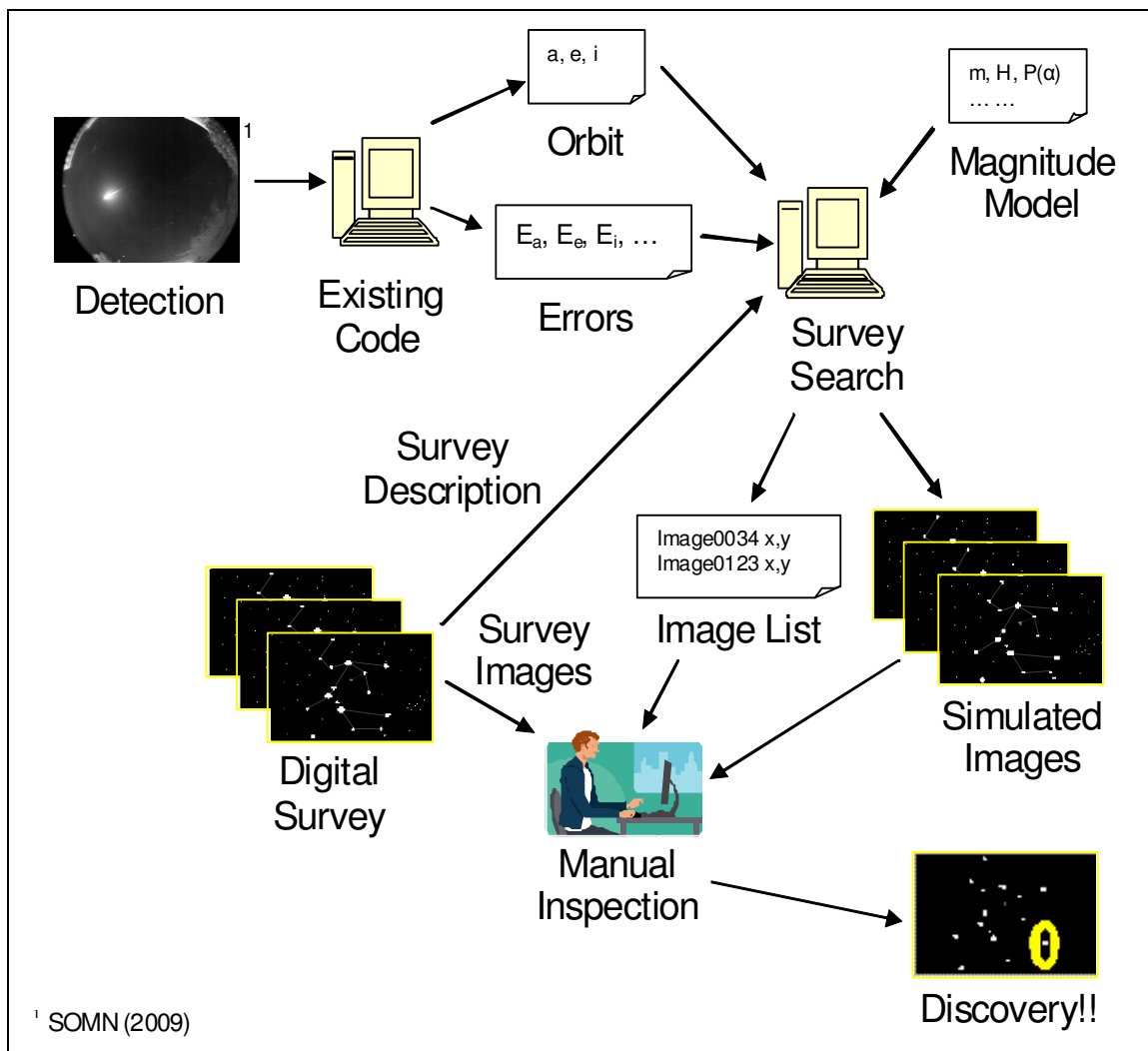
Figure 1-1. The original project plan.

The project was originally imagined as a three phase project: 1) Understanding of the problem including understanding of existing codes used by ASGARD and the data ASGARD provides, the modelling of PFM visibility using asteroidal models, and the availability of image description data; 2) Implementation and execution of ASGARD object searches against CFHTLS images; and 3) the automation of the entire process. It is important to note that the initial Phase 2 search of catalogue images is a catalogue search only, highlighting intersections of object positions and image fields, not the actual search of the images themselves for the appearance of the object. This more sophisticated image content search was considered a Phase 3 automation objective. Early work on the project quickly demonstrated that the overall project effort would be larger than expected for a number of reasons described below. In the interest of time, the effort to automate the process was limited to development of steps that could be easily orchestrated, and did not include the searching of candidate image content for evidence of the objects.

Modelling of PFM visibility evolved from a simple application of asteroidal magnitude models and a simple statement of the viability of detecting PFMs, to thorough simulations utilizing pre-existing NEA dynamical models and pre-existing meteoroid size frequency distributions. Chapter 2 is a review of the literature studied to better model the PFM size frequency distribution, and to justify the usage of NEA and asteroidal models to predict the probability of success in discovering PFM pre-detection images. Chapter 3 describes in detail both the early simplistic modelling done to reassure that success may be possible and the more detailed modeling based on prior NEA and meteor works. One significant outcome of the modelling was the realization that the original thought of capturing images in the 48 hour priors was somewhat optimistic, and that I needed to concentrate on periods of time closer to the time of contact. A second major finding was that the restricted ASGARD and CFHTLS based program was unlikely to yield success, but with numbers tantalizing enough to

continue with generalized approaches that could yield results with the inclusion of more meteor detection and sky survey systems.

The outputs from ASGARD, and software tools used by it, proved insufficient for accurate determination of a PFM trajectory near the Earth. This is not a statement of shortcoming in these systems, but simply a result of utilizing data in a manner which was beyond the intent of these systems. Chapter 4 describes the issues encountered with the orbits generated by ASGARD through the MORB meteor orbit determination code (documented as FIRBAL in (Ceplecha Z. , 1987). An exhaustive description of the calculations used to arrive at heliocentric contact state is provided. The chapter also describes the gravitational integration work required to replace MORB, and the methods used to complement ASGARD in acquiring appropriate initial meteor state to drive this integration.

Chapter 5 discusses the image description search technique developed for this project. The viewing frustum, the three-dimensional volume of space covered by an observer's view of a scene, is a long-used computer scene rendering tool which allows world objects positions to be transformed and clipped to a viewing port. I have adapted this tool by representing images as frustums, facilitating a significant shift of computation from image search time to front-end image download time. The pre-calculating of image presence in heliocentric space and time yields a data base of image frustums which greatly reduces the object-image intersection computation effort. A side benefit to this approach is the availability of the pre-processed image description database for use by other projects. I explain the mathematics of the approach in sufficient detail to show that the problem of image intersection can be reduced to a small number of computational steps at search time. I also briefly describe the image download process and the data organization around the constructed image catalogue.

Chapter 6 provides a brief description of my pre-existing astronomical simulation software ClearSky, and describes the major functionality added in support of this project. This description ties together the modelling, gravitational integration, and image searching pieces discussed in previous chapters.

Chapter 7 summarizes the results of the project. Although we have yet to discover a survey image of a meteoroid, there have been several achievements in using orbit determination and image searching functionality as stand-alone tools. I provide survey effectiveness results for a number meteor and meteor collections, presented as case studies.

Chapter 8 draws conclusions from the results, and speaks to possible future work stemming from this project.

2 LITERATURE REVIEW

2.1 Introduction

The search for fireball pre-detection images in sky surveys is an event-driven process; a fireball is observed, an approach trajectory is calculated, and sky survey databases are searched. The modelling of pre-fireball meteoroids (PFMs) yields an expected frequency of fireball meteoroids sufficiently large to support discovery, and provides guidance as to a reasonable degree of automation for the search process. This literature review discusses existing literature relevant to the modelling of the pre-fireball meteoroid size frequency distribution and the detectability of these objects. The modeling of potential success in searching for PFM images in sky surveys involves several different factors: 1) the true size frequency distribution (SFD) of PFMs, considering both absolute numbers and frequency of Earth collision, 2) the visibility of these meteoroids based on their physical properties, and 3) the sky coverage and sensitivity of the sky surveys. These factors cannot be analysed in total independence of each other. The PFM SFD is both based on assumed PFM physical properties and our understanding of observational selection effects of sky surveys. The visibility of a PFM is dependent on its physical properties. Long-term solar system dynamics affect the SFD of PFMs and as well as the orbital distribution, the latter impacting visibility through dependencies on orbit parameters and velocity.

2.2 The Size Frequency Distribution of PFMs

This review of object SFD literature starts with works that specifically target meteoroid frequency and detectability. It then transitions to literature pertaining to Near Earth Asteroid (NEA) work, where we assume extrapolations of NEA models may be made to infer PFM population characteristics.

2.2.1 The Fireball SFD

Early works on meteor flux rates include Halliday et al. (1984), an informative summary of the flux estimates to that date. They reported on observations from the Meteorite Observation and Recovery Project (MORP), concluding with the flux estimate:

$$log\,N = -0.689\,log\,m + 2.967, \qquad (1)$$

where N is the number of events producing a total mass of meteorites on the ground exceeding m grams in 10^6 km^2 in 1 year. Halliday et al. plotted, compared, and reasoned differences among their results and the results of previous work by Hawkins (1960), Brown (1960), Millard (1963), McCrosky and Ceplecha (1969) and Hughes (1981) (See Figure 2-1).
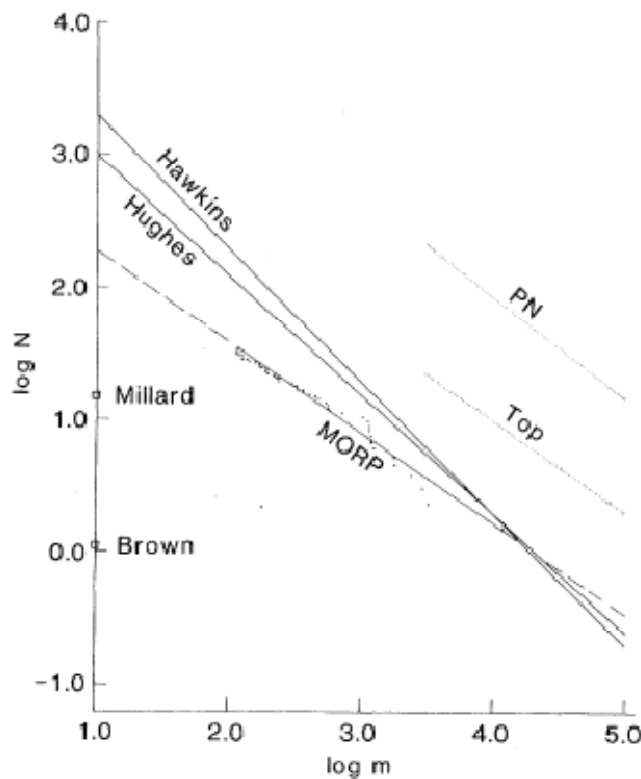
Figure 2-1. The Halliday et al. (1984) meteorite size frequency distribution. Plot of log N versus log m, where N is the number of events per year in 10^6 km^2 with mass exceeding m grams. The instrumental results presented here are labeled "MORP"; the distributions derived by Hawkins (1960) and by Hughes (1981) and the frequencies published by Brown (1960) and by Millard (1963) are shown for comparison. All of these refer to meteorite masses on the ground. Dashed portions of the MORP line are extrapolations beyond the observed mass range. The dotted line labeled "Top" indicates the flux entering the atmosphere for those fireballs that produce meteorites on the ground, while the line labeled "PN" is the estimate of the total flux entering the atmosphere from Prairie Network data (McCrosky & Ceplecha, 1969). Halliday et al. (1984). (The PN curve is significantly higher due to both the inclusion of non-meteorite producing fireballs and an over-estimation of mass due to a low luminous efficiency being used).

Halliday at al. (1996) provided an analysis of 259 fireball MORP events from 1971 to 1985. They stepped through the calculation of photometric mass (the mass lost to ablation) and initial mass, yielding mathematical expressions for cumulative frequency (N) based on initial masses (MI). Table 2-1 lists these expressions, Table 2-2 provides representative values of cumulative frequency, and Figure 2-2 plots the associated fluxes. Of note is a step in the slope of the log N vs. log MI plot at 2.4 kg. Halliday et al. discussed and then discounted this step being due to underestimated magnitudes of bright objects, concluding the reduced frequency of larger objects is real. Brown et al. (2002) converted the Halliday results to total Earth area frequency by bolide energy and plotted this data against other flux estimations in Figure 2-3.

All fireballs,	2.4 to 12 kg,	$\log N = -1.06 \log MI + 5.26$
All fireballs,	0.1 to 2.4 kg,	$\log N = -0.48 \log MI + 3.30$
Meteorites,	2.0 to 25 kg,	$\log N = -0.87 \log MI + 4.09$
Asteroidal,	2.7 to 12 kg,	$\log N = -1.00 \log MI + 4.92$
Asteroidal,	0.1 to 2.7 kg,	$\log N = -0.50 \log MI + 3.20$
Cometary,	0.05 to 4 kg,	$\log N = -0.60 \log MI + 3.15$
Shower,	0.1 to 4 kg,	$\log N = -0.65 \log MI + 2.37$
Fast,	0.008 to 0.125 kg	$\log N = -0.66 \log MI + 2.47$

MI	All Fireballs		"Probable Meteorites"		Asteroidal		Cometary		Meteor Showers	
0.1	220	(5)			160	(8)	89	(9)	12	(10)
0.3	130	(5)	–		92	(8)	46	(9)	5.8	(10)
1.0	72	(5)	–		50	(8)	22	(9)	2.6	(10)
3.0	38	(4)	12	(6)	28	(7)	12	(9)	0.6	(10)
10.0	10	(4)	4	(6)	8	(7)	–		–	

Table 2-1. The mathematical expressions for the cumulative frequencies (N) with the range of values of initial mass (MI in grams) over which each expression may be used. Halliday et al. (1996)

Table 2-2. Frequency, N, of preatmospheric masses larger than MI (kg) per 10^6 km^2 per year for several types of fireballs. Halliday et al. (1996)

ReVelle (2001a) arrived at estimates of large bolide flux utilizing infrasonic data on 19 objects collected from 1960-1974 and 1995-2001. ReVelle introduced source energy prediction methods available at the time, concluding on the use of a semi-empirical yield-period relationship method of Olmstead and Leies(1978). ReVelle arrived at the relationship:

$$N(E \geq E_s) = 5.66 \cdot E_S^{-0.724}, \quad r^2 = 0.954, \tag{2}$$

where N is the cumulative number of bolides colliding with the Earth per year of source energy greater than or equal to E_s in kilotons, and r is the correlation coefficient of the fit. Predicted global influxes by source energy are listed in

Source Energy, E_s: kt	Number, N, per year at the Earth	Cumulative Number, N' $\geq E_s$	Standard statistical counting errors
1100	0.05	1	± 0.05
30	0.18	2	± 0.13
26	0.30	3	± 0.17
20	0.434	4	± 0.22
14	0.63	5	± 0.28
11	1.24	6	± 0.51
10	1.55	8	± 0.55
9.86	2.21	9	± 0.74
8	1.26	10	± 0.40
6	2.51	11	± 0.76
2.5	4.58	12	± 1.32
0.84	8.04	13	± 2.23
0.29	12.8	14	± 3.43
0.21	16.2	15	± 4.18
0.20	32.3	16	± 8.06
0.112	23.6	17	± 5.74
0.11	23.7	18	± 5.58
0.053	33.1	19	± 7.59

Table 2-3. Bolide Infrasound Data and the Predicted Global Influx Rate

(Cumulative number of bolides per year at the Earth whose source energy exceeds Es) as well as standard, statistical counting errors, i.e., ± N/{N}1/2. ReVelle (2001a).

Table 2-3. Brown et al. (2002) plotted this data against other flux estimations in Figure 2-3, and comment on the higher infrasound estimates.

In a concise summation of original and prior work, Brown et al. (2002) reported on the total Earth flux of large bolides (or "small near-Earth objects"), for which 300 optical flashes were detected by United States Department of Defence and Department of Energy space based systems. Optical energies were calibrated against source energies in thirteen situations where independent estimates of event energies had been derived. Brown et al. arrived at a power-law fit for total energy E (in kilotons) and N, the cumulative number of objects colliding with the Earth per year with total energy $\geq E$:

$$log\ N = a_0 - b_0\ log\ E \qquad (3)$$

where $a_0 = 0.5677 \pm 0.015$ and $b_0 = 0.90 \pm 0.03$. The consistency of slope with the Halliday et al. (1996) findings is evident as E varies with MI. In Figure 2-3, Brown et al. plotted the Halliday et al. flux expressed in terms of diameter and energy in relation to their power-law, along with the infrasound based estimates by ReVelle (2001a), the lunar crater flux (Werner, Harris, Neukum, & Ivanov, 2002), and telescopic survey based estimates from LINEAR: (Stuart, 2001) (referenced as Stewart) and (Harris A. W., 2002), and Spacewatch and NEAT: (Rabinowitz, Helin, Lawrence, & Pravdo, 2000). Good correlation is evident.

Figure 2-2. Plots of the flux at the top of the atmosphere showing log N vs. log Ml. N is the cumulative number of events per 10^6 km^2 per year with mass equal to or greater than Ml (in grams). The solid line represents data for all fireballs. Dashed lines represent subgroups as follows: AA = asteroidal group; CC = cometary group; MM = meteorite-dropping objects; SS = shower meteors; FF = fast meteors with entry velocity 40 km s or more. - Halliday et al. (1996)
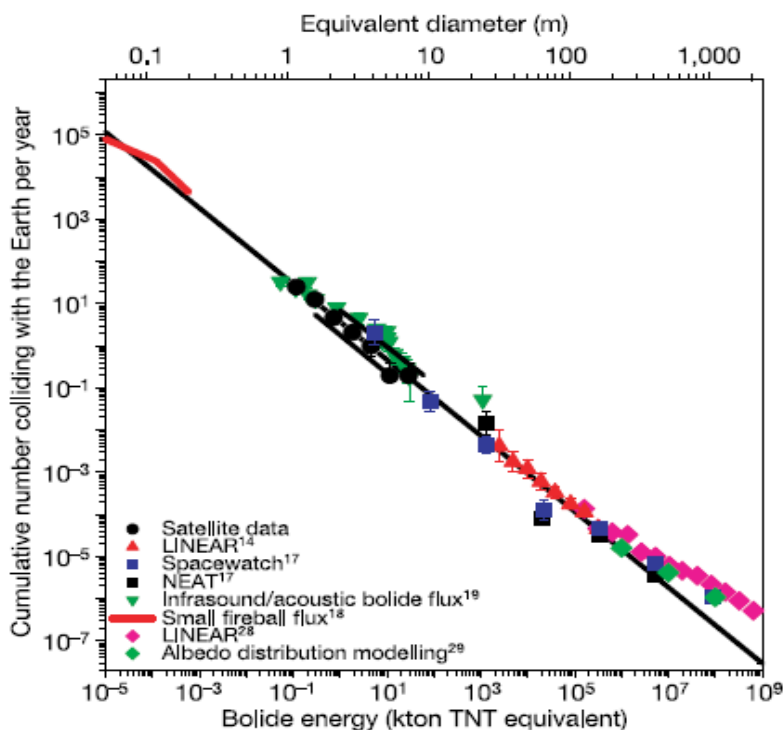
Figure 2-3. The flux of small near-Earth objects colliding with the Earth. Data are shown over a range of 14 magnitudes of energy. The fireball flux from Halliday et al. (1996) is at the upper left. – Brown et al. (2002)

2.2.2 The NEA SFD

The Brown et al. (2002) work leads to the observation that it is reasonable to utilize research on the NEA SFD to model the PFM distribution. Much of the

literature on the NEA SFD arrived at estimates on the number of NEAs (Table 2-5) and the expected frequency of Tunguska like impacts (Table 2-6), but it is the underlying development and refinement of an SFD and orbital characteristic models that are of greater importance to a PFM detection project.

Morrison et al. (1994), in "The Impact Hazard", provided an insightful study of impact effects from the perspective of mortality risk. The section titled "Impact Flux" listed several references to earlier works on lunar cratering rates, along with newer (at the time) work based on estimates of Near Earth Object and long period comet populations and dynamical life-times (see Table 2-4).

Shoemaker et al. (1979)	Earth-crossing asteroids - Orbital classes, collision rates with earth, and origin. In: Asteroids.
Shoemaker and Wolfe (1982)	Cratering time scales for the Galilean satellites.
Weissman (1982)	Cometary impacts on the terrestrial planets.
Wetherill and Shoemaker (1982)	Collisions of astronomically observable bodies with the Earth.
Shoemaker (1983)	Asteroid and comet bombardment of the Earth.
Shoemaker et al. (1988) (referred to as 1990 in Morrison et al.)	Asteroid and Comet Flux in the Neighborhood of the Earth
Wetherill (1989)	Cratering of the terrestrial planets by Apollo objects.
Weissman (1991)	Cometary impactor flux at the Earth.
Ceplecha (1992) (title incorrect in Morrison et al.)	Influx of interplanetary bodies onto Earth.
Rabinowitz et al. (1994)	Chapter in: Hazards due to comets and asteroids.
Shoemaker et al. (1994)	Chapter in: Hazards due to comets and asteroids.

Table 2-4. A list of references and titles of works on lunar cratering rates from Morrison et al. (1994).

Bottke et al. (2000) referred to works by Morrison (1992) and Rabinowitz et al. (1994) and speak to their early estimates of the existence of 1000-2000 NEAs of absolute magnitude H<18 (diameter > 1 km). Later estimates of an NEA population and SFD involved the analysis of the efficiencies or biases of sky surveys combined with the modelling of fictitious asteroid populations. Bottke et al. (2000) documented the building of a representative NEA population, integrating forward fictitious objects originating from three intermediate sources (IS's), regions which continuously are fed main asteroid belt material: (1) asteroids in the 3:1 mean motion resonance with Jupiter, (2) asteroids in the v_6 secular resonance (where the rate of precession of the asteroids perihelion is

one sixth the secular frequency of the solar system), and (3) asteroids in Mars-crossing orbits adjacent to the main belt. Bottke et al. binned the *a,e,i* space and tracked the duration of time the representative objects from each IS spent in each bin, thereby giving a steady state relative distribution $R_{NEA}(a,e,i)$ over these bins. By combining this binning with the known magnitude dependent bias function $B(a,e,i,H)$ of the Spacewatch system (Jedicke, 1996) (Jedicke & Metcalfe, 1998) (Durda, Greenberg, & Jedicke, 1998), and fitting a predicted Spacewatch magnitude frequency distribution *n(a,e,i,H)*:

$$n(a, e, i, H) = B_{NEA}(a, e, i, H)R_{NEA}(a, e, i)N_{NEA}(H) \qquad (4)$$

to actual Spacewatch observations, Bottke at al. developed an absolute magnitude distribution:

$$N_{NEA} = C \times 10^{\gamma(H-13)} \qquad (5)$$

where: γ = 0.35 ± 0.02 and C = 13.26. The R_{NEA} distribution is of interest in modelling the smaller PFMs regardless of whether the N_{NEA} magnitude distribution is used. Bottke et al. arrived at an estimate of NEAs of H<18 of approximately 910 (-120, +200). In a later work (Bottke, et al., 2002a), two additional intermediate source regions were added to the model: the outer main belt population and the ecliptic comet population dominated by Jupiter-family comets. With the addition of a cometary source, a switch to the terminology NEO (Near-Earth Object) from NEA occurred. A refined R_{NEO} is developed, and a revised estimate for NEOs of H<18 is given as ~ 960 ± 120. The Bottke et al. (2002a) distribution provides an excellent basis for simulating PFM orbital distributions in the study of visibility as it pertains to object position and motion.

Morbidelli et al. (2002a) adjusted the estimate of NEOs over 1 km size down to 855 ± 110 based on the observation that the long-used conversion of H = 18 ⇔ D = 1 km was incorrect. They based this argument on observed

albedo distributions of large asteroids in the NEO source regions, extrapolating these distributions to smaller asteroids. They adjusted the H⇔D relationship to H = 17.85 ± 0.03 ⇔ D = 1 km.

Rabinowitz et al. (2000) proposed a markedly decreased estimate of NEAs (700 ± 230) based on the results of the NEAT (Near-Earth Asteroid Tracking) program. Rabinowitz et al. spoke to the prior Spacewatch analyses, Rabinowitz (1993) and Rabinowitz (1994), as not being normalized due to uncertainties in the detection efficiency of that system.

Stuart (2001) utilized the LINEAR Survey to arrive at a >=1 km NEA population size of 1227 (+170, -90), larger than the Bottke et al. estimates, and significantly larger than the Rabinowitz et al. estimate. Stuart questioned the Rabinowitz et al. estimate based on their small sample size (significantly less than the number of *a,e,i* bins used), and the resulting assumptions on orbital parameters that were made. Stuart rationalized that the higher Bottke et al. (2000a) estimate is due to a questionable coupling of semi-major axis and inclination in the Bottke model, where NEAs of a < 1.8 AU have higher inclinations than those with a > 2 AU. Stuart concluded with a derived cumulative H magnitude distribution of:

$$N(< H) = 10^{-3.88 + 0.39H} \qquad (6)$$

Harris (2002) built on the Stuart (2001) work by extending his size curve down to magnitude H = 25.5 from 22.5, thereby including Tunguska-sized objects (H ~ 24.0 – 24.5). He derived an estimate of 500,000 objects in this size range, with an expected Earth impact frequency of once per 1000 years, with an uncertainty of a factor of 3.

Werner et al. (2002) demonstrated that the lunar crater SFD leads to a projectile estimate quite consistent with NEA search program based estimates.

Werner et al. utilized the lunar crater models of Neukum (1983) and Neukum and Ivanov (1994) with updates from Ivanov et al. (1999) and (2001) utilizing a method by Schmidt and Housen (1987) to convert the lunar crater SFD into a projectile SFD. They derived a lunar impact probability for objects of diameter ≥ 1km of 1.3 (± 0.2) x 10^{-7} impacts per year. Dividing this count by the average probability of impact per asteroid of 1.86 ± (0.04) x 10^{-10}, as determined by the formulas of Öpik (1951) and revised by Wetherill (1967), Werner et al. arrived at a projectile of diameter ≥ 1km population of 700 ± 130.

Quoted "earlier estimates"	1000 - 2000
Bottke et al. (2000)	~910 (+100,-120)
Rabinowitz et al. (2000)	700 ± 230
Stuart (2001)	1227 (+170,-90)
Bottke et al. (2002a)	~960 ± 120
Morbidelli et al (2002a)	855 ± 110
Werner et al. (2002)	700 ± 130

Table 2-5. Estimates of NEA populations where H<18 (approximately 1km in diameter)

Shoemaker (1983)	300 years
Harris (2002)	1000 (accurate to a factor of 3)
Brown et al. (2002)	400-1800 years

Table 2-6. Estimates of Tunguska-like impact frequency

In conclusion, the literature on fireball and NEA (or NEO) SFD shows that the various models are not in complete agreement, but that it is reasonable to model PFM dynamics and population through a combination of NEA simulations such as Bottke et al. (2002a) or Stuart (2001), and a size distribution such as the Brown et al. (2002) distribution. This combination of models supports the setting of expectations for both the pre-contact detectability of the meteoroids and the frequency of fireball events that may trigger a survey search.

2.3 The Physical Properties of PFMs

The physical properties of PFMs, and by extension NEAs, affect the modelling of PFM detection in several ways: 1) the relating of fireball intensity to meteoroid mass, 2) the understanding of the delivery mechanisms of NEAs and PFMs and therefore the PFM SFD, and 3) the visibility and therefore detectability of PFMs in sky surveys.

2.3.1 Fireball Processes and PFM mass

Of great importance to both the modeling of PFM visibility, and the selection of events for reasonableness in survey searches, is the determination of the PFM mass from video meteor observations. Brown et al. (2002) began their paper with a discussion on assumptions made to derive a PFM mass from an in-space detected optical flash. Similar issues apply with ground-based observations. Assumptions must be made on the spectrum of the bolide, the fraction of kinetic energy converted to light, the bolide velocity, and its density. Object velocities are directly available by ground-based observation or through modelling the PFM SFD, but all other assumptions relate to physical properties of the object, and the processes in play on the object.

Brown et al. first assumed a 6000º K black body spectral distribution, as used in prior work by Tagliaferri et al. (1994). Ceplecha et al. (1998) provided a thorough summary of atmospheric interaction models, with which they discuss and tabulate prior spectral work and comment on there being no one temperature or known process that leads to the observed spectra. Brown et al. acknowledged the shortcoming of the black body assumption, but consider the resulting error in estimated flux to be acceptable.

The determination of object mass by optical measurement requires a good estimate of the fraction of the initial object kinetic energy converted into light, termed luminous efficiency. In Brown et al. (2002), the luminous efficiency of their bolide population is derived by fitting luminosity to total kinetic energy for a subset of the events where the kinetic energy was derived by other means (infrasound, measured velocities, multi-station photos, retrieved meteorites, observed spectra). ReVelle (1980) presented an integral approach to the problem of determining fireball mass and behaviour from observed fireball properties. ReVelle provided a summary of previous approaches and the difficulty in their use due to a microphysical approach: Öpik (1933), Whipple (1942), Öpik (1958), McKinley (1961), and Kovshun (1977). Ceplecha et al.

(1998) summarized the discussion and works on luminosity of meteors, and commented more than once on the ReVelle work significantly correcting prior views on initial mass and luminous efficiency.   Pecina and Koten (2009) provided a systematic computation of meteoroid mass from video recorded meteors. Although concerned with smaller objects than PFMs, the application of their work appears relevant to the estimation of PFM size and therefore visibility. The role of deceleration in absorbing kinetic energy is discussed often in the literature. Ceplecha et al. (1998) cautioned that deceleration needs to be considered. The amount of energy consumed in deceleration is significant for larger masses at lower velocities, with the $\frac{dv}{dt}$ term being factored by the mass and velocity, while the $\frac{dm}{dt}$ term is factored by the square of the velocity. Halliday et al. (1996) also speak to deceleration being a dominant factor at low velocities. Pecina and Koten (2009) noted that it is not typically a factor with video meteors, but do discuss the appropriate adjustments.

Fragmentation plays a significant role in the ablation process, and therefore needs be understood in determining PFM mass. Ceplecha (1994) documented a classification of meteoroids based on prior observations (NF = no gross fragmentation, 1F = one point of sudden overwhelming fragmentation, MF = many points of fragmentation). Prior to this time, most ablation work was based on a single body theory. ReVelle (2001b) examined the "pancake" fragmentation process, a catastrophic fragmentation previously assumed for large meteoroid cases. ReVelle determined that pancake fragmentation is not a contributing process for meteoroids of diameter up to one metre. Ceplecha and ReVelle (2005) describe a fragmentation model and code implementation that handles fragmentation into both large fragments and a cluster of small fragments. The application of their model to the Lost City bolide event results in a derivation of luminous efficiency as a function of object velocity, mass, and air density.

2.3.2 The Meteor-PFM-NEO-Asteroid Association

The association of meteors to parent asteroidal bodies is very much related to the goal of a PFM search project, the association of a fireball event with an in-space image of the impacting object. Binzel et al (2002) explained the wide interest in NEO properties. The NEO population is known to require a replenishment process, and with NEOs being a precursor to meteors, the understanding of NEO properties provides a link between known meteorite properties and asteroidal spectral observations. Binzel et al. tabulated the group, classification, size, albedo, rotational characteristics and NIR spectral data for asteroidal NEOs. This list is maintained online at http://earn.dlr.de/nea/ (Hahn, 2009). The online list provides original source documentation for each object. In discussion of this list, Binzel et al. referred to or credited prior works by several authors (see Table 2-7).

Chapman et al. (1994)	Physical Properties of Near-earth Asteroids: Implications for the Hazard Issue.
Lupishko and Di Martino (1998)	Physical properties of near-Earth asteroids.
Wisniewski et al. (1997)	Photometric Observations of 125 Asteroids.
Binzel et al. (1998)	Size Dependence of Asteroid Spectral Properties: SMASS Results for Near-Earth and Main-Belt Asteroids.
Binzel et al. (2001)	Spectral Properties of Near-Earth Objects: Palomar and IRTF Results for 48 Objects Including Spacecraft Targets (9969) Braille and (10302) 1989 ML.
Erikson et al. (2000)	The Near-Earth Objects Follow-up Program III.
Hammergren (1998)	The Composition of Near-Earth Objects.
Pravec et al. (2000)	Fast Rotating Asteroids 1999 TY_2, 1999 SF_{10}, and 1998 WB_2.
Rabinowitz (1998)	Size and Orbit Dependent Trends in the Reflectance Colors of Earth-Approaching Asteroids.
Hicks et al. (1998)	The Unusual Spectra of 15 Near-Earth Asteroids and Extinct Comet Candidates.
Hicks et al. (2000)	Physical Observations of 1996 PW and 1997 SE5: Extinct Comets or D-Type Asteroids?
Whiteley and Tholen (1999)	The UH Near-Earth Asteroid Composition Survey: an Update.
Whiteley (2001)	A compositional and dynamical survey of the near-Earth asteroids.

Table 2-7. A list of references and titles of works on asteroidal characteristics from Binzel et al (2002).

Binzel et al. discussed the taxonomy of NEOs referring to works on delivery process: Bottke et al.(2002a), (2002b), Morbidelli et al. (2002b), and the higher albedo of S-type NEOs, and phase effects: Luu and Jewitt (1989),

Muinonen et al. (2002). They also discussed the relationship of NEOs to comets, the relationship of NEOs to ordinary chondrite meteorites, the shape and rotation of NEOs, orbital properties, and surface structures.

Group	Fall Percentage (%)*	Postulated Parent or Source Bodies†
L	38.0	S(IV) asteroids (*Gaffey et al.*, 1993)
H	34.1	6 Hebe [S(IV)] (*Gaffey and Gilbert*, 1998)
LL	7.9	S(IV) asteroids (*Gaffey et al.*, 1993)
Irons	4.2	M asteroids (*Cloutis et al.*, 1990; *Magri et al.*, 1999)
Eucrites	2.7	4 Vesta (V) (*Consolmagno and Drake*, 1977; *Drake*, 2001)
Howardites	2.1	4 Vesta (V) (*Consolmagno and Drake*, 1977; *Drake*, 2001)
CM	1.7	19 Fortuna (G, Ch) (*Burbine*, 1998)
Diogenites	1.2	4 Vesta (V) (*Consolmagno and Drake*, 1977; *Drake*, 2001)
Aubrites	1.0	3103 Eger (E) (*Gaffey et al.*, 1992)
EH	0.8	M asteroids (*Gaffey and McCord*, 1978)
EL	0.7	M asteroids (*Gaffey and McCord*, 1978)
Mesosiderites	0.7	M asteroids (*Gaffey et al.*, 1993)
CV	0.6	K asteroids (*Bell*, 1988)
CI	0.5	C asteroids (*Gaffey and McCord*, 1978)
CO	0.5	221 Eos (K) (*Bell*, 1988)
Pallasites	0.5	A asteroids (*Cruikshank and Hartmann*, 1984; *Lucey et al.*, 1998)
Ureilites	0.5	S asteroids (*Gaffey et al.*, 1993)
"Martian"	0.4	Mars (*McSween*, 1994)
CR	0.3	C asteroids (*Hiroi et al.*, 1996)
CK	0.3	C asteroids (*Gaffey and McCord*, 1978)
Acapulcoites	0.1	S asteroids (*McCoy et al.*, 2000)
Angrites	0.1	S asteroids (*Burbine et al.*, 2001a)
Lodranites	0.1	S asteroids (*Gaffey et al.*, 1993; *McCoy et al.*, 2000)
R	0.1	A or S asteroids
Winonaites	0.1	S asteroids (*Gaffey et al.*, 1993)
(Tagish Lake)‡	0.1	D asteroids (*Hiroi et al.*, 2001)
Brachinites	Only finds	A asteroids (*Cruikshank and Hartmann*, 1984; *Sunshine et al.*, 1998)
CH	Only finds	C or M asteroids
"Lunar"	Only finds	Moon (*Warren*, 1994)

*Fall percentages are calculated from the 942 classified falls that are listed in *Grady* (2000), *Grossman* (2000), and *Grossman and Zipfel* (2001).

†Asteroid classes are a combination of those of *Tholen* (1984), *Gaffey et al.* (1993), and *Bus* (1999).

‡Tagish Lake is a newly discovered type of carbonaceous chondrite (*Brown et al.*, 2000) and is listed in the table because of its spectral similarity to D asteroids.

Table 2-8. Meteorite Groups and their postulated parent or source bodies. Burbine et al. (2002)

Burbine et al. (2002) detailed the number of meteorite to parent body connections established to that date, carefully explaining that for the most part, "parent body" refers to primordial asteroids and not the heavily fragmented current asteroidal population. Burbine et al. stated that the meteorites collected to that time represent approximately 100 distinct parental bodies. A list of such connections with originating authors is presented in Table 2-8.

Burbine et al. summarized advances in the understanding of the dynamics in the delivery of asteroidal material into the Earth region, referring to the works of Wetherill (1985), Greenberg and Nolen (1989), Farinella et al. (1994), Gladman et al. (1997), Morbidelli and Gladman (1998), Morbidelli et al. (2002b), Bottke et al. (2002b), ending with the observation that meteoroid flux is dominated by large asteroid collisional ejecta, and not material from small asteroids (based on SFD work of Durda et al. (1998) and findings of Bottke et al. (2002b). With numerous references to support their work, Burbine et al. described in detail the proposed meteorite to asteroid linkages: ordinary chondrites to S-type asteroids, CM chondrites to C-type, basaltic achondrites (HEDs) to 4 Vesta, and iron meteorites and enstatite chondrites to M-type.

2.3.3 Albedo, Phase Effects and Visibility

The albedo of asteroids, NEOs and PFMs directly leads to our understanding of the SFD of these object populations, and plays an obvious role in object detectability. Linking object size and albedo corresponding to a visual magnitude requires an understanding of the thermal and optical processes at play. As explained by Lebofsky and Spencer (1989), a large dark object and a small bright object may exhibit the same visual magnitude. However, the larger object will emit more thermal energy. An iterative algorithm may be used to determine an object's size (and albedo) from visual and thermal emissions (See Figure 2-4). Lebofsky and Spencer stepped the reader through the thermal models considered at the time: the Standard Thermal Model (STM) assuming a non-rotating object, the Fast-Rotating (or Isothermal Latitude) Model (FRM), and the Thermophysical Model which effectively parameterizes the continuum between the STM and the FRM. The STM involves a beaming parameter η which accounts for objects not radiating all their heat in the day direction and the fact that emissions are not isotropic.
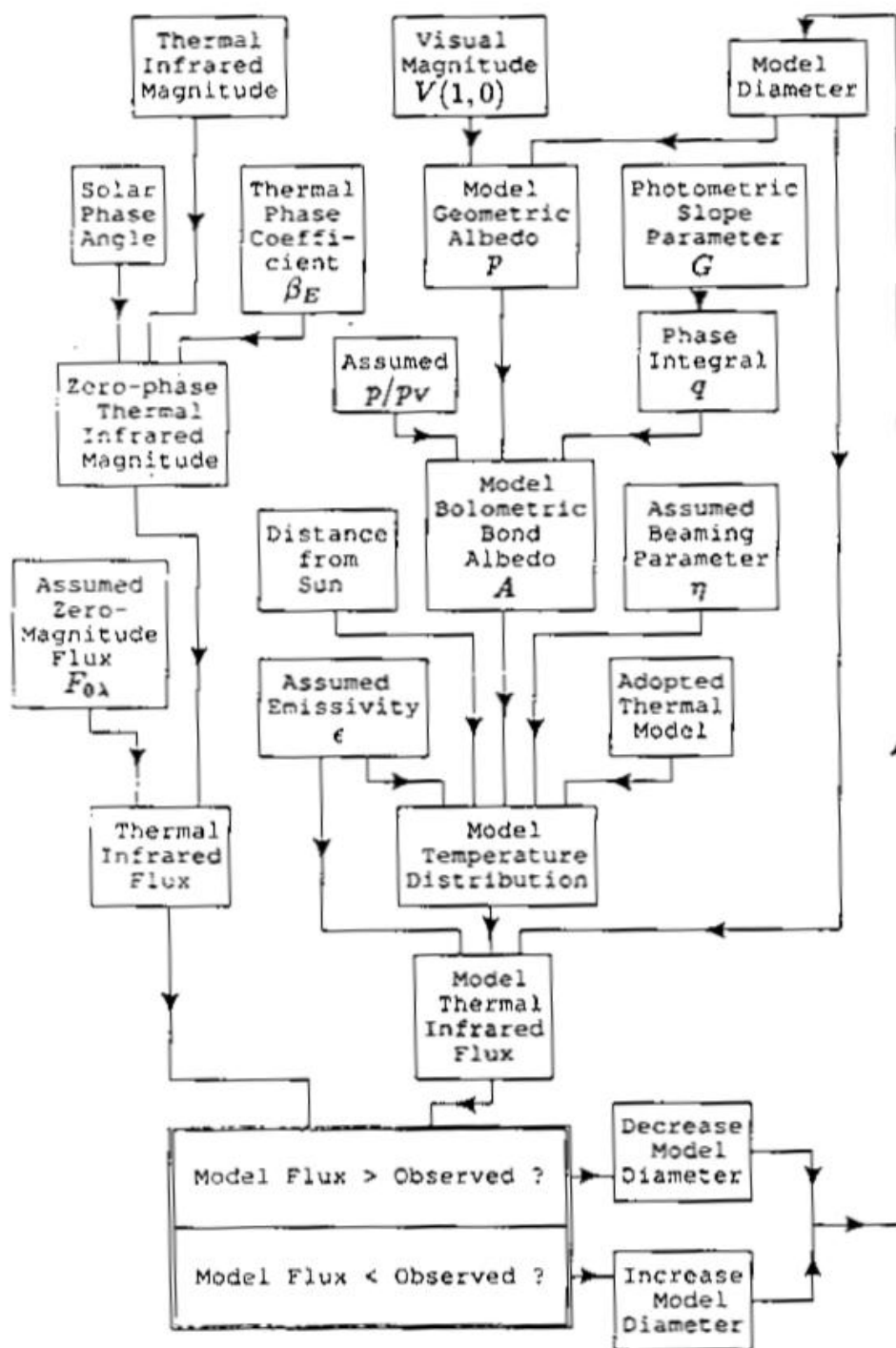
Figure 2-4. The steps required to determine a radiometric diameter from the observations of a body's visual and thermal radiation. V(1,0) is the V magnitude corrected to zero phase and to distances from the Sun and Earth of 1 AU. An initial guess at the model diameter is required, and the process is iterated until the thermal flux of the model converges to the observed value, using Newton/Raphson or similar techniques. Lebofsky and Spencer (1989)

Harris (1998) utilized IR data from six NEAs to develop a refinement of the STM as it pertains to NEAs. The NEA Thermal Model (NEATM) is effectively an STM with $\eta \sim 1.2$ where $\eta = 0.757$ for the asteroidal population. Harris and Davies (1999) utilized NEATM against NEAs to both confirm the validity of the model, and to arrive at new NEA diameter estimates. Kim et al (2003), in their work on the utilization of asteroids for far-infrared flux calibration, provided a very readable summary of asteroid thermal modelling.

Morbidelli et al. (2002a) described a detailed approach to determining an albedo distribution of NEOs. Utilizing the Bottke et al. (2002a) orbital element binnings and source region model, and varying the background threshold values of a Statistical Asteroid Model (Tedesco & Gradie, 2002) by comparing various background threshold levels to fit Sloan Digital Sky Survey results (Ivezić, et al., 2001), Morbidelli et al. arrived at an NEO albedo distribution for five albedo classes, and developed a new NEO size distribution over *a,e,i.* The albedo classes used are defined in Tedesco et al. as high, moderate, intermediate and low, with Morbidelli et al. adding a fifth cometary source class.

Of particular interest to the modelling of PFMs and in the detectability of a PFM in a sky survey of defined magnitude limitations, is the impact of phase angle on an object's apparent magnitude. The IAU adopted standard for calculating an asteroid apparent magnitude *m* based on the object absolute magnitude *H* as stated in Bowell et al. (1989) is:

$$m = H + 5log_{10}(r\Delta) + P(\propto) \tag{7}$$

where *r* and *Δ* are heliocentric and geocentric distances to the asteroid and *P(α)* is the phase function over phase angle *α:*

$$P(\propto) = -2.5log_{10}((1-G)\phi_1 + G\phi_2) \tag{8}$$

where:

$$\phi_1 = e^{-3.33(\tan\left(\frac{\alpha}{2}\right))^{0.63}}, \qquad \phi_2 = e^{-1.87(\tan\left(\frac{\alpha}{2}\right))^{1.22}}$$

and G is the slope parameter, a measure of change in object magnitude under differing illumination angles. As described in Morbidelli et al. (2002a), G is smaller for low-albedo objects than for high albedo objects, i.e. the phase angle effect is albedo-dependent. Morbidelli et al. list G based on albedo class as:

- $G = 0.13$ to the Cometary class,
- $G = 0.15$ to the Low class,
- $G = 0.18$ to the Intermediate class,
- $G = 0.25$ to the Moderate class, and
- $G = 0.40$ to the High class.

Luu and Jewitt (1989) studied the albedo-dependent phase angle in relation to the ratio of C-type to S-Type asteroids (the C:S ratio), as NEOs are often observed at large phase angles. Jedicke et al. (2002) graphically presented the dependency in Figure 2-5.
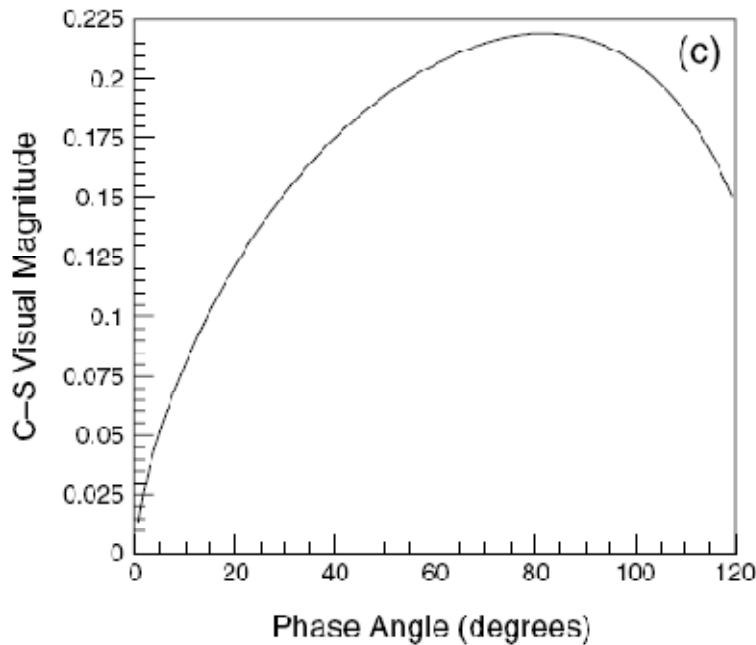
Figure 2-5. Difference in apparent visual magnitude between a C-type and S-type asteroid of the same absolute magnitude as a function of the phase angle. Jedicke et al. (2002)

Opposition effects on object magnitude and reflected light polarization are of significant importance in understanding the surface characteristics of asteroids (and by extension NEOs and PFMs). Muinonen et al. (2002) provided an in-

depth review of the observations of these affects, models used to explain them, and future prospects for research. They discussed the contributions of two light scattering mechanisms: the traditional shadowing-mechanism (SM) and the more recently proposed coherent backscattering mechanism (CBM). They referred the reader to the works of Muinonen (1994) and Shkuratov et al. (1994) for background on these models. Figure 2-6 demonstrates the observed spike in magnitude and reversal of polarization angle observed at low angles.
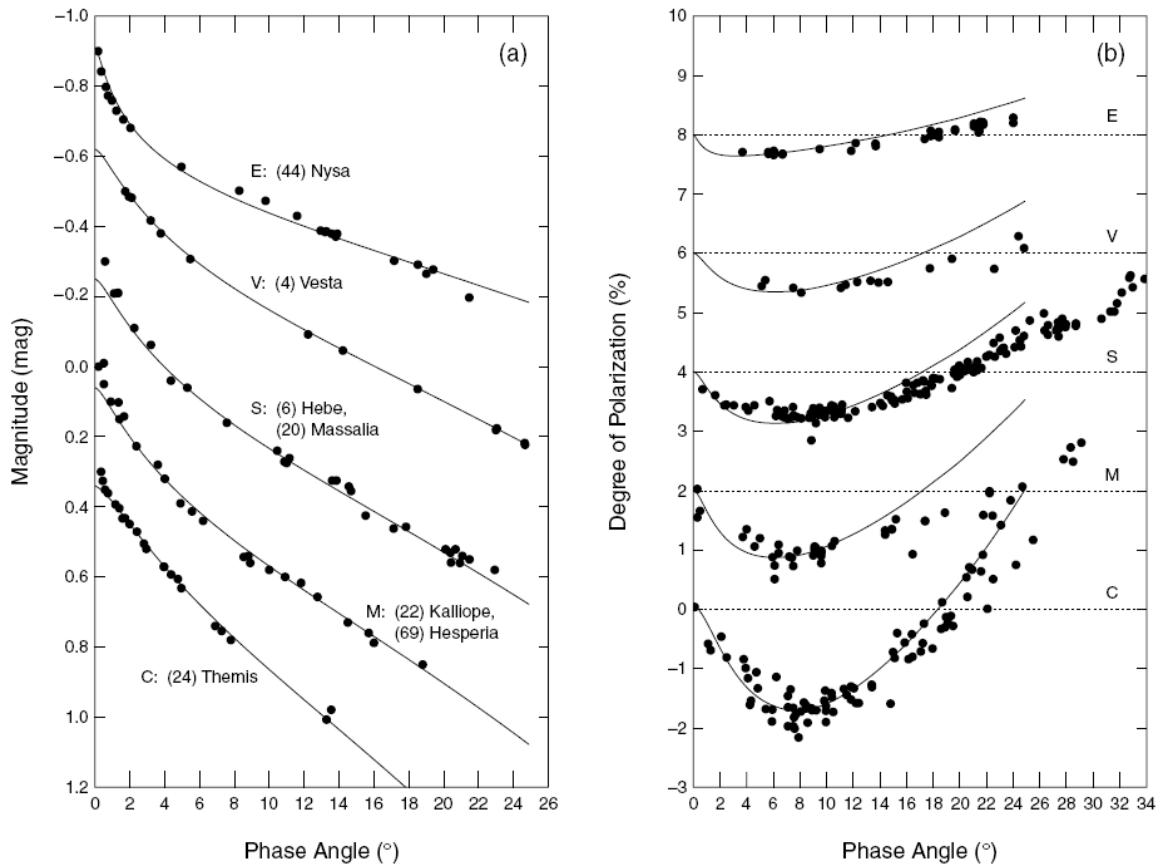
Figure 2-6. (a) Opposition effect and (b) negative linear polarization observations for C-, M-, S-, V-, and E-class asteroids. For illustration, the opposition effects are presented on a relative magnitude scale, and the negative polarizations of M-, S-, V-, and E-class asteroids have been shifted upward by 2, 4, 6, and 8 vertical units respectively. The solid lines illustrate results from heuristic theoretical modeling. Muinonen et al. (2002)

2.4 Image Search Program Effectiveness

Sky survey equipment and search techniques introduce selection effects in the visibility of NEAs, and by assumed extension, PFMs. Biases arise over attributes such as object inclination, albedo, colour, and velocity. The sky region covered can yield preferential detection of certain dynamical classes of asteroids.

Stokes et al. (2002) provided a historical view of sky survey programs, giving technical equipment details and search strategies of these programs. They discussed the traditional assumption that searching near the ecliptic and at opposition is the most effective search strategy, and agree with the Jedicke (1996) conclusion that searching away from opposition is more effective for higher magnitude objects. Many of the works previously discussing the NEA SFD and NEA population, such as Bottke et al. (2000), Bottke et al. (2002a)), Rabinowitz et al. (2000), and Stuart (2001), relied on specific program biases to extend observed distributions to actual population estimates.

Jedicke et al. (2002) described in great detail the various selection effects of sky surveys: sky-plane distribution, trailing losses, stationary points (the point at where an objects ecliptic longitude motion is zero), magnitude cut-off, line-of-sight, inclination, phase angle, colour, and survey factors around observing techniques, equipment attributes and weather. Jedicke et al. contains a section on rather complex bias calculations, which they readily admitted "should be read through pragmatic glasses".

Chesley and Spahr (2004) also analysed the impact of orbit characteristics on visibility, adding a study of the time frame between detection and impact. Starting with the Bottke et al. (2000) distribution, they built a population of NEAs that exhibited consistent behaviour with prior studies, noting that that the most efficient search area for H = 18 impactors is at 60-90º solar elongation. They then simulated two sky surveys, one which simulated the

LINEAR survey, concentrating on high solar elongations (Opposition Survey), and one which concentrated on the 60-90º region mentioned above (Near-Sun Survey). In both cases the limiting magnitude is V_{lim} = 20. Figure 2-7 shows their results, where it is evident that the Near-Sun simulated survey is significantly more successful at detecting large impactors of $H < V_{lim}$.

In a brief paper on the linking of sky surveys with meteorite finds, Chapman and Harris (2009) speak to 4 m. object strikes such as 2008 TC_3 being annual events, and 1.5 m. strikes being monthly events. They state that current sky surveys are likely to detect 10% of either of these types of events. With further surveys coming on-line, such as Pan-STARRS and LSST, the success rate should increase to cover all monthly events occurring within the 35% of the sky being covered.
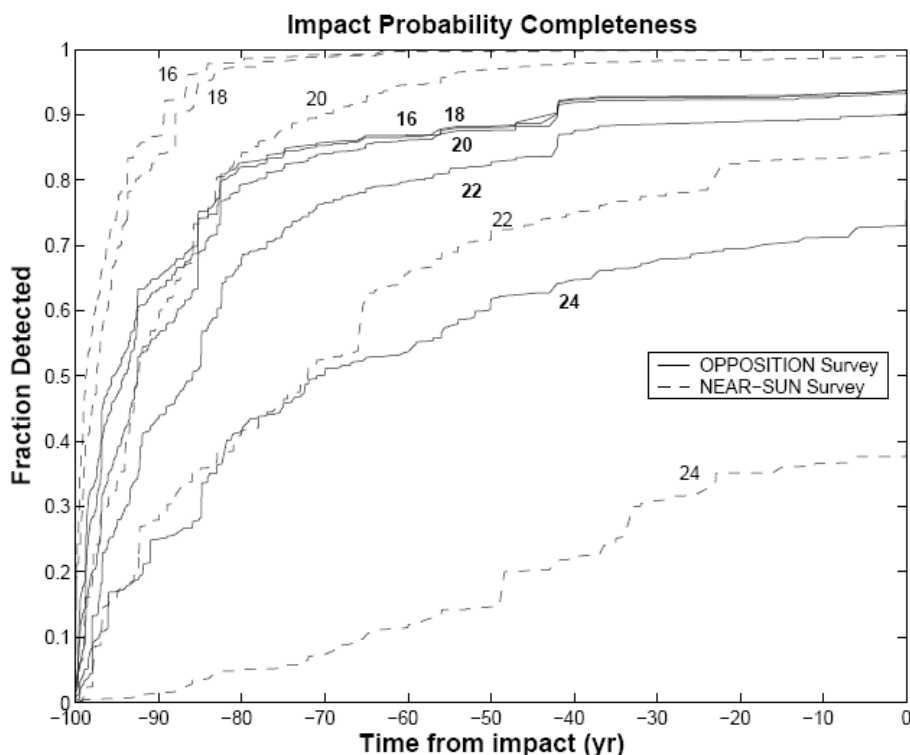
Figure 2-7. Comparison of OPPOSITION and NEAR-SUN survey performance, in terms of impact hazard completeness. Each curve is labeled with the assumed absolute magnitude. Chesley and Spahr (2004)

2.5 Summary

The collective literature on the fireball SFD, NEA SFD, albedo distribution and survey effectiveness provide sufficient theory to support the modelling of a PFM detection project. Methods are provided to model the PFM population complete with size, albedo and orbital parameter distributions. The literature appears to justify the utilization of NEA/NEO models for the purposes of PFM modelling. Finally, literature on the selection effects of surveys provides insight into modelling effectiveness of specific surveys in detecting modelled PFMs.

3 MODELLING METEOROID VISIBILITY

As alluded to earlier in the introduction to the literature view, the probability of success in discovering a pre-detection images is based on visibility of PFM's, their size distribution, and the probability of having observed a given event.

3.1 Primitive Modelling

The initial goal in modelling PFM visibility was to answer the question as to whether these objects are in fact visible for any significant duration of time prior to contact. Frequency distributions were not initially considered. PFM characteristics affecting visibility are size, distance from Earth and the Sun, phase angle, and albedo. Wiegert et al. (2007), extending on Bowell et al.(1989), document a relationship of asteroid diameter D in kilometres to absolute magnitude H_k and albedo A_k for colour filter k as:

$$D = \frac{1347 \times 10^{-H_k/5}}{A_k^{1/2}} \tag{9}$$

Disregarding colour filters, rearranging and combining with (7) and (8), and assuming a constant approach speed v such that:

$$\Delta = vt \tag{10}$$

for time t prior to contact, we derive a formula for apparent magnitude m as follows:

$$m = -5log_{10}(\frac{DA^{1/2}}{1347}) + 5log_{10}(rvt) - 2.5log_{10}((1-G)\phi_1 + G\phi_2 \tag{11}$$

where:

$$\phi_1 = e^{-3.33(\tan{(\frac{\alpha}{2})})^{0.63}}, \qquad \phi_2 = e^{-1.87(\tan(\frac{\alpha}{2}))^{1.22}}$$

We now have an expression for apparent magnitude in terms of object diameter (D) in metres, albedo (A), velocity (v) expressed consistently in units such that vt is in AU, phase angle (α) and time (t), as well as solar distance (r) and slope

parameter (*G*). Assuming *r* ~ 1 AU in the proximity of Earth, and *G* = .15 typical for low albedo asteroids (see Section 2.3.3), we are able to plot *m* against a sampling of reasonable *D*, *A*, *v* at *α* values, for various time periods.
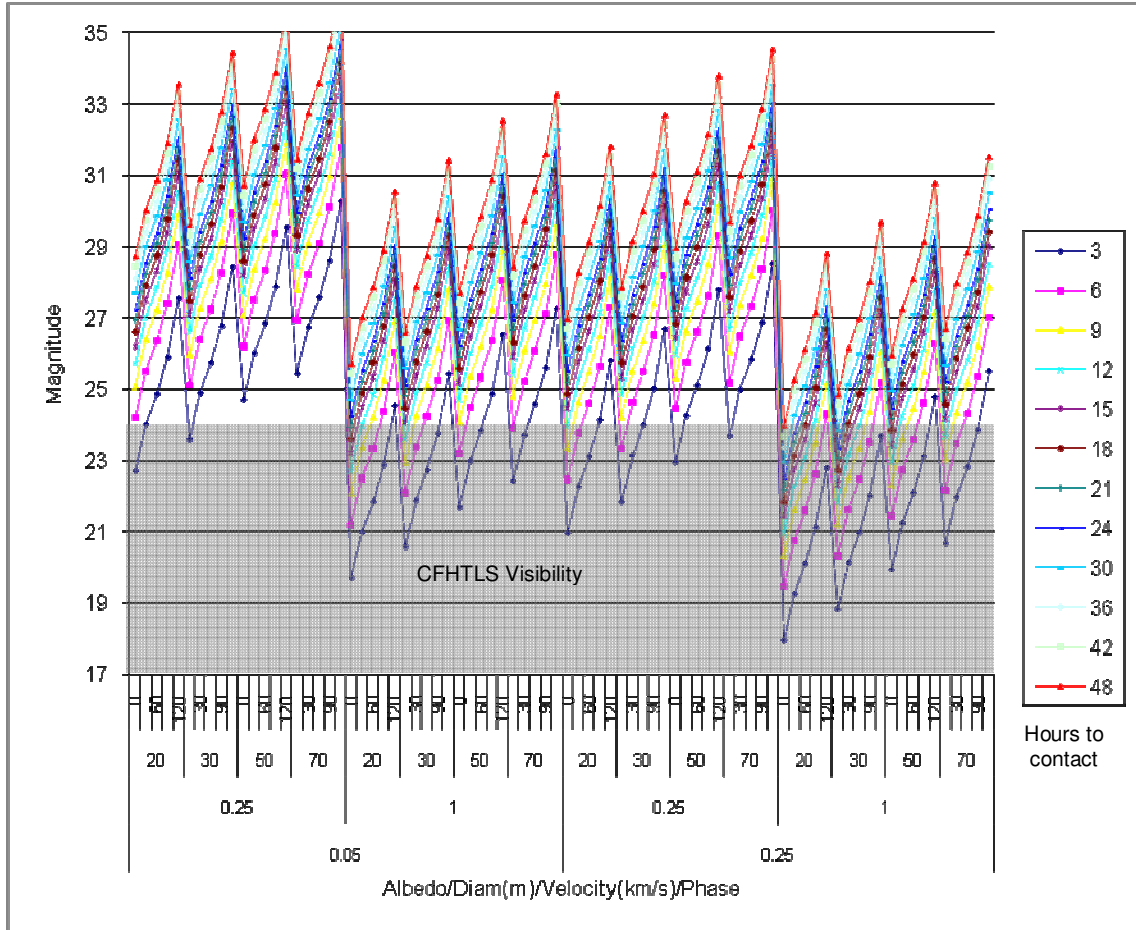
Figure 3-1. Plot of apparent magnitude over time of a variety of objects having albedo of 0.05 and 0.25, diameter of .25 and 1.0 metres, approach velocity of 20, 30, 50 and 70 kms^{-1}, and phase angle 0º, 30º, 60º, 90º and 120º, assuming linear approach. The gray shaded area represents visibility within the CFHTLS images. Lines join points of equal visibility duration. Trailing loss is not considered.

In Figure 3-1, visual magnitude is plotted for objects with *A* = 0.05 and 0.25, *D* = 0.25 and 1.0 metres, *v* = 20, 30, 50 and 70 kms^{-1}, and α = 0º, 30º, 60º, 90º and 120º at 3 hour intervals from 3 hours to 48 hours prior to contact. Symbols in the plot represent each time interval, with lines connecting points of like interval. The CFHTLS visibility limit of 24th magnitude is shown for comparison. One observes in the plot that there are indeed combinations of PFM physical and dynamical attributes which support predetections. In addition to the

expected favouring of higher albedo, larger diameter, slower speed, and lower phase angle objects, this plot demonstrates that very few objects remain visible for time periods in the range of the original project target of 48 hours, and that visibility ranges of 6-12 hours are what should be considered.

3.2 Bottke/Brown/Morbidelli Modelling

The simplistic modelling in section 3.1, although reassuring that object prediction images could exist, does not provide insight into the frequencies of objects with attributes permitting successful predetections.   The literature reviewed for Chapter 2 highlighted that pre-existing models for the relevant dynamical and physical attributes of PFMs were available, specifically NEA dynamical models of Bottke et al. (2002a), fireball size frequency distribution and flux model of Brown et al. (2002), and the albedo model of Morbidelli et al. (2002a). We use the Bottke et al. distribution as an estimate of a smaller body distribution, recognizing that the Yarkovsky effect on smaller bodies is not properly accounted for.

The Bottke 2002a NEA distribution is a 5-intermediate source model of NEA distribution binned over orbit semi-major axis (a), eccentricity (e), and inclination (i) (See section 2.2.2). 15,120 bins in total represent unique a, e, i combinations, where $a, e,$ and i vary as follows:

Element	#bins	Bin Width	Minimum Centre	Maximum Centre
a	42	0.10	0.05	4.15
e	20	0.05	0.025	0.975
i	18	5.0	2.5	87.5

The distribution of NEA's is represented as relative probability associated with each bin, where the sum of the bins is unity. In reality, the data as provided did not sum exactly to unity, so modelling code was adjusted to normalize to the actual sum.   The bins were pre-scanned, converting bin probabilities to

cumulative bin probabilities. The cumulative probability of a bin combined with the cumulative probability of the previous bin provide a range of 0 to 1 values for that bin which allows the bin to be selected with appropriate frequency from the simple generation of a uniform random number in the range 0 to 1. NEA model populations are generated by repetitively sampling from this distribution as follows:

For each of *a*, *e*, and *i*

1) Generate a uniform random number from 0 to 1.
2) Search the cumulative probability of *a*, *e*, or *i* bins for the bin containing the uniform random number.
3) Generate a uniform random number between the low and high values for that bin, giving the desired *a*, *e*, or *i* value.

Six Keplerian elements are required to define the orbit and position of an object at a given time. In addition to *a*, *e*, and *i*, values for longitude of the ascending node (Ω), the argument of perihelion (ω) and true anomaly (*f*) are required. In the case of the general NEA population, the three angles Ω, ω, and *f* may be uniformly selected from the full 0-360º range, as there is no natural anti-symmetric bias to these elements. However, PFMs are characterized within the NEA population as objects which have the immediate potential to collide with the Earth. A standard equation for Keplerian motion is:

$$r = \frac{a(1-e^2)}{1+e\cos f} \tag{12}$$

where *r* is the object-Sun distance. Re-arranging, we have:

$$f = \pm\cos^{-1}\frac{a(1-e^2)-r}{er} \tag{13}$$

Selecting a uniformly random time *t* in the time range of interest, we are able to determine *r* by assuming *r* *very* closely approximates the Earth-Sun distance. The Earth-Sun distance is readily available from published theories such as DE405 (NASA JPL planetary position ephemerides available as tables of Chebyshev coefficients and supporting code), which is used throughout this

work.   DE405 provides the Earth's position in heliocentric rectangular coordinates, but these are easily converted to distance *r* and heliocentric longitude (L).

Since the argument of perihelion ω is defined as an angle from the ecliptic, the circumstance of Earth-object collision occurs on the ecliptic, and *f* is defined as an angle from ω, we are able to determine ω from *f*. There are four possible relationships among *f*, ω, and Ω characterized by the object being at the ascending node or descending node, and whether the object is inbound or outbound in its orbit in relation to the Sun:

1) Ascending node, outbound: $f = \cos^{-1} ..., \omega = -f, \Omega = L$
2) Ascending node, inbound: $f = -\cos^{-1} ..., \omega = -f, \Omega = L$
3) Descending node, outbound: $f = \cos^{-1} ..., \omega = \pi - f, \Omega = \pi + L$
4) Descending node, inbound: $f = -\cos^{-1} ..., \omega = \pi - f, \Omega = \pi + L$

A uniform random distribution is used to select one of the four *f*, ω, Ω value combinations.

The above generation of PFM orbital elements refines two aspects of my earlier primitive modelling, eliminating the linear approach assumption, and providing a proper distribution of phase angles. Beginning at the time of Earth-object intersection, we are able to step back in time, calculating the distance and phase angle of each sample object at each time step.   However, neither the impact of object physical characteristics on the object visibility model, nor the need to model absolute frequencies, have yet been addressed. For these, we turn to the Brown et al. (2002) fireball flux work, and the Morbidelli et al (2002a) on the albedo distribution of NEOs. With equation (3), Brown et al. describe a power law for the cumulative number of objects (*N*) colliding with Earth per year with total energy ≥ *E.* They also express this power law in terms of cumulative number of objects with diameter ≥ *D* in metres as:

$$log\ N = c_0 - d_0\ log\ D \qquad\qquad (14)$$

where $c_0 = 1.568 \pm 0.03$ and $d_0 = 2.70 \pm 0.08$. Table 3-1 lists values for the relationship of D and N, highlighting the diameter range of interest, $0.2 - 1.0$ m.

D	N	D	N	D	N	D	N	D	N	D	N	D	N
10.0	0.07	7	0.19	4	0.88	1.0	37	0.7	97	0.4	439	0.1	1.85E+04
9.0	0.10	6	0.29	3	1.90	0.9	49	0.6	147	0.3	954	0.05	1.20E+05
8.0	0.13	5	0.48	2	5.69	0.8	68	0.5	240	0.2	2852	0.01	9.29E+06

Table 3-1. Tabulating the cumulative number of objects (N) colliding with Earth per year with diameter ≥ D in metres, as calculated from the Brown et al. (2002) formula (14).

From Table 3-1 we see an appropriate sample size for simulating $D \geq 0.2$m flux on the Earth would be approximately 2800 objects/year. This is not a large sample size at all when we consider that the samples are distributed over more than 15,000 *a, e, i* bins in the Bottke distribution, and still require some distribution over an albedo range. Therefore, the sample size used here will be substantially larger, with analysis adjusted back to this 2800 objects/year flux as appropriate. The actual generation of individual sample objects of $D \geq 0.2$m is accomplished by:

1) Generating a uniform random number *n* between 0 and 1.
2) Generating a sample diameter *D* as:

$$D = 0.2n^{1/d_0}$$

   where d_0 is -2.70 from (14).

With orbital properties and object size accounted for, we complete the modelling of the PFM population with albedo and slope parameter distributions from Morbidelli et al. (2002a). As discussed in 2.3.3, Morbidelli et al. define 5 NEO albedo classes: Hig(h), Mod(erate), Int(ermediate), Low, and Com(etary) with mean albedo for each, and albedo ranges for all but the Com class (for which we will assume the mean value for all samples). They then assign differing slope parameter values for each class to simulate a phase angle effect. Finally, they model a frequency distribution by class for the NEO population. Table 3-2

summarizes the mean albedo, albedo range, slope parameter and probability distribution into a single table, used to drive albedo (*A*) and slope parameter (*G*) generation as follows:

1) Generate a uniform random number between 0 and 1.
2) Locate the albedo class whose cumulative probability range contains the uniform random number.
3) Assign the class slope parameter to *G.*
4) Assign the mean albedo to A.

A more complete modeling could be done by randomly assigning albedos from an appropriate distribution within an albedo class. The shapes of these distributions are not immediately evident from the Morbidelli paper, so the simplified method of using the average albedo of each albedo class was used.

Class	Albedo Range	Mean Albedo	Slope Parameter	Probability	Cumulative Probability
Hig	0.355-0.526	0.462	0.40	0.10	0.10
Mod	0.112-0.355	0.197	0.25	0.65	0.75
Int	0.089-0.112	0.099	0.18	0.05	0.80
Low	0.020-0.089	0.055	0.15	0.14	0.94
Com	?(0.04-0.04)	0.04	0.13	0.06	1.00

Table 3-2. Albedo classes with corresponding albedo ranges, mean albedo, slope parameter and relative distribution. Summarized from Morbidelli et al. (2002a). An albedo range for Com class NEA's was not provided.

A sample of 10,000,000 objects was generated using the above NEA, bolide size and albedo models. This sample size is a compromise of reasonable required computation time against granularity of result binning. For the strict needs of visual magnitude analysis, a smaller sample size could be used. However, other analyses (below) were performed on the model which benefited from the increased sample size. Figure 3-2 shows the visual magnitude distribution of the sample objects plotted over various times from 5 minutes to 24 hours prior to Earth contact. As in the simple model of above, a significant portion of objects are potentially visible (magnitude < 24) in sky surveys in the minutes prior to contact. However, this visible proportion trails off very quickly in

the hours prior to contact, to the extent that almost none of the model population have visual magnitude less than 6 hours prior.
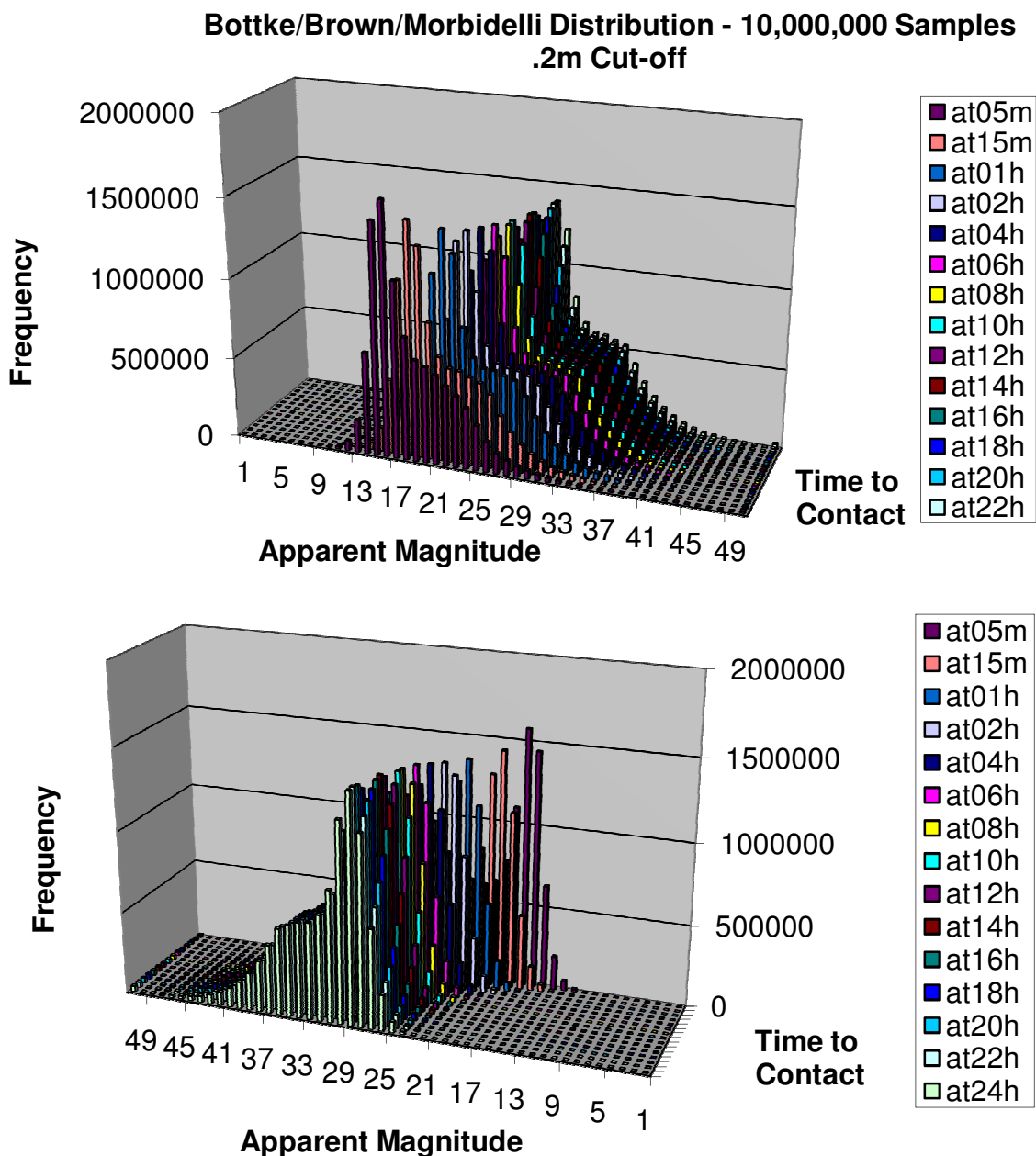
Figure 3-2. A visual magnitude plot of 10,000,000 simulated objects generated from the Bottke et al. (2002a) NEA distribution, the Brown et al. (2002) bolide size-frequency distribution, and the Morbidelli et al. (2002a) albedo distribution. Only objects above 0.2m in diameter are considered. Objects are selected by adjusting the argument of perihelion such that objects collide with Earth. The plot shows the number of objects falling into 1-magnitude wide bins over a series of time intervals prior to contact. Top: From foreground to background are the time intervals of 5 minutes, 15 minutes, 1 hour, and 2 hours to 24 hours in 2-hour increments. Bottom: The same plot with earlier times in the foreground.

Another output of the Bottke / Brown / Morbidelli modelling is the frequency distribution of the approach angles of the PFM population. The understanding of some unexpected asymmetries in this distribution could be considered for future work. A plot of the approach angle frequency distribution is provided in Appendix D – Approach Direction from Bottke / Brown / Morbidelli Modelling.

3.3 Detectability in ASGARD

With the Brown et al. (2002) SFD predicting approximately 2800 events/year of interest, we naturally turn to determining the expected frequency of such events being detected in ASGARD. A rigorous examination of this problem was deemed too large an exercise for this project, but is recognized as an area of possible future work. This effort would include an accurate computation of ASGARD sky coverage, weather factors, and a detailed analysis of the impact of PFM orbital dynamics, Earth orientation, and PFM physical properties on detectability. Assuming an accurate model for the ASGARD system, one could utilize the Bottke/Brown/Morbidelli modelling in section 3.2, sampling for objects entering the Earth's gravity influence, gravitationally integrating forward to Earth contact using the techniques in section 4.5, and testing for and modelling the resultant behaviour in the ASGARD (or any other meteor network) sky coverage area.

For the purpose of this project I use a personal conversation with Peter Brown (Brown (2009)) to arrive at a first order estimate on the fluence (or flux over time) of ASGARD corresponding to the 2800 objects/year flux. Brown estimates the ASGARD sky coverage to be 200,000 km^2, with approximately 15 hours/week of usable observing. When factoring in the surface area of the Earth (5.1×10^8 km^2), we arrive at an estimate of observed flux of candidate objects ($D \geq 0.2$ m) of:

$$N_{ASG}(D \geq 0.2) \cong 2800 \times \frac{15}{7 \times 24} \times \frac{2 \times 10^5}{5.1 \times 10^8} \cong 1 \times 10^{-1} yr^{-1} \qquad (15)$$

suggesting that candidate objects are decadal events. This flux estimate appears low in that two $D \geq 0.2$ metre events have occurred in the past 4 years: December 23, 2006 (Edwards, Brown, Weryk, & Revelle, 2008) and the recent September 25, 2009 Grimsby event. In deciding to continue with an image search of major ASGARD events as an exercise in both completeness and verification of a pessimistic but realistic expectation of success, the methods used are applicable to other camera networks, to satellite observations, and to the cross program data collections of meteor data such as the Virtual Meteor Observatory documented in Koschny et al. (2008) and Barentsen (2006).

3.4 Effectiveness of Sky Surveys

A successful discovery of a PFM requires the detection of the object in both a meteor observing system, and a sky survey. Independent of the sky coverage of a given survey over time, the characteristics of the object approach significantly impact the potential visibility of an object in a given survey. The determination of sky survey effectiveness is handled both on an object-by-object basis, and as a statistical study over a collection of events for a given meteor observing network. These analyses are automated by both object and object collection by network, using the calculated approach ephemerides described in Chapter 4. The results of these analyses are provided in Chapter 7. An evident pattern is the rather low effectiveness of current surveys based on approach characteristics and the limiting magnitude and observing field of the survey telescopes.

4 DETERMINATION OF METEOROID PATH

The search for a PFM in survey images requires a reasonably accurate determination of the PFM position over time. At project inception it was believed that the simple use of the orbital elements output by ASGARD would suffice. Error bars on the orbital elements would be used to generate a cloud of probability objects, each of which could be checked for image intersections. However, shortcomings in both in ASGARD output and a later questioning of the validity of using orbital elements, led to substantial unplanned work.

4.1 Issues with MORB Output

ASGARD determines the trajectory of a meteor expressed in an instantaneous geographic position, a radiant direction and a velocity magnitude. This trajectory is input into the MORB meteor orbit determination code (Ceplecha (1987)), which provides the PFM orbital elements at infinity and the associated error bars. 3D renderings of object and probability cloud positions quickly identified three major issues with the use of MORB orbital elements: lack of data precision, an extremely large probability cloud unsuitable for image searching, and an inappropriate convergence of the cloud towards the centre of the Earth.
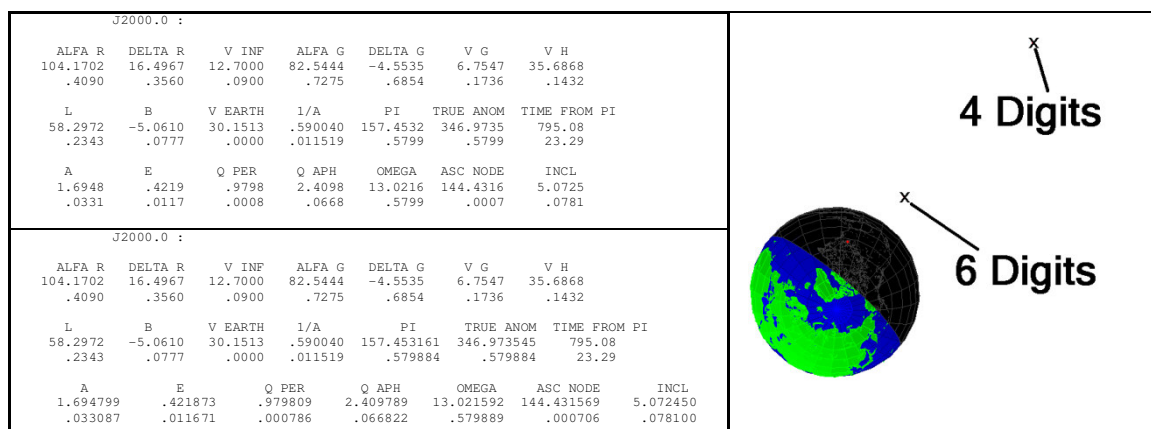
Figure 4-1. Sample output from MORB orbit determination program as used by ASGARD. Top left: original 4 digit orbital element output. Bottom left: Output modified for 6 digit output. In both cases, the second line of numbers are standard deviations around the mean value.   Right: Resulting positions of a sample object with orbital elements specified to 4 and 6 digits respectively.

Figure 4-1 illustrates an MORB output, both with the original 4 significant digits of orbital element output as used by ASGARD, and a modified 6 digit output, and the impact of 2 digits of orbital element significance on object position. This impact is easily understood when expressing the semi-major axis in terms of AU, where .00005 AU, the average error of 4 digit precision, is 7,500 km alone. Further analysis with 8 digit resolution reduced typical positional errors to the order of 100 km, although there was little confidence that such resolutions could be considered of value without a significant study of the MORB code and Ceplecha (1987) methods.

The significance of additional digits of precision hints at the even greater issue around the reported error bars from MORB. Orbital element error bars are calculated by MORB from the position and velocity vector error bars provided by ASGARD. Each error range for any one input coordinate is propagated across all orbital elements, yielding an orbital element error space significantly larger than is warranted by the inputs. For example, in the Figure 4-1 example, we see a standard deviation of .033 AU or 5×10^6 km in semi major axis. The significance of these large error bars is graphically demonstrated in Figure 4-2, showing 10,000 objects having orbital elements randomly selected from the reported MORB error bars. The resulting probability cloud dwarfs the lunar orbit, and is evidently of no use in directing an image search process.

A second attempt at utilizing MORB involved generating a random set of 1000 MORB inputs arrived at by sampling the input error bars. Each of these inputs resulted in a set of MORB orbital elements, which were then used to plot a probability cloud. With the expectation that 4-digit data precision would dominate the cloud size, 8 digits of precision were used for the experiment. Figure 4-3 demonstrates the resulting probability cloud size at 30 minutes and 2 minutes prior to Earth contact. The markedly reduced cloud size is evident. However, the observation is made that the probability cloud converges over time towards the centre of the Earth, and not towards the observing sight on the surface of the

Earth. At this point, the decision to abandon MORB as the orbit determination code was made, and attention turned to directly calculating Keplerian orbital elements directly from meteor positions and velocities output from ASGARD.
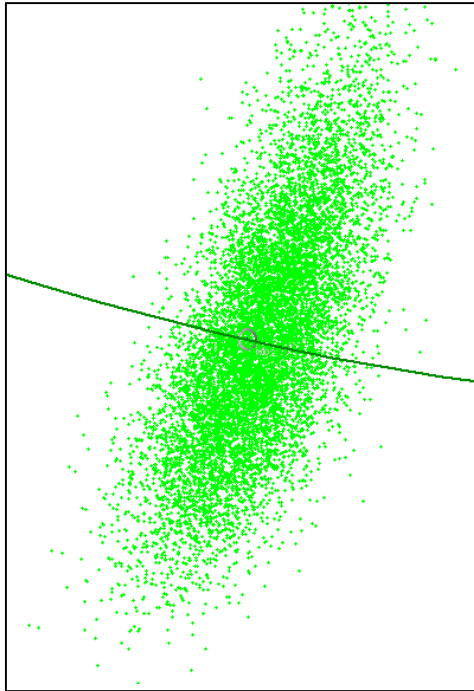
Figure 4-2. An illustration of 10000 probability points generated by randomly selecting orbital elements from sample MORB output error bars. The orbit of the Earth (left-to-right) and the Moon (inner circle) are depicted.
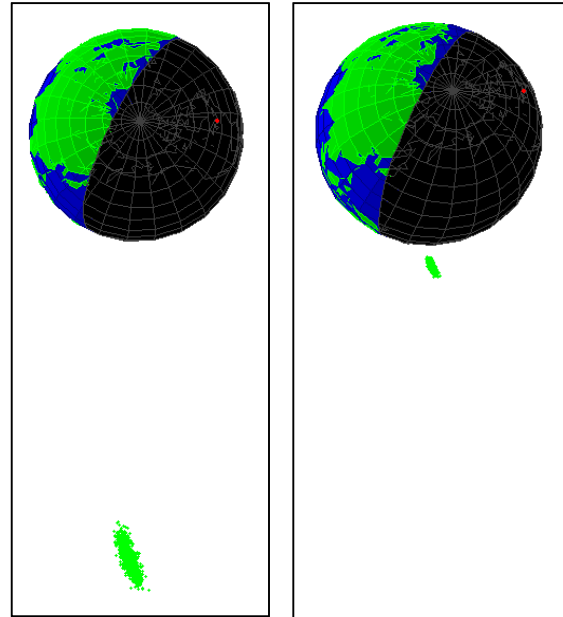
Figure 4-3. An illustration of 1000 probability points, generated by distributing position and velocity vectors across ASGARD error bars, feeding each resulting state into MORB to arrive at a set of orbital elements for each point. Left: 30 minutes prior to contact. Right: 2 minutes before contact. Note the convergence of probability points towards the centre of the Earth, and not towards the ASGARD location (red dot).

4.2 Issues with ASGARD Velocity Calculations

The exercise of extracting an instantaneous position and velocity at the top of the atmosphere from the ASGARD system is not straightforward. ASGARD calculates average velocities over portions of the meteor path as required by the Ceplecha (1987) method. These velocities are calculated independently for each observing station. In conversation with Rob Weryk, Dr. Wayne Edwards, and Dr. Peter Brown, it was decided the appropriate method to calculate the initial velocity vector is to perform a least squares fit of object movement through the initial non-decelerating portion of the observed trajectory,

calculated over all station observations merged by time. The initial trajectory data provided by ASGARD in an "event.txt" file as shown in Figure 4-4. This file contains the time of each camera frame for each camera station, starting with time $t=0$ being the first frame for each station which contains the object, and the position along the path (L) where $L=0$ corresponds to $t=0$ on the first station to detect the object. Therefore, barring a chance simultaneous initial observation, only one station's observations contains a $t=0$, $L=0$ point. For this discussion, I refer to the path point time and length for the i'th frame of station s as t_{is} and L_{is}.

```
beg ; lat 43.45446 0.00295 lon −82.31767 0.00482 ht 109.640 0.200 x 1216.254 0.408 y −4557.465 0.174 z 4439.700 0.201
end ; lat 42.82546 0.00255 lon −82.89026 0.00418 ht 78.031 0.168 x 1176.957 0.355 y −4594.019 0.137 z 4366.345 0.178
rad ; alp 42.929 0.412 del 53.809 0.450 eta 70.027 0.368 rho 56.508 0.379
map ; 7 3 5 6
vel ; 59.42 60.06 58.20 60.47
avg ; 59.54 0.99
fit ; tag 0 no   1 t  0.0000 L  0.0000 R 151.6348 vel  0.0000 lat  43.4545 lon  −82.3177 ht 109.6401
fit ; tag 0 no   2 t  0.0330 L  1.6347 R 152.2747 vel 49.5378 lat  43.4432 lon  −82.3282 ht 109.0617
fit ; tag 0 no   3 t  0.0670 L  2.6422 R 152.6782 vel 29.6323 lat  43.4363 lon  −82.3347 ht 108.7054
fit ; tag 0 no   4 t  0.1000 L  6.3410 R 154.1956 vel 112.0850 lat  43.4109 lon  −82.3582 ht 107.3985
                                       :
                                       :
fit ; tag 1 no   1 t  0.0000 L 30.0652 R 233.5880 vel  0.0000 lat  43.2474 lon  −82.5078 ht  99.0602
fit ; tag 1 no   2 t  0.0330 L 31.9236 R 234.2177 vel 56.3155 lat  43.2346 lon  −82.5196 ht  98.4103
fit ; tag 1 no   3 t  0.0660 L 34.8544 R 235.2313 vel 88.8135 lat  43.2143 lon  −82.5382 ht  97.3862
fit ; tag 1 no   4 t  0.1000 L 36.7809 R 235.9190 vel 56.6595 lat  43.2010 lon  −82.5505 ht  96.7137
                                       :
                                       :
```

Figure 4-4. Event.txt file for event 20090906_012755 as provided by ASGARD. Event times 't' give frame times at 30 frames/sec, beginning at t=0 for the first frame of each station which contains the object. The path length 'L' is given in kilometres and provides the position of the object along the path with respect to the earliest observation. The 'tag' field contains the 0-based index into the map of station numbers in the 'map' line' (tag 0 = station 7, etc.)

```
#
#   version : 20090522
#    num_fr : 42
#      time : 20090906 01:27:56.587 UTC
#      unix : 1252200476.587262
#       ntp : LOCK −1530 38346 1691
#       seq : 137022
#       mul : 0 [A]
#      site : 06
#    latlon : 43.9850 −79.9742 386.0
#      text : Orangeville
#     label :
#     plate : 20090727-071001-06-aut-calib-ID
#      geom : 640 480
#    reject : 0
#
# fr    time   sum     seq       cx       cy
  30  −0.834  3169  136997  538.743  134.729  …
  31  −0.801  2910  136998  539.490  136.486  …
  32  −0.767  2943  136999  540.855  136.155  …
                     :
                     :
```

Figure 4-5. The station 6 event file ev_20090906_012756A_06.txt containing the base event time for that station, and the clock offset of the first observation.

The detailed event information for a given observation station s is found in the file named ev_<date>_<time>A_s.txt as shown in Figure 4-5. This file contains the date and time (d_{0s}) of the first observation of the object for that station. The file also contains time offsets for each point, the first of which (δ_{0s}) may be used as a clock offset for all path point times for that station. The assumed data and time corresponding to the eventual calculated position and velocity vector is the d_{0s} of the station whose path point list contains the $L=0$ point. This

station is referred to as the 'base' station, with the event date/time labelled d_{0b}. The adjusted time for the i'th path point for station s, assumed to be sufficient for merging of all path points, is calculated as:

$$t'_{is} = t_{is} + (d_{0s} - d_{0b}) + \delta_{0s} \qquad (16)$$

Visual inspection of the adjusted path points (t'_{is}, L_{is}) for the 20090906_012756 event did not reveal the hoped for near-linear arrangement. The plot in Figure 4-6 demonstrates that additional time offsets were at play. In discussions with Rob Weryk, and after his investigation of the station clocks, we concluded that 1) small sub-second synchronization issues were unavoidable with the ASGARD system, and 2) the time synchronization configuration for Station 7 was in error by 1 second for the time period Aug 1, 2009 00:00 through Sept 22, 2009 21:00.
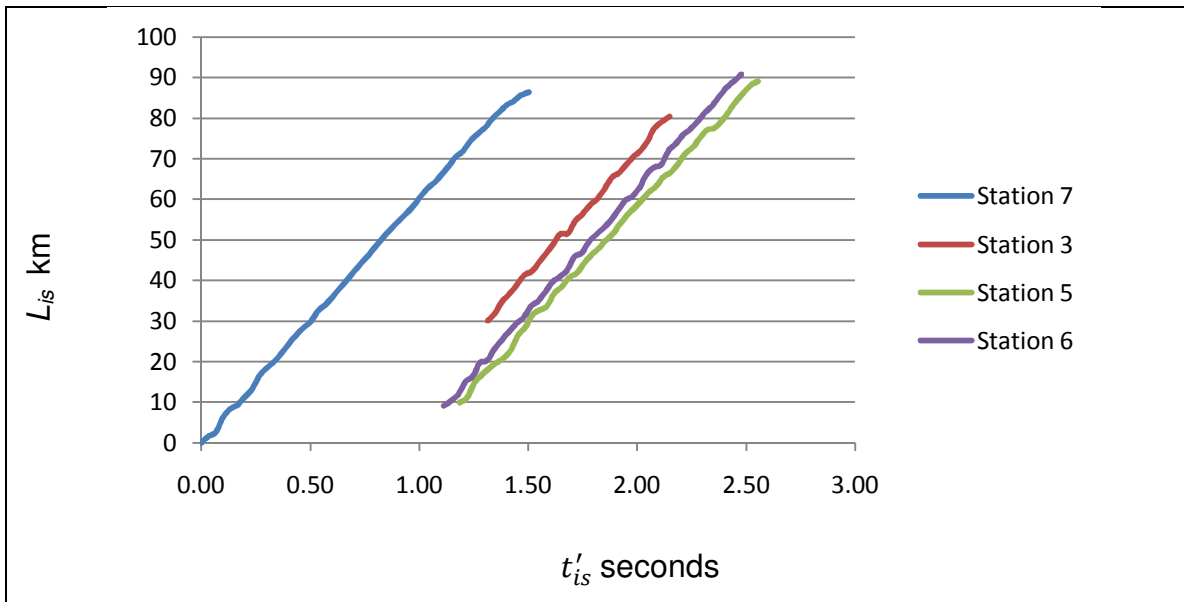
Figure 4-6. A plot of adjusted frame times and meteor path lengths for the event 20090906_012756

In order to provide an automated velocity calculation able to handle all such clock discrepancies, I assume similar slope to the velocity (L_{is}/t_{is}) plots, and calculate the time adjustment to super-impose the plots with a (0,0) intercept. This is done using a modified linear least squares fit (LLSF) algorithm, calculating the best fit

straight line which is not impacted by the deceleration curve at the tailing end of the trajectory. The new additional time adjustment for each station, a_s, is the t' intercept calculated using standard LLSF calculations as follows:

$$\Delta = N \sum t_{is}'^2 - \left(\sum t_{is}' \right)^2 \tag{17}$$

$$A = \left(\sum t_{is}'^2 \sum L_{is} - \sum t_{is}' \sum t_{is}' L_{is} \right)/\Delta \tag{18}$$

$$B = \left(N \sum t_{is}' L_{is} - \sum t_{is}' \sum L_{is} \right)/\Delta \tag{19}$$

$$a_s = A/B$$

or, simplified as the Δ divisor may be eliminated:

$$a_s = \frac{\sum t_{is}'^2 \sum L_{is} - \sum t_{is}' \sum t_{is}' L_{is}}{N \sum t_{is}' L_{is} - \sum t_{is}' \sum L_{is}}, \tag{20}$$

where all sums are over N points and N is selected as such that the coefficient of determination, r^2, is maximized over the first portion of the path, preventing the deceleration portion of the path from impacting the fit. Combining (16) and (20), we have a new adjusted time offset for each point of each station:

$$t_{is}'' = t_{is} + (d_{0s} - d_{0b}) + \delta_{0s} + a_s. \tag{21}$$

We may now calculate a velocity for the meteor in the non-decelerating portion of its trajectory (v_i) by calculating another modified LLSF as in (17), (18), and (19), where:

$$v_i = B \tag{22}$$

and A should approach 0. The calculated v_i above, and the initial meteor position and radiant vector from ASGARD, combine to provide a complete initial state of the meteor suitable for meteor orbit determination.

4.3 Calculating the Meteoroid Heliocentric Contact State

The ASGARD system uses two independent codes to calculate the geocentric position and velocity state of a meteoroid: MILIG and SMETS. These codes provide similar outputs describing the geocentric position of the object at the beginning of the observed meteor trajectory, and the geocentric position and apparent radiant direction at the end of the trajectory. Assuming the trajectory is relatively linear and not too long, assumptions which can be controlled by selecting a portion of the trajectory if need be, the apparent radiant is the same for the beginning and end points. The final required parameter is the velocity magnitude, as calculated above in 4.2, or as calculated by drag models and commonly reported as $\mathbf{v}_\infty$ in other meteor event systems. MILIG and SMETS provide geocentric positions in both rectangular and WGS84 coordinates with error, and radiant information in geocentric rectangular coordinates without errors, and in equatorial coordinates with errors. Since the reference frame used for rectangular coordinates is inconsistent among versions of MILIG and SMETS, and error bars were not available for rectangular velocity co-ordinates, this project concentrates on the use of WGS84 positions and equatorial radiants. These inputs are consistent with other published or available atmospheric trajectory data such as Spurný (1997) as described in section 7.4.4 European Events (1993-1996).

The heliocentric contact state of an object is calculated as a cloud of probability objects, each object having longitude λ_B, latitude φ_B, height h_B, radiant right ascension and declination α_R and δ_R, and velocity v_∞, all at an epoch t, where each of these values, including the epoch, are generated from a

Gaussian distribution defined by the reported mean and standard deviations. An independent heliocentric state and contact orbit elements are calculated for each probability object by the method below. The description is intentionally exhaustive, in that these calculations were arrived at with much debate, and their accuracy is important for determining an object trajectory and the resulting positions on survey images.

The geocentric rectangular coordinates for an object are calculated using WGS84 as follows where a is the semi-major axis in metres, b is the semi-minor axis in metres, and e is the eccentricity of the spheroid of the Earth.

$$a = 6378137.0$$
$$b = 6356752.314245$$
$$e^2 = \frac{a^2 - b^2}{a^2} \tag{23}$$

The geocentric coordinates centred on Greenwich are calculated using the transverse radius of curvature v as follows:

$$v = \frac{a}{\sqrt{1 - e^2 \sin^2 \varphi_B}}$$
$$x_G = (v + h_B) \cos \varphi_B \cos \lambda_B$$
$$y_G = (v + h_B) \cos \varphi_B \sin \lambda_B$$
$$z_G = ((1 - e^2)v + h_B) \cos \varphi_B \sin \lambda_B \tag{24}$$

The mean sidereal rotation of the Earth θ at time t is calculated as described in Chapter 11 of Meeus (1991). Assuming t is expressed in Julian days in UT:

$$T = \frac{t - 2451545.0}{36525}$$
$$\theta = 280.46061837 + 360.98564736629 \, (t - 2451545.0)$$

$$+0.000387933T^2 - T^3/38710000 \qquad (25)$$

The apparent sidereal rotation θ' is calculated as described in Chapters 11 and 21 of Meeus (1991) as:

$$\theta' = \theta + \Delta\Psi \, cos(\varepsilon_0 + \Delta\varepsilon) \qquad (26)$$

where ε_0 is the mean obliquity of the ecliptic, $\Delta\Psi$ is the nutation in longitude, and $\Delta\varepsilon$ is the nutation in obliquity. The calculations of nutation and obliquity require that the time of the event be expressed in dynamical time, not universal time. The dynamical time t_D is related to the universal time t by the formula:

$$t_D = t + \Delta t \qquad (27)$$

where Δt is calculated using a variety of means. For most dates of relevance to this project (subsequent to January 1, 1972), Δt is taken from a table of adjustments available on the US Naval Observatory web site (USNO, 2010). Appendix A – Dynamical Time and UT provides a complete explanation of the calculation of Δt over a range of dates.

The nutation in longitude $\Delta\Psi$ and the nutation in obliquity $\Delta\varepsilon$ are calculated from a table of periodic terms, the terms being a series of sine coefficients and arguments for $\Delta\Psi$ and a series of cosines for $\Delta\varepsilon$. The arguments for the sine and cosine terms are linear combinations of the mean elongation of the Moon from the Sun, the mean anomaly of the Sun, the mean anomaly of the Moon, the Moon's argument of latitude, and the longitude of the ascending node of the Moon's orbit on the ecliptic, all calculated for dynamics time t_D.

Appendix B – Nutation in Longitude and Obliquity describes this calculation in detail.

The mean obliquity is ε_0 calculated directly from the dynamical time t_D as follows:

$$U = \frac{t_D - 2451545}{3652500}$$

$$\varepsilon_0 = 84381.448" - 4680.93"U - 1.55"U^2 + 1999.25"U^3 \qquad (28)$$
$$- 51.38"U^4 - 249.67"U^5 - 39.05"U^6 + 7.12"U^7$$
$$+ 27.87"U^8 + 5.79"U^9 + 2.45"U^{10}$$

With the calculation of ε_0, $\Delta\Psi$, and $\Delta\varepsilon$, we are able to calculate apparent rotation of the Earth θ' using (26), and are able to rotate the geocentric coordinates x_G, y_G, z_G giving the Earth-centred equatorial coordinates with respect to the equinox of the date:

$$x_E = x_G \cos\theta' - y_G \sin\theta'$$
$$y_E = x_G \sin\theta' + y_G \cos\theta'$$
$$z_E = z_G \qquad (29)$$

These coordinates are converted to equinox J2000 by the method described in Chapter 20 of Meeus (1991). The conversion of equinoxes is performed using spherical coordinates, so we first convert the rectangular coordinates:

$$r_E = \sqrt{x_E^2 + y_E^2 + z_E^2}$$
$$\alpha_E = \tan^{-1}\frac{y_E}{x_E}$$
$$\delta_E = \sin^{-1}\frac{z_E}{r_E} \qquad (30)$$

The spherical equatorial coordinates are converted to equinox J2000 as follows:

$$T = \frac{t_D - 2451545.0}{36525} \quad , \quad T' = \frac{2451545.0 - t_D}{36525} \tag{31}$$

$$\zeta = (2306.2181'' + 1.39656''T - 0.000139''T^2)T'$$
$$+ (0.30188'' - 0.000344''T)T'^2 + 0.017998''T'^3$$

$$z = (2306.2181'' + 1.39656''T - 0.000139''T^2)T' \tag{32}$$
$$+ (1.09468'' + 0.000066''T)T'^2 + 0.018203''T'^3$$

$$\tau = (2004.3109\text{-}0.85330''T\text{-}0.000217''T^2)T'$$
$$- (0.42665'' + 0.000217T)T'^2 - 0.041833''T'^3$$

$$A = \cos \delta_E \sin(\alpha_E + \zeta)$$
$$B = \cos \tau \cos \delta_E \cos(\alpha_E + \zeta) - \sin \tau \sin \delta_E \tag{33}$$
$$C = \sin \tau \cos \delta_E \cos(\alpha_E + \zeta) + \cos \tau \sin \delta_E$$

$$\alpha_{EJ} = tan^{-1} \frac{A}{B} + z$$
$$\delta_{EJ} = sin^{-1} C \tag{34}$$
$$r_{EJ} = r_E$$

The J2000 equatorial coordinates of the position of the object are then converted back to rectangular coordinates:

$$x_{EJ} = r_{EJ} \cos \delta_{EJ} \cos \alpha_{EJ}$$
$$y_{EJ} = r_{EJ} \cos \delta_{EJ} \sin \alpha_{EJ} \tag{35}$$
$$z_{EJ} = r_{EJ} \sin \delta_{EJ}$$

The Earth-centred velocity of the object in equatorial J2000 coordinates has two components, the observed velocity calculated directly from the apparent velocity at infinity and its apparent right ascension and declinations, and the velocity at the point of the object due to the rotation of the Earth. The former is calculated simply as:

$$v_{xOJ} = -v_\infty \cos \delta_R \cos \alpha_R$$

$$v_{yOJ} = -v_\infty \cos \delta_R \sin \alpha_R \qquad (36)$$

$$v_{zOJ} = -v_\infty \sin \delta_R$$

The velocity due to the rotation of the Earth is the tangent vector at the Earth-centred position expressed in equatorial coordinates for the epoch of the date. The magnitude of the velocity is taken from a complete rotation of the earth at the object's distance and declination. Care must be taken when velocities are tracked in software with respect to solar time scales. We must make a sidereal adjustment.

$$v_{Rot} = 2\pi r_E \cos \delta_E \frac{86400}{86164.09053}$$

$$v_{xRot} = -v_{Rot} \sin \alpha_E$$

$$v_{yRot} = -v_{Rot} \cos \alpha_E \qquad (37)$$

$$v_{zRot} = 0$$

The rotation velocity vector $v_{xRot}, v_{yRot}, v_{zRot}$ must be converted from the equinox of the date to equinox J2000 using equations (30) through (35) substituting x_E, y_E, z_E with $v_{xRot}, v_{yRot}, v_{zRot}$ yielding $v_{xRotJ}, v_{yRotJ}, v_{zRotJ}$. We then sum this rotational velocity with the observed velocity from (36) yielding an Earth-centred J2000 equatorial velocity:

$$v_{xEJ} = v_{xOJ} + v_{xRotJ}$$

$$v_{yEJ} = v_{yOJ} + v_{yRotJ} \qquad (38)$$

$$v_{zEJ} = v_{zOJ} + v_{zRotJ}$$

Combining (35) and (38), we now have a complete position and velocity state for the object at time t in UT (t_D in dynamical time) in Earth-centred equatorial J2000 coordinates.

Converting this Earth-centred state to heliocentric coordinates involves acquiring an accurate position for the Earth. For the purposes of this project, the DE405 ephemeris is used, with the specific implementation returning the Earth's location and velocity in equatorial J2000 coordinates: $x_\oplus, y_\oplus, z_\oplus, v_{x\oplus}, v_{y\oplus}, v_{z\oplus}$. Care is taken to return the position of the Earth, and not the Earth-Moon barycentre. We then arrive at a heliocentric equatorial J2000 object state of:

$$x_{EH} = x_{EJ} + x_\oplus \qquad\qquad v_{xEH} = v_{xEJ} + v_{x\oplus}$$

$$y_{EH} = y_{EJ} + y_\oplus \qquad\qquad v_{yEH} = v_{yEJ} + v_{y\oplus}$$

$$z_{EH} = z_{EJ} + z_\oplus \qquad\qquad v_{yEH} = v_{yEJ} + v_{z\oplus} \qquad (39)$$

The above heliocentric equatorial coordinates need to be converted to ecliptical coordinates for the purposes of calculating time-of-contact Keplerian elements, and as we will see later, for gravitational integrations. Described here for the position x_{EH}, y_{EH}, z_{EH} the same methods apply for converting the velocity.

The coordinates are first converted to equatorial spherical coordinates:

$$r_{EH} = \sqrt{x_{EH}^2 + y_{EH}^2 + z_{EH}^2}$$

$$\alpha_{EH} = tan^{-1} \frac{y_{EH}}{x_{EH}}$$

$$\delta_{EH} = sin^{-1} \frac{z_{EH}}{r_{EH}} \qquad (40)$$

The conversion from equatorial spherical coordinates to ecliptical spherical coordinates proceeds as follows:

$$\lambda_H = tan^{-1} (\frac{sin\, \alpha_{EH}\, cos\, \varepsilon + tan\, \delta_{EH}\, sin\, \varepsilon)}{cos\, \alpha_{EH}})$$

$$\beta_H = sin^{-1} (sin\, \delta_{EH}\, cos\, \varepsilon - cos\, \delta_{EH}\, sin\, \varepsilon\, sin\, \alpha_{EH}) \qquad (41)$$

$$r_H = r_{EH}$$

where:

$$\varepsilon = \varepsilon_0 + \Delta\varepsilon \qquad (42)$$

is the true obliquity calculated from the mean obliquity ε_0 as calculated in (28) and the nutation in obliquity $\Delta\varepsilon$ as described above and in Appendix B. It is important to note that the epoch used for these obliquity calculations is the epoch J2000, not the epoch of the event. The ecliptical spherical coordinates are then converted to heliocentric rectangular coordinates:

$$x_H = r_H \cos \beta_H \cos \lambda_H$$
$$y_H = r_H \cos \beta_H \sin \lambda_H \quad\quad (43)$$
$$z_H = r_H \sin \beta_H$$

Similarly, we apply equations (40), (41) and (42) to the equatorial velocity vector to arrive at heliocentric velocity coordinates v_{xH}, v_{yH}, v_{zH}.

At this point we have the complete state of a probability object at a given time expressed in heliocentric ecliptical rectangular coordinates. As noted earlier in this section, equations (23) through (43) are applied independently to each probability object generated from random selections across all input error bars.

4.4 Rectangular to Keplerian Conversions

The heliocentric position and velocity state of an object given a specific point in time uniquely describes the orbit of the object, but not in a manner which allows one to understand the nature of the orbit. For this we need Keplerian orbital elements: semi-major axis (*a*), eccentricity (*e*), inclination (*i*), longitude of the ascending node (Ω), and the argument of perihelion (ω). The orbital element true anomaly (*f*) provides the position of the object in the orbit, but does not characterize the orbit. The conversion from a rectangular state such as the meteoroid contact state above to an instantaneous contact orbit proceeds as follows. The methods are derived from Bate et al. (1971) merged with an approach described in the private email Brown (2007).

The specific orbital energy ϵ is calculated as:

$$\epsilon = \frac{|\vec{V}|^2}{2} - \frac{\mu}{|\vec{R}|} \tag{44}$$

where R is the position vector (x_H, y_H, z_H) and V is the velocity vector (v_{xH}, v_{yH}, v_{zH}) from section 4.3, and $\mu = GM$ is the standard gravitation parameter appropriate for the solar mass and distance units being used. For this purpose we use $\mu = 4\pi^2 = 39.4784176043574$ corresponding to a distance unit of AU and a solar mass of 1. The semi-major axis is then calculates as:

$$a = {-\mu}/{2\epsilon} \tag{45}$$

To calculate the eccentricity e we first calculate the orbital angular momentum vector h, being the normal to the orbital plane, or the cross-product of the position and velocity vectors:

$$\vec{h} = \vec{R} \times \vec{V} \tag{46}$$

We then calculate the eccentricity as the magnitude of the eccentricity vector:

$$\vec{e} = \frac{\vec{V} \times \vec{h}}{\mu} - \frac{\vec{R}}{|\vec{R}|} \tag{47}$$

$$e = |\vec{e}| \tag{48}$$

The inclination is derived directly from the orbital momentum vector:

$$i = cos^{-1} \frac{h_z}{|\vec{h}|} \tag{49}$$

where h_z is the z-component of $\vec{h}$. The longitude of the ascending node is calculated as follows:

$$\vec{k} = (0,0,1)$$

$$\vec{n} = \vec{k} \times \vec{h} \tag{50}$$

$$\Omega = tan^{-1}\frac{n_y}{n_x} \ \ (|\vec{n}| \neq 0) \tag{51}$$

$$\Omega = 0 \ \ (|\vec{n}| = 0)$$

where $\vec{k}$ is the normal vector to the xy-reference plane, $\vec{n}$ is the vector from the Sun pointing to the ascending node, and n_x and n_y are the x and y-components of $\vec{n}$. The argument of perihelion is calculated from the dot-product of the ascending node and eccentricity vectors:

$$\omega = cos^{-1}\frac{\vec{n}\cdot\vec{e}}{|\vec{n}||\vec{e}|} \ \ (|\vec{n}| \neq 0, e_z \geq 0) \tag{52}$$

$$\omega = 2\pi - cos^{-1}\frac{\vec{n}\cdot\vec{e}}{|\vec{n}||\vec{e}|} \ \ (|\vec{n}| \neq 0, e_z < 0)$$

$$\omega = cos^{-1}\frac{e_x}{|\vec{e}|} \ \ (|\vec{n}| = 0)$$

and finally, the true anomaly is calculated as follows:

$$f = cos^{-1}\frac{\vec{e}\cdot\vec{R}}{|\vec{e}||\vec{R}|} \ \ (\vec{R}\cdot\vec{V} \geq 0) \tag{53}$$

$$f = 2\pi - cos^{-1}\frac{\vec{e}\cdot\vec{R}}{|\vec{e}||\vec{R}|} \ \ (\vec{R}\cdot\vec{V} < 0)$$

4.5 A Need for Meteoroid Path Integration

Early testing of the code to implement the above calculation of heliocentric state and contact orbital elements from ASGARD input files quickly demonstrated large discrepancies between calculated contact orbits and orbits at infinity calculated using MORB. This should not have been a surprise, as Ceplecha (1987) describes in detail the analytic methods used to compensate for the

Earth's gravitational influence on the object's heliocentric state. As well, the above calculations are fraught with potential errors in coordinate system assumptions. Therefore my calculations needed to be verified using an independent method. Dr. Paul Wiegert provided that check through the integration of geocentric inputs into his pre-existing gravitational integration code, with the intent of simply comparing his initial orbital elements at contact time to my calculated values. Agreement on initial heliocentric meteor state was achieved between the two codes, but the application of Wiegert's integration back over time demonstrated a substantial shift in orbital parameters (see Table 4-1), consistent with the disagreement between MORB calculated orbits, and those calculated at point-of-contact. This drift demonstrated the unsuitability of using a single orbit, be it an orbit at infinity calculated by MORB or an orbit at contact directly calculated from meteor position and velocity state.

t	a	E	incl	lasc	aper	meanan
0.000114	5.27374	0.921071	1.6556	174.628	102.238	-3.26614
0.000228	5.18168	0.919556	1.65462	174.628	102.227	-3.35408
0.000342	5.15071	0.919036	1.65392	174.628	102.225	-3.38224
0.000456	5.13515	0.918773	1.65349	174.628	102.224	-3.39479
			:			
0.005932	5.09155	0.918028	1.65206	174.628	102.223	-3.26889
0.006046	5.09148	0.918027	1.65206	174.628	102.223	-3.26538
0.006160	5.09141	0.918026	1.65206	174.628	102.223	-3.26188
0.006274	5.09134	0.918025	1.65206	174.628	102.223	-3.25837
0.006388	5.09128	0.918024	1.65206	174.628	102.223	-3.25486

Table 4-1. A sample meteor ephemeris as calculated by Wiegert. Time t is expressed in days prior to contact. The entire ephemeris spans approximately 10 minutes. Note the substantial drift in orbital elements.

Not wanting to "re-invent the wheel" in the field of numerical integrators, and understanding that this project did not require sophisticated optimizations or approaches in performance, we decided on a quick C to C++ conversion of an existing C-language implementation of RADAU-15, a 15th-order differential equation integrator documented in Everhart (1985). The RADAU family of integrators is characterized by the use of Gauss-Radau spacings for sequence time steps. The work of porting and integrating the publically available C-code

involved converting C code to C++, the language used in the remainder of the project coding, and abstracting the concepts of an integrator, force calculations, and physical objects into C++ interfaces and implementations to facilitate substitution of trial implementations.

The initial implementation of the RADAU integrator was tested by integrating the major objects of the solar system over 100 years, and comparing the results to the JPL DE405/DE406 ephemerides. A sample comparison is shown in Figure 4-7 and Figure 4-8, with a complete set of planetary and lunar comparisons provided in Appendix C. This test required the implementation of post-Newtonian adjustments, a refinement not required for the integration of meteoroid objects on Earth-approach. These post-Newtonian adjustments require knowledge of velocity state within the inter-object force calculations that is not required by meteoroid integrations. A concept of "forces-need-velocities" was introduced into the abstraction of force calculations to ensure no unnecessary passing of state information to force calculation implementations of differing sophistication.
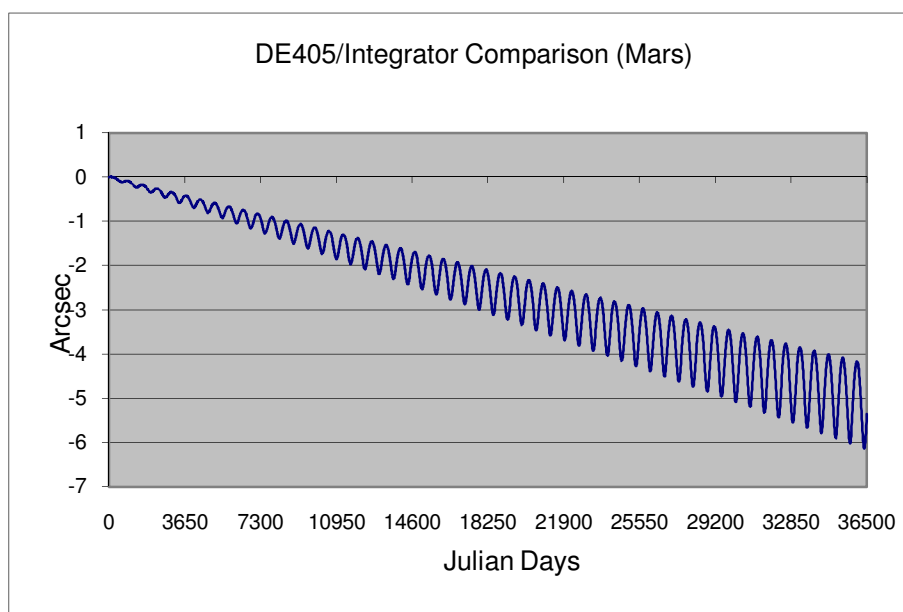
Figure 4-7. The difference in solar longitude in the position of Mars over 100 years as calculated by the RADAU-15 integrator with post-Newtonian adjustments, and the NASA JPL DE405/DE406 ephemeris service.
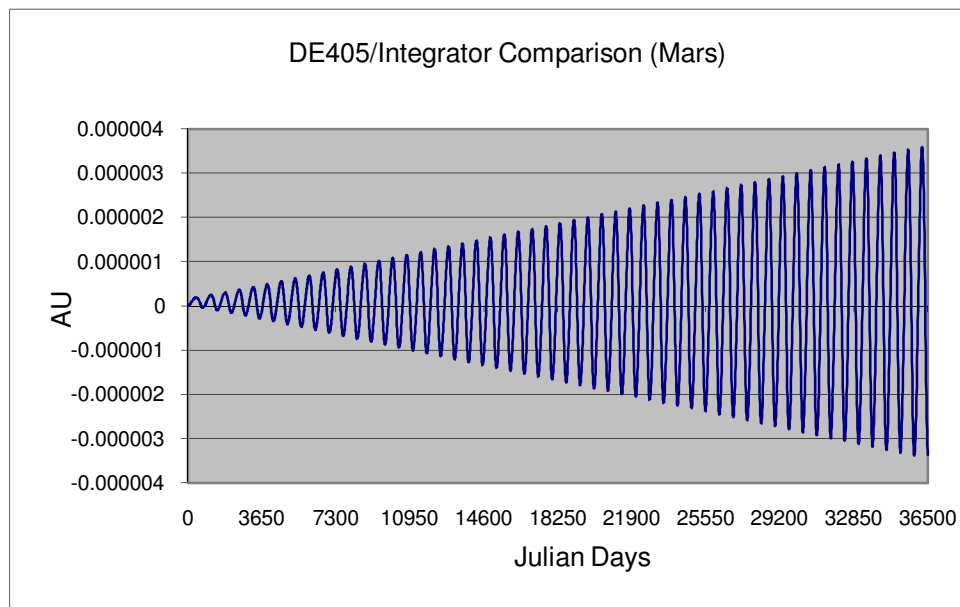
Figure 4-8. The difference in solar distance in the position of Mars over 100 years as calculated by the RADAU-15 integrator with post-Newtonian adjustments, and the NASA JPL DE405/DE406 ephemeris service. See Appendix C – RADAU-15 & DE405/DE406 Comparisons for a complete list of solar system body comparisons.

Several generations of force calculators and planetary object calculations were used or experimented with prior to arriving at what I term a mass-optimized approach. The initial implementation is described in the above DE405/DE406 test. All major solar-system objects are integrated along with a collection of zero-mass meteoroid probability particles. The zero-mass of probability particles both accurately reflects the situation that meteoroids have negligible gravitation impact on the larger bodies, and prevents interaction among the probability particles. The zero-mass approach works because the force calculations (using the RADAU terminology) are in fact acceleration calculators, calculating the acceleration of an object based on the mass and distance of another. Therefore we do not have a situation of acceleration being calculated from a zero gravitational force imparted on a zero-mass.

The first obvious optimization was the removal of the post-Newtonian adjustments and the removal of unnecessary velocity publication to the force calculators. Automated testing using character-by-character comparisons of

force calculation output journals demonstrated that this simplification generated consistent results with the original integrator. The second optimization attempt involved the removal of solar system objects from the integrated object list and the use of DE405/DE406 to position these objects at the appropriate times. Again using an automated character-by-character output journal comparison, this method provided consistent results. However, the performance of this method was far inferior to the pure integration method and was, therefore, not used in further work.

The final optimization implemented was a "mass-optimized" approach where zero-mass objects are dealt with in a totally separate logic and data tables from objects with mass. In situations where the number N of probability object (N=1000 for much of this project) far exceeds the number of system objects (11, Sun, 8 planets, Moon, Pluto), the force calculations approach an O(N) complexity rather that $O(N^2)$. This optimization is significant, even in cases where an $O(N^2)$ number of simple zero-mass checks are avoided. As in prior cases, the output of this approach was compared to prior approaches using character-by-character output journal comparisons.

The resulting integration back in time of a collection of probability points generated from contact state value and error bars yields a slowly expanding probability cloud representing the possible meteoroid paths. Figure 4-9 is a sample illustration of the Bunburra Rockhole event, generated from an initial contact sate provided by Pavel Spurný in a private correspondence (Spurný, 2009). The convergence of the probability cloud towards the eventual error bars in the original state is evident. There is a marked improvement over the probability clouds depicted in Figure 4-2 and Figure 4-3.
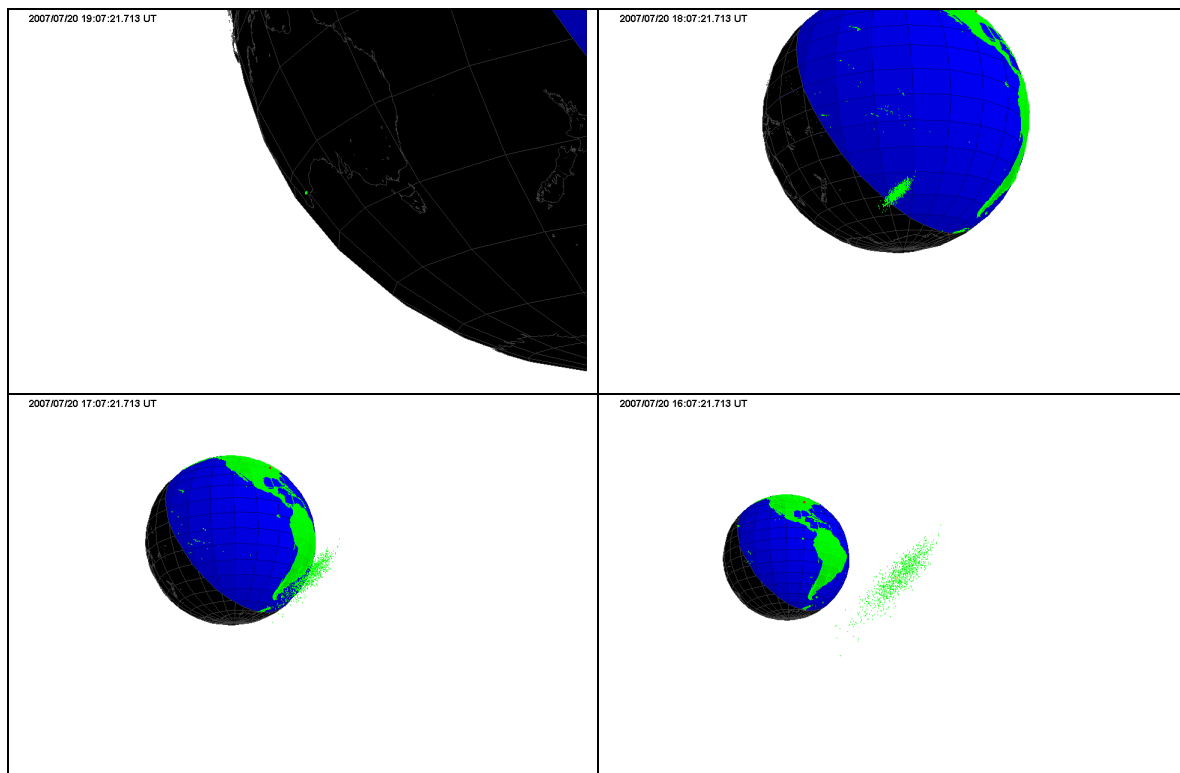
Figure 4-9. The RADAU-15 generated probability cloud for the Bunburra Rockhole effect. Meteoroid contact position, velocity and error bars were provide by Pavel Spurný in private correspondence (Spurný, 2009). The illustrations show the probability at the time of contact, and 1, 2 and 3 hours prior to contact. The viewer is a consistent 9100 km distance from the cloud's mean point.

4.6 Comparison to Ceplecha Orbits

The analytical orbit-at-infinity calculation methods of Ceplecha (1987) provide the means to verify the resulting orbits from the back-integration technique. Two sets of fireball orbits derived using Ceplecha's calculations were used to perform this comparison: the ten largest mass European Network events documented in Spurný (1997), and 10 more recent unpublished European Network events provided by Spurný in a private correspondence (Spurný, 2010). For the purposes of orbit-at-infinity calculations, the back-integrations are stopped at 2-months prior to Earth contact. Table 4-2 and Table 4-3 demonstrate the good correspondence between the methods. In these tables the term ClearSky refers to the program in which the integrations were implemented.

Event	Source	a	a SD	e	e SD	i	i SD	Node	node SD	peri	peri SD
EN070594(Leszno)	ClearSky	2.1070	0.0172	0.5328	0.0037	6.8953	0.0838	227.1320	0.0004	338.2490	0.2630
	Published	2.1000	0.0200	0.5320	0.0040	6.9100	0.0700	227.1100	0.0001	338.2000	0.2000
	Delta	0.0070	-0.0028	0.0008	-0.0003	-0.0147	0.0138	0.0220	0.0003	0.0490	0.0630
EN070893(Polnã)	ClearSky	2.0040	0.0283	0.5163	0.0070	18.8955	0.2539	135.4610	0.0004	209.5240	0.0727
	Published	2.0030	0.0060	0.5162	0.0013	18.9000	0.0300	135.4410	0.0002	209.5200	0.0700
	Delta	0.0010	0.0223	0.0001	0.0057	-0.0045	0.2239	0.0200	0.0002	0.0040	0.0027
EN150294(Dresden)	ClearSky	2.3386	0.0132	0.5784	0.0023	33.8443	0.0347	327.1350	0.0000	173.9130	0.1768
	Published	2.3380	0.0030	0.5783	0.0006	33.8410	0.0120	327.1300	0.0001	173.9000	0.0200
	Delta	0.0006	0.0102	0.0001	0.0017	0.0033	0.0227	0.0050	-0.0001	0.0130	0.1568
EN150396(Dobríš II)	ClearSky	7.5345	1.4256	0.8779	0.0204	8.3313	0.4868	355.5680	0.0007	141.1660	0.9380
	Published	7.2000	1.1000	0.8800	0.0200	8.3000	0.5000	355.5530	0.0001	141.2000	0.9000
	Delta	0.3344	0.3256	-0.0021	0.0004	0.0313	-0.0132	0.0150	0.0006	-0.0340	0.0380
EN220293(Meuse)	ClearSky	1.5069	0.0181	0.5682	0.0036	32.5929	0.1559	334.4100	0.0000	266.8560	0.8100
	Published	1.5000	0.0200	0.5670	0.0040	32.6000	0.2000	334.4070	0.0001	266.9000	0.8000
	Delta	0.0069	-0.0019	0.0012	-0.0004	-0.0071	-0.0441	0.0030	-0.0001	-0.0440	0.0100
EN220495A(Koutim)	ClearSky	2.3878	0.0105	0.7886	0.0008	4.1310	0.0462	32.4134	0.0002	277.3980	0.0788
	Published	2.3740	0.0040	0.7878	0.0003	4.1190	0.0120	32.3858	0.0001	277.5800	0.0500
	Delta	0.0138	0.0065	0.0008	0.0005	0.0120	0.0342	0.0276	0.0001	-0.1820	0.0288
EN231195(J. Hradec)	ClearSky	3.4436	0.1283	0.7813	0.0070	11.8921	0.5959	240.3480	0.0002	242.7970	1.9673
	Published	3.3900	0.0500	0.7790	0.0030	11.9900	0.0200	240.3360	0.0007	243.3000	0.3000
	Delta	0.0536	0.0783	0.0023	0.0040	-0.0979	0.5759	0.0120	-0.0005	-0.5030	1.6673
EN241095B(Odra)	ClearSky	1.3055	0.0859	0.5663	0.0193	52.7598	0.5480	211.0410	0.0006	281.4500	4.2692
	Published	1.3270	0.0110	0.5710	0.0020	52.8000	0.2000	211.0380	0.0007	280.2000	0.4000
	Delta	-0.0216	0.0749	-0.0047	0.0173	-0.0402	0.3480	0.0030	-0.0001	1.2500	3.8692
EN250594(Ulm)	ClearSky	2.0128	0.1134	0.5548	0.0214	2.5661	0.7510	244.4780	0.0293	312.0790	1.7704
	Published	2.0400	0.0200	0.5600	0.0030	2.5000	0.0400	244.5260	0.0007	313.1000	0.3000
	Delta	-0.0272	0.0934	-0.0052	0.0184	0.0661	0.7110	-0.0480	0.0286	-1.0210	1.4704
EN251095A(Tisza)	ClearSky	1.0780	0.0069	0.8068	0.0010	6.1339	0.1655	31.2538	0.0003	140.4080	0.3306
	Published	1.0770	0.0090	0.8067	0.0010	6.2000	0.2000	31.2595	0.0001	140.4000	0.4000
	Delta	0.0010	-0.0021	0.0001	0.0000	-0.0661	-0.0345	-0.0057	0.0002	0.0080	-0.0694

Table 4-2. A list of the 10 highest mass events from Spurný (1997) showing the published orbital elements calculated using Ceplecha (1987) calculations compared to the orbit at infinity elements calculated using the project's software ClearSky's integration technique. Semimajor axis, eccentricity, inclination, longitude of the ascending node and argument of perihelion are listed. Standard deviations are listed beside each element. ClearSky elements are displayed in blue if outside the published error bars. Published elements are displayed in red if outside the ClearSky calculated error bars. Note that the ascending nodes are numerically close, but are consistently flagged as being out of the corresponding error bars. The source data for these events is found in the results section Table 7-5 and Table 7-6.

Event	Source	a	a SD	E	e SD	i	i SD	node	node SD	peri	peri SD
EN040207	ClearSky	2.3329	0.0099	0.6990	0.0014	6.9378	0.0185	315.6630	0.0000	252.5130	0.0302
	Published	2.3400	0.0100	0.6997	0.0015	6.9200	0.0200	315.6470	0.0000	252.3300	0.0300
	Delta	-0.0071	-0.0001	-0.0007	-0.0001	0.0178	-0.0015	0.0160	0.0000	0.1830	0.0002
EN060402	ClearSky	2.4045	0.0158	0.6703	0.0023	11.4230	0.0289	16.8388	0.0001	241.1840	0.0342
	Published	2.4000	0.0200	0.6700	0.0020	11.4100	0.0300	16.8266	0.0000	241.2000	0.0600
	Delta	0.0045	-0.0042	0.0003	0.0003	0.0130	-0.0011	0.0122	0.0001	-0.0160	-0.0258
EN170702	ClearSky	0.9997	0.0011	0.5343	0.0003	14.1308	0.0367	115.2050	0.0000	303.7790	0.1081
	Published	1.0002	0.0011	0.5343	0.0004	14.1200	0.0400	115.1880	0.0000	303.7400	0.1100
	Delta	-0.0005	0.0000	0.0000	-0.0001	0.0108	-0.0033	0.0170	0.0000	0.0390	-0.0019
EN171101	ClearSky	1.3270	0.0044	0.4845	0.0011	7.4192	0.1257	235.4200	0.0003	266.7790	0.2524
	Published	1.3260	0.0040	0.4844	0.0011	7.4100	0.1300	235.3930	0.0000	266.8000	0.2000
	Delta	0.0010	0.0004	0.0001	0.0000	0.0092	-0.0043	0.0270	0.0003	-0.0210	0.0524
EN210199	ClearSky	1.7312	0.0105	0.4400	0.0034	17.5593	0.0625	301.2940	0.0002	197.9950	0.2155
	Published	1.7300	0.0110	0.4400	0.0030	17.5600	0.0600	301.2710	0.0007	198.0000	0.2000
	Delta	0.0012	-0.0005	0.0000	0.0004	-0.0007	0.0025	0.0230	-0.0005	-0.0050	0.0155
EN231006	ClearSky	2.3754	0.0103	0.8219	0.0007	0.5405	0.0279	210.4330	0.0050	285.8060	0.0915
	Published	2.3900	0.0100	0.8226	0.0007	0.5300	0.0300	210.2810	0.0030	285.7100	0.0900
	Delta	-0.0146	0.0003	-0.0007	0.0000	0.0105	-0.0021	0.1520	0.0020	0.0960	0.0015
EN280506	ClearSky	1.3927	0.0006	0.4694	0.0002	2.6022	0.0095	67.4835	0.0003	261.1740	0.0287
	Published	1.3936	0.0006	0.4691	0.0003	2.5500	0.0100	67.4132	0.0001	261.1000	0.0300
	Delta	-0.0009	0.0000	0.0003	-0.0001	0.0522	-0.0005	0.0703	0.0002	0.0740	-0.0013
EN290903	ClearSky	2.0138	0.0036	0.7024	0.0004	6.4963	0.0216	185.4720	0.0000	268.4880	0.0672
	Published	2.0190	0.0040	0.7027	0.0004	6.4800	0.0200	185.4540	0.0000	268.3900	0.0700
	Delta	-0.0052	-0.0004	-0.0003	0.0000	0.0163	0.0016	0.0180	0.0000	0.0980	-0.0028
EN300807	ClearSky	2.5232	0.0094	0.6284	0.0013	11.0871	0.0321	157.0890	0.0001	215.3720	0.1083
	Published	2.5290	0.0090	0.6290	0.0010	11.0600	0.0300	157.0600	0.0000	215.2500	0.1100
	Delta	-0.0058	0.0004	-0.0006	0.0003	0.0271	0.0021	0.0290	0.0001	0.1220	-0.0017
EN310800	ClearSky	0.7965	0.0002	0.2962	0.0003	16.8173	0.0148	158.8590	0.0001	19.0107	0.0261
	Published	0.7969	0.0002	0.2958	0.0003	16.7400	0.0200	158.8170	0.0000	19.1300	0.0300
	Delta	-0.0004	0.0000	0.0004	0.0000	0.0773	-0.0052	0.0420	0.0001	-0.1193	-0.0039

Table 4-3. A list of 10 fireball events from Spurný (2010) showing the published orbital elements calculated using Ceplecha (1987) calculations compared to the orbit at infinity elements calculated using the project's software ClearSky's integration technique. See Table 4-2 for further description. Note the consistent highlighting of ascending node variances. The source data for these events is found in the results section Table 7-9 and Table 7-10.

The close correspondence of orbit elements from the Ceplecha and integration techniques serves as both a validation for the time-honoured analytical method and as a confirmation the integration technique does accurately reproduce object approach trajectories. However, the small but systematic variance in longitude of ascending node required further attention. Section 11 of Ceplecha (1987) describes in detail the impact of Earth's gravity on calculating velocity and radiant direction of a meteor, this impact being removed prior to the calculation of orbital elements. However, in formula (48) of Section

11, Ceplecha makes the assumption that the longitude of the ascending node (Ω) of the orbit can be directly derived from the solar longitude of the Earth (L_{SUN}) at the time of impact. This is true of the instantaneous orbit of the meteoroid, but not its orbit at infinity. The instantaneous Ω is drawn towards the limiting value L_{SUN} as the meteoroid approaches the Earth. The magnitude of this shift in Ω depends on the approach characteristics and the length of time the meteoroid is influenced by Earth's gravity. The largest calculated variance in Ω is .15° for Spurný (2010) event EN231006 (see Table 4-3). Figure 4-10 demonstrates the shift in ascending node of approximately .1° of the Bunburra Rockhole event.
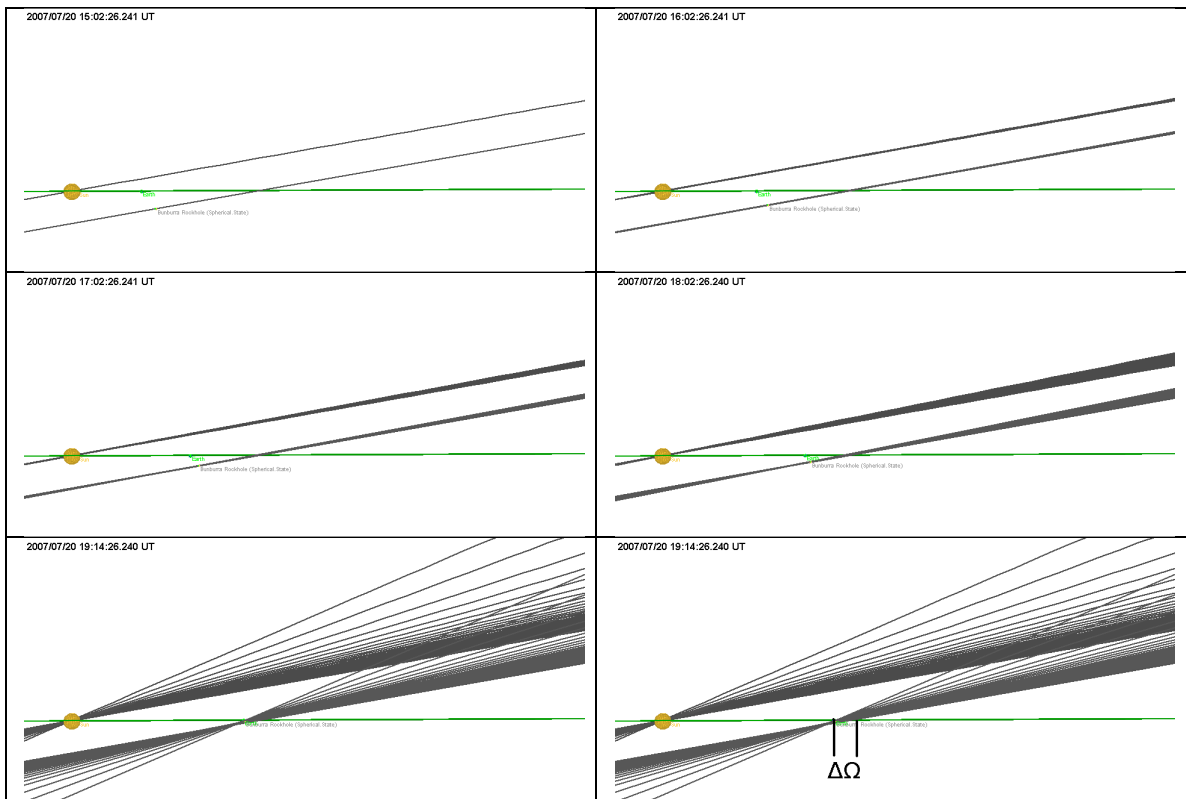
Figure 4-10. The shift ΔΩ of the ascending node Ω of the instantaneous orbit of the Bunburra Rockhole meteoroid. From left to right, top to bottom, the progress of the shift is shown, 4, 3, 2, and 1 hours prior to contact, at contact, and at contact with the shift highlighted. The rightmost diagonal lines represent the instantaneous orbits at the ascending node on the near side of the Sun. The leftmost lines represent the orbits at the descending node on the far side of the Sun.

A consequence of this variance in Ω that has not been quantified is the dependency in the Ceplecha calculations of all other orbit elements except

semimajor axis on Ω and L_{SUN}. Further quantification of the impact is noted as possible future work. A correlation study between $\Delta\Omega$ and the variances in other elements in Table 4-2 and Table 4-3 should be performed, along with an analysis of the impact of small $\Delta\Omega$ on the Ceplecha calculations.

5 SEARCHING SKY SURVEYS

Having developed the methods to accurately describe a meteoroid's position through the hours prior to Earth contact, we now turn to the problem of efficiently searching image surveys for images serendipitously containing the object. The search techniques described here work equally well for image catalogue searches of any object whose ephemeris is known.

5.1 Image frustums

Astronomical images are typically thought of as two-dimensional rectangular projections onto the celestial sphere. Such images may be defined by the right ascension (α) and declination (δ) of the four corners of the image, or by the α and δ of the image centre, width and height of the image, and the rotation around the image centre. The computations involved in determining the location of a fast moving object in relation to long image exposure involves several conversions of the object's position into observer centred α and δ as both the object and observer move over time. These conversions, although not complex, are computationally expensive as they involve trigonometric transformations. Since the position of an object is relative to the observer, there is little opportunity to optimize this heavy computation against multiple images, or against multiple image surveys. I, therefore, developed an image representation scheme that supports a front-end loaded one-time optimization of individual image representations, while reducing the object-image computation complexity.

A single survey image in reality is a projection of a three-dimensional volume of space. Assuming a rectangular image, this volume is a frustum as shown in Figure 5-1. A frustum is defined as the portion of a solid lying between two planes. An image frustum is the portion of a square pyramid lying between a front viewing plane and an arbitrary depth of field plane. Further in this chapter, I show that this frustum space can be transformed into a three dimensional rectangular 2x2x1 frustum space to which object position intersections are easily

calculated. The determination of the image frustum and the calculation of the transformation into a rectangular frustum space are costly, but may be performed once per image description with the resulting transformation being stored and associated with the image description.
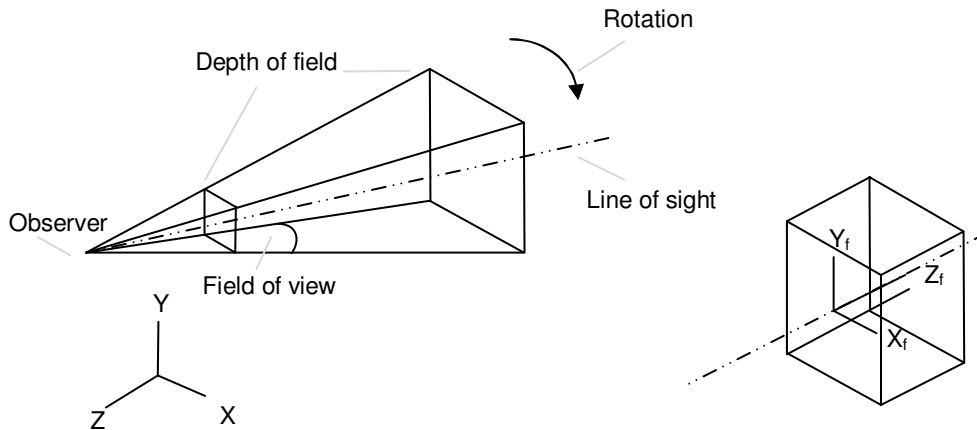
Figure 5-1. Viewing frustum in heliocentric space, and the cubic frustum space.

Viewing frustums and the related transformations have been used for decades in rendering three dimensional world scenes onto a two-dimensional view port (screen). The following discussion is based on the unpublished lecture notes and course exercises by Beatty (1980). An image frustum is defined by a set of parameters: observer position (d_x, d_y, d_z), a line of sight (s_x, s_y, s_z), horizontal and vertical fields of view (α_h, α_v), a near view distance (d, taken as a distance closer to the observer than the typical in-atmosphere meteor distance), and a depth of field (f, taken as infinity). The conversion of an arbitrary image description into these frustum description parameters is discussed in section 5.2 below. Here I describe how a PFM position (or the position of any solar system object) in heliocentric coordinates (x, y, z) may be translated to the image frustum space (x_f, y_f, z_f) by the simple application of a 4x4 transformation matrix T_f to the homogenous coordinates (x, y, z, 1), where T_f is the matrix product of a series of constituent transformations.

5.1.1 Translation

The position of the observer is accounted for by a translation transformation T_T which shifts the observer location to the coordinate system origin:

$$T_T : [x, y, z, 1] \begin{bmatrix} 1 & 0 & 0 & 0 \\ 0 & 1 & 0 & 0 \\ 0 & 0 & 1 & 0 \\ d_x & d_y & d_z & 1 \end{bmatrix} = [x_T, y_T, z_T, 1] \tag{54}$$

5.1.2 Line of Sight Rotations

Three rotation transformations T_{RX}, T_{RY}, and T_{RZ} are required to align the centre line of sight of the image onto the z-axis of the frustum space:

$$T_{RX} : [x, y, z, 1] \begin{bmatrix} 1 & 0 & 0 & 0 \\ 0 & \cos\theta_x & -\sin\theta_x & 0 \\ 0 & \sin\theta_x & \cos\theta_x & 0 \\ 0 & 0 & 0 & 1 \end{bmatrix} = [x_{RX}, y_{RX}, z_{RX}, 1] \tag{55}$$

where: $\theta_x = \tan^{-1}\frac{S_y}{S_z}$ is the rotation required around the x-axis to place the line of sight onto the x-z plane,

$$T_{RY} : [x, y, z, 1] \begin{bmatrix} \cos\theta_y & 0 & \sin\theta_y & 0 \\ 0 & 1 & 0 & 0 \\ -\sin\theta_y & 0 & \cos\theta_y & 0 \\ 0 & 0 & 0 & 1 \end{bmatrix} = [x_{RY}, y_{RY}, z_{RY}, 1] \tag{56}$$

where: $\theta_y = \tan^{-1}\frac{x_{RY}}{z_{RY}}$ is the rotation around the y-axis to place the line of sight onto the -z axis, and x_{RY} and z_{RY} result from $(sx, sy, sz, 1) \times T_{RX}$, and

$$T_{RZ} : [x, y, z, 1] \begin{bmatrix} \cos\theta_z & \sin\theta_z & 0 & 0 \\ -\sin\theta_z & \cos\theta_z & 0 & 0 \\ 0 & 0 & 1 & 0 \\ 0 & 0 & 0 & 1 \end{bmatrix} = [x_{RZ}, y_{RZ}, z_{RZ}, 1] \tag{57}$$

where: $\theta_z = \tan^{-1} \frac{x_{RY}}{y_{RY}}$ is the rotation around the z-axis to place the up vector onto the y-z plane, and x_{RZ} and y result from $[s_x, s_y, s_z, 1][T_{RX}][T_{RY}]$.

5.1.3 Windowing Transformation

A windowing transformation T_W centres the frustum on (0,0) and performs the scaling required to reduce the coordinates to a 2x2 square. It is the product of two simple transformations, a translation in X and Y and a scaling in X and Y, applied to a rotated observer position.

.

$$T_W : [x,y,z,1] \begin{bmatrix} 1 & 0 & 0 & 0 \\ 0 & 1 & 0 & 0 \\ 0 & 0 & 1 & 0 \\ -e_x & -e_y & 0 & 1 \end{bmatrix} \begin{bmatrix} 1/w_x & 0 & 0 & 0 \\ 0 & 1/w_y & 0 & 0 \\ 0 & 0 & 1 & 0 \\ 0 & 0 & 0 & 1 \end{bmatrix} = [x_W, y_W, z_W, 1]$$

(58)

where: e_x and e_y are the observer position resulting from $[d_x, d_y, d_z, 1]$ $[T_{RX}][T_{RY}][T_{RZ}]$, and w_x and w_y are the image window size calculated from the assumed distance to the image near plane, and the fields of view:

$$w_x = \tan \frac{\alpha_x}{2}, \quad w_y = \tan \frac{\alpha_y}{2}$$

5.1.4 Perspective Transformation

The perspective transformation is a product of three transformations:

1) a scaling transformation to reverse the sign of the z-coordinate, turning the right-handed heliocentric coordinate system into the left handed frustum coordinate system.

2) a transformation yielding appropriate z-dependent scaling of x, y and z to facilitate clipping to the 2x2x1 frustum space.

3) a translation based on the observer location and the observer distance to the front face of the frustum, which adjusts the front face to be at the origin.

Assuming the viewing frustum is rotated to be centred down the increasing z-axis, with the near face on (0, 0, 0) and the observer at (0, 0, -d), any point (x, y, z) is projected onto a point $(x, \; y, z = 0\;)$ on the near face. By similar triangles:

$$\frac{x'}{d} = \frac{x}{d+z} \qquad \frac{y'}{d} = \frac{y}{d+z}$$

and therefore:

$$x' = \frac{x}{w_f} \qquad y' = \frac{y}{w_f} \; where \; w_f = 1 + \frac{z}{d} \tag{59}$$

The divisor $w_f = 1 + \frac{z}{d}$ is called the normalized z-depth of the point, allowing the x and y coordinates to be clipped to the range of values -1 to 1. Of no importance to astronomical image intersection is the clipping of object positions to the front and back frustum planes. For consistency with the transformations used in scene rendering, the z coordinate adjustment of $(\frac{1}{f} + \frac{1}{d})$ is used, supporting z coordinate clipping to the range 0 to 1 corresponding to the near and far plane distances of d and f. The transformation which yields the appropriate normalized z-depth and z-depth clipping is:

$$\begin{bmatrix} 1 & 0 & 0 & 0 \\ 0 & 1 & 0 & 0 \\ 0 & 0 & \frac{1}{f} + \frac{1}{d} & \frac{1}{d} \\ 0 & 0 & 0 & 1 \end{bmatrix}$$

and the complete perspective transformation when combined with the above mentioned translation and scaling transformations is:

$$T_P : [x,y,z,1] \begin{bmatrix} 1 & 0 & 0 & 0 \\ 0 & 1 & 0 & 0 \\ 0 & 0 & -1 & 0 \\ 0 & 0 & 0 & 1 \end{bmatrix} \begin{bmatrix} 1 & 0 & 0 & 0 \\ 0 & 1 & 0 & 0 \\ 0 & 0 & \frac{1}{f} + \frac{1}{d} & \frac{1}{d} \\ 0 & 0 & 0 & 1 \end{bmatrix} \tag{60}$$

$$\begin{bmatrix} 1 & 0 & 0 & 0 \\ 0 & 1 & 0 & 0 \\ 0 & 0 & 1 & 0 \\ 0 & 0 & -(e_z - n) & 1 \end{bmatrix} = [x_P, y_P, z_P, w_P]$$

5.1.5 The Frustum Transformation and Edge Coordinates

By combining the above translation, rotation, windowing, and perspective transformations, we arrive at a single 4x4 transformation:

$$T_F = [T_T][T_{RX}][T_{RY}][T_{RZ}][T_W][T_P] \tag{61}$$

where an object's heliocentric position can be transformed as follows:

$$[x, y, z, 1][T_F] = [x_f, y_f, z_f, w_f] \tag{62}$$

An object's position with respect to the 2x2 image frustum front face is:

$$x_I = \frac{x_f}{w_f} \ , \ \ y_I = \frac{y_f}{w_f} , \tag{63}$$

where $-1 \le x_I \le 1$ and $-1 \le y_I \le 1$ correspond to the object being on the image. Additional outputs of the above transformation are four values called edge coordinates, which allow for quick object-image checking, prior to performing the above divisions in calculating x_I and y_I:

$e_1 : w_f + x_f$ left edge

$e_2 : w_f - x_f$ right edge

$e_3 : w_f + y_f$ bottom edge

$e_4 : w_f - y_f$ top edge

In all cases, the edge coordinate e_i exhibits the properties:

$e_i > 0$ the position is inside the edge

$e_i < 0$ the position is outside the edge

As long as the 4x4 T_f transformation matrix is calculated before search time, the computation required to determine an object-image intersection at a single point in time is the 12 multiplications and 9 additions required to calculate the $x_f,$ $y_f,$ and w_f values, and the 4 additions and 4 comparisons required to perform the edge coordinate checks.

5.1.6 The Image Intersection Algorithm

Images are not instantaneous; there is always an exposure time period. During this elapsed time both the object being checked and the observer move in heliocentric space. This is particularly of concern when dealing with close-by and, therefore, potentially fast-moving objects such as PFMs. Beatty (1980) deals with the issue of a line segment intersecting the viewing frustum when the endpoints are not within the frustum. I extend on his approach to deal with a point object's motion, the difference being that I work with two viewing frustums, one calculated for the beginning of the exposure, one for the end, thereby accounting for observer motion. Figure 5-2 shows some examples of possible object motion, and the edge coordinate properties at the beginning and end of image exposure.
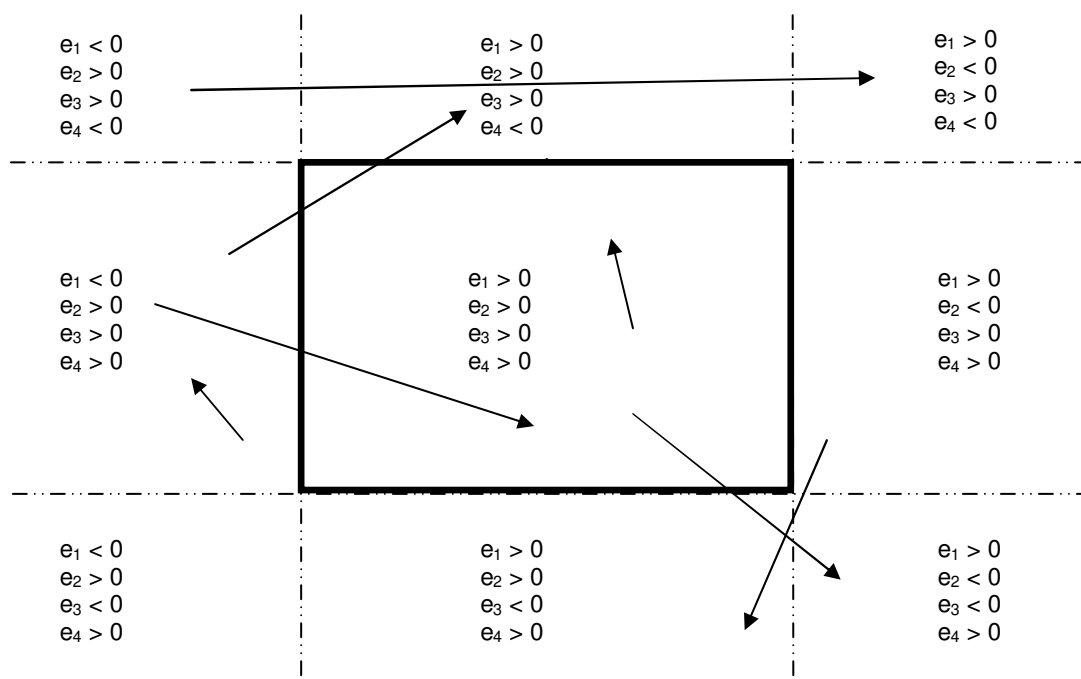
Figure 5-2. Sample object motions in relation to an image exposure.

As can be seen in Figure 5-2, the transitions from image beginning and end edge coordinates characterize object motions as: clearly in the image for some or all of the exposure, clearly outside the image for the entire exposure, or possibly in the image for a portion of the exposure. The entire image-object intersection algorithm can be stated as follows:

At image download time, performed once per image, calculate and store:
1) the image frustum description D_s at the start of the exposure.
2) the image frustum transformation T_s at the start of the exposure.
3) the image frustum description D_e at the end of the exposure.
4) the image frustum transformation T_e at the end of the exposure.

At image search time:
1) Calculate the object's position at the start of the exposure
2) Apply transformation T_s to this position, deriving edge coordinates e_{s1}, e_{s2}, e_{s3}, and e_{s4}.
3) If all four edge coordinates are positive, stop. An intersection exists.
4) Calculate the object's position at the end of the exposure.
5) Apply transformation T_e to this position, deriving edge coordinates e_{e1}, e_{e2}, e_{e3}, and e_{e4}.
6) Analyse e_{s1}, e_{s2}, e_{s3}, e_{s4} transitions to e_{e1}, e_{e2}, e_{e3}, e_{e4} and characterize the object path as being:
   a. Definitely in the image, stop.
   b. Definitely not in the image, stop.
   c. Possibly being in the image.
7) Perform linear intercept calculations on the segment $(e_{s1}, e_{s2}, e_{s3}, e_{s4})$, $(e_{e1}, e_{e2}, e_{e3}, e_{e4})$ determining the 0 intercepts (and the associated times) corresponding to the object's path across the image boundaries. If any of these intercepts occur within all four boundaries, the object path intercepts the image for a period of time.

If an image-object intersection is detected, the path of the object in the image may be simulated by iterating through the time range in which the object appears in the image. The stored frustum descriptions D_s and D_e provide end descriptions for the frustum, from which interim descriptions may be interpolated, and interim frustum transformations may be calculated. Recognizing this is a

computationally heavy process, it is only performed once a positive image intersection has been identified.

5.2 Automated downloads and pre-processing

The object-image intersection process described in section 5.1.6 assumes the opportunity to have pre-calculated image frustum descriptions and transformations prior to executing object searches. I have developed a generic image catalogue data base which serves to:

1) Maintain local copies of available image databases.

2) Provide a generic representation of the images databases.

3) Support the storage of the above pre-calculated data.

4) Provide indexing to support various object search use cases.

5.2.1 Image Catalogue Description

The image catalogue developed for this project is implemented as a flat file of generic image data referring back to local copies of download image databases.   Indexes are maintained on the image catalogue to facilitate searching by survey name, time frame, or both.   The image catalogue is recreated from scratch on every download cycle. This approach was taken to avoid the concerns of needing a sophisticated underlying database technology that could handle both efficient insertion and querying.   A description of the catalogue follows. The download process is described in section 5.2.2.

Local Image Collections

Each supported image survey is referred to as a "Collection".   This nomenclature allows for the searching of image collections other than formal sky surveys (e.g., space mission catalogues, amateur astrophotography).   Image collections are stored locally in the format of the source survey or collection. A description of each collection must be manually created to permit the software to parse the image collection, both for generic data required for image searches, and for the collection-specific data needed to describe the image when an image-

object intersection is found. An example collection description for the CFHTLS survey is shown in Figure 5-3.

```
ClearSky
Image Collection Definition
1.0
[Collection]
CollectionName=CFHT Catalogue
DownloadURL=http://www.cadc.hia.nrc.gc.
ca/cadcbin/cfht/megaprime_proxy
DownloadFile=ImageCollectionCFHT.txt
FieldWidth=1.0
FieldHeight=1.0
Location=CFHT
[Format]
Title=CFHT Catalogue
Format=TabDelimited
Comment=#
Field1=@name
Field2=@ra
Field3=@dec
Field4=object
Field5=URL
Field6=category
Field7=filter
Field8=obstype
Field9=crunid
Field10=runid
Field11=@exp
Field12=@time
Field13=public_date
Field14=qso_status
Field15=is_phot
Field16=obs_iq_refccd
Field17=procdate
Field18=elixirswv
Field19=flipssvw
```

```
[Field-@name]
Title=Exposure
Source=1
Field=1
Format=int

[Field-@ra]
Title=RA
Source=1
Field=2
Format=float
Units=mas

[Field-@dec]
Title=Dec
Source=1
Units=mas
Field=3
Format=float

[Field-object]
Title=Target Object
Source=1
Field=4
Format=char(15)

[Field-URL]
Title=Imae URL
Source=1
Field=5
Format=varchar(73
```

```
Field-category]
Title=Category
Source=1
Field=6
Format=char(10)
[Field-filter]
Title=Filter
Source=1
Field=7
Format=char(10)
[Field-obstype]
Title=Observation
Type
Source=1
Field=8
Format=char(10)
[Field-crunid]
Title=C Run ID
Source=1
Field=9
Format=char(10)
[Field-runid]
Title=Run ID
Source=1
Field=10
Format=char(10)
[Field-@exp]
Title=Exposure Time
Source=1
Field=11
Format=real
[Field-@time]
Title=Image Time
Source=1
Field=12
Format=datetime
```

Figure 5-3. A sample image collection description (CFHTLS). Description data in bold signifies generic data which is expected in any collection description.

The local copy of an image collection may reside in a single file (as with the CFHTLS). In cases where the image collection file structure is complex, as in the case of the Minor Planet Centre (MPC) Sky Coverage collection, customized external programs, or internal code components may be developed to manage that complexity.

Image Collection Records

Image collection records are maintained in a single flat file that is recreated on every automated or manual request to update the image catalogue from the various image collection sources. These records include references back to the local copies collection databases, sufficient information to generically define an image independently of its source (date time, direction, size, orientation) and the image description and transformation information discussed in section 5.1. Figure 5-4 details the content of each image collection record.

Image Collection	The name of the image survey, database, or collection. E.g. "CFHT Catalogue", "Catalina Catalogue".
Image File	The local copy of each image survey is described by one or more file names, and a description of the format of these files. The image catalogue points to the file number and file offset corresponding to an image in this set of files.
Image Offset	The position in the image file where the source description of the image may be found (see Image File).
Right Ascension	The right ascension of the centre of the image.
Declination	The declination of the centre of the image.
Width	The width of the image in radians.
Height	The height of the image in radians.
Start Time	The start date and time of the image exposure.
Exposure	The length of the exposure in seconds.
Starting Frustum	The parameters used to describe the image frustum at the beginning of the exposure, and the contents of the 4x4 transformation matrix used to convert object positions to the frustum space. The frustum description includes: • Frustum rotations around each axis • Dimensions of the frustum front face • Observer distances to the front and back faces • 16 floating point numbers corresponding to the T_f image frustum transformation described in section 5.1.5.
Ending Frustum	The parameters used to describe the image frustum at the end of the exposure (See Starting Exposure)

Figure 5-4. Image catalogue record description.

Image Collection Indexes

Two indexes are maintained on the image catalogue. The collection/time index provides the list of images sorted by image date and time within a collection. This index supports the searching of a single image collection over an

optional time range. The time/collection index provides the list of catalogue images sorted by time across all collections. This index supports the cross survey search of images for a given time frame. Image collection indexes are recreated from scratch on every rebuilding of the image collection during automated and manual catalogue updates.

5.2.2 Image Survey Download Process

The project's images catalogue file and indexes are periodically recreated from local copies of the various image collections. Each collection is defined within the software by a collection description, with each description containing directives for the updating or wholesale replacement of the local collection files. Directives of the form **DownloadURL=<URL>** and **DownloadFile=<local path>** drive a basic wholesale replacement of a local image collection with an update from the Internet. A directive of the form **DownloadExecCmd=<program>** causes an external program to be executed to perform the updating of the local image collection. Finally, the **DownloadImplementation=<key>** directive indicates that an internal code implementation registering with the specified key is to be executed to update the local collection.

The survey download process proceeds as follows:
1) The program steps through each defined image collection, utilizing each download directives in the collection descriptions to drive the replacement or updating of the local copy of each image collection.
2) The image catalogue data file and index files are deleted.
3) The local files of each image collection are scanned sequentially, the manner in which they are parsed being dictated by directives in the image collection description. Of most importance in these descriptions are the location and format of generic image data needed for any image. For each image, a generic image description with frustum descriptions and transformations is

output to the catalogue. In-memory indexes by collection/date-time and date-time/collection are maintained.

4) When all collections are processed, the in-memory indexes are sorted and written to disk.

Table 5-1 lists the number of image records downloaded for each survey at the time of the writing of this thesis.

Image Collection	Data Source	# Images	Image Collection	Data Source	# Images
CFHT	CFHT	92250	G96 (Mt. Lemmon)	MPC	44930
SPACEWATCH	MPC	8938	924 (Trois-Rivieres)	MPC	1
691 (SPACEWATCH)	MPC	19971	699 (Lowell - LONEOS)	MPC	0
683 (Goodricke-Pigott)	MPC	5	644 (Palomar – NEAT)	MPC	5597
333 (Desert Eagle)	MPC	98	NEAT	MPC	112445
CATALINA	MPC	1810	LINEAR	MPC	876635
CSS (Catalina)	MPC	64816	428 (Reedy Creek)	MPC	0
E12 (Siding Spring)	MPC	70322			

Table 5-1. Image collection record counts and collection sources. MPC leaves download data validity to the submitter, therefore several table rows may in fact represent the same survey. In many cases the three-character MPC observatory code is used to name the image collection.

5.2.3 CFHT Image Database Download

The entire CFHT image database is available by a single HTTP query, returning the entire image database. The approximately 60 megabyte file (at the time of writing) is downloaded, stored as-is, and used as downloaded to produce generic image records in the project's image catalogue.   The data records contain unique image identifications, date and time, exposure, and pointing direction in right ascension and declination. Per image fields of view are not provided, so the field of view is specified as directives in the CFHT collection description file.   The image orientation is not provided, so all images are assumed to be oriented with the up direction pointing to the celestial north.

5.2.4 MPC Sky Coverage Pointing Data Download

The MPC Sky Coverage Pointing Data is a service provided by MPC permitting surveys to submit image lists for the purposes of cataloguing sky coverage. The data is a collection of data files, each containing a list of images captured by one survey over a given day. The name of each data file contains a survey identification code and the date of the images.   The records of the files simply contain the right ascension and declination of each of the four corners of an image, and the limiting magnitude of the image. The corner locations are used to determine image direction, fields of view, and the image orientation. Noticeably lacking are the time of each image, and a unique identification for each image. Therefore, all images are deemed to be 24-hour exposures, and the resulting intersections of object and image can only be used as a trigger of possible success. Images are also given a sequential identification number assigned as new MPC image records are processed. The chance of true success is quite small with close and apparently fast moving PFM's. The 24 hour exposure time also tends to confuse the on-image determination with the complexity of relative motions of observer and object during that time period. The ideal solution is to acquire direct access to the survey databases feeding MPC.

The download process is performed by a customized section of code, registering into the code's catalogue manager module as a handler of the "MPC" implementation.   Several individual image collection descriptions, each representing a sky survey that submits images to the MPC site, contains a **DownloadImplementation=MPC** directive.   For each such collection, the program:

1) Creates an interim collection file to hold all MPC data records for the survey collection, if the file does not already exist.
2) FTP is used to scan the remote MPC folder structure, downloading any files for a collection that are not already residing on the local system for that collection.

3) The local folder structure is then scanned for any file for the collection whose operating system file timestamp is newer than the timestamp of the interim collection. Any new local files are added to the interim collection file, with MPC records being augmented with the above mentioned assumed exposure time and unique image identification. The interim collection file is now ready for use as the source for creating the final image catalogue.

6 SOFTWARE OVERVIEW

6.1 Introduction to ClearSky

ClearSky is an astronomical simulation program developed as hobbyware by the author. Prior to its use in this project, ClearSky was primarily used as a visualization tool for public education in astronomy.   In recent years ClearSky outputs have been used by members of the UWO Astronomy department for visualizations of solar system object orbits and meteor streams. The intent of the software is to aid in the understanding of astronomical concepts, motions, and scales. It is not intended to compete in output quality with commercially available sky plotting software such as Earth Centred Universe or photo-realistic simulators such as Starry Night.   Features of the software prior to project inception included:

- Arbitrary 3D visualization based on arbitrary observer position, line of sight, field of view, and view orientation.
- Interactive scene content and perspective editing, with scene definition storage in editable textual files.
- Support of static, in motion and rotating reference frames.
- Production and replaying of animations over arbitrary time intervals and scene perspective changes.
- Automated periodic refreshes of various object databases, including MPC minor planet database, MPC comet database, MPC event calendar, William Harris's globular cluster database.
- Display of equatorial, ecliptical and galactic coordinate grids.
- Tracking of object paths against multiple reference frames.
- Display of mean and instantaneous orbits, with tracking of instantaneous orbital changes.
- Stellar background from Yale Bright Star Catalogue.
- Planetary and lunar positioning from various sources including VSOP87.

- Creation, storage, and management of natural and spacecraft object ephemerides.
- Automated JPL Horizons interface for the downloading of object ephemerides, with path resolution verifications for local high-resolution downloads (as required by spacecraft or small object fly-bys).
- Eclipse visualizations.

Figure 6-1 contains sample visualizations from the software. Functionality added to the software in support of this project includes:

- Object positional probability clouds and ephemerides.
- Gravitational integration of objects from an initial state.
- Meteoroid definitions and meteoroid event imports.
- Sky survey image cataloguing and searching.
- Sky survey effectiveness reporting.
- Enhanced image scene rendering to support sky survey image simulation:
    - US Naval Observatory star database support.
    - Survey CCD grid simulation.

Interaction with the software is done primarily through a graphical user interface (GUI), with maintenance performed through custom import plug-ins or manual editing of textual files. A limited command-line interface supports batch operations such as an automated database refresh operation. I envision using this command line interface to allow for the automated invoking of sky surveys as more meteor data and sky survey catalogues become available. At this point in time, large batch operations such as survey searches and survey effectiveness analyses are invoked from the GUI. Figure 6-2 shows a sample screen shot of the ClearSky GUI.
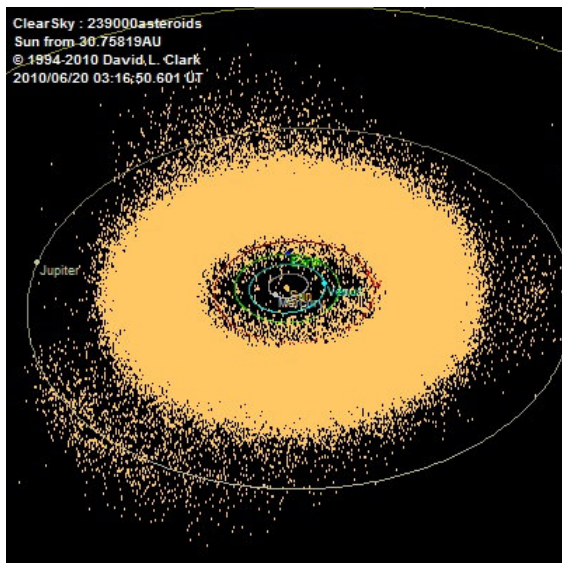
A solar system display showing the Sun, planetary orbit and positions, and the locations of 239,000 MPC objects.
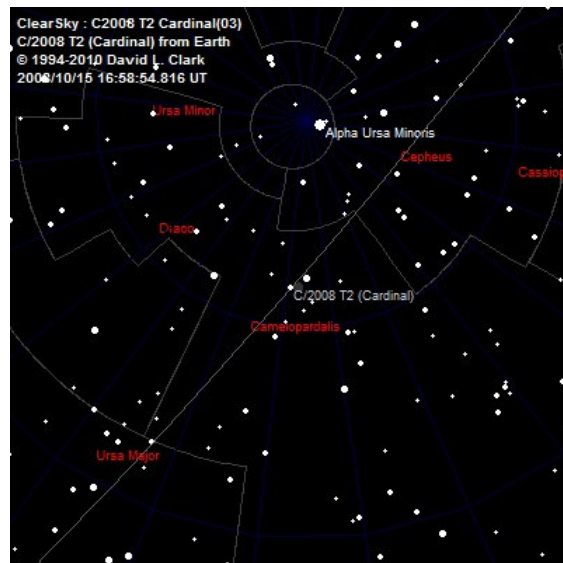
A sky chart showing the position of a comet. An animation over time shows the apparent of the object through the sky.
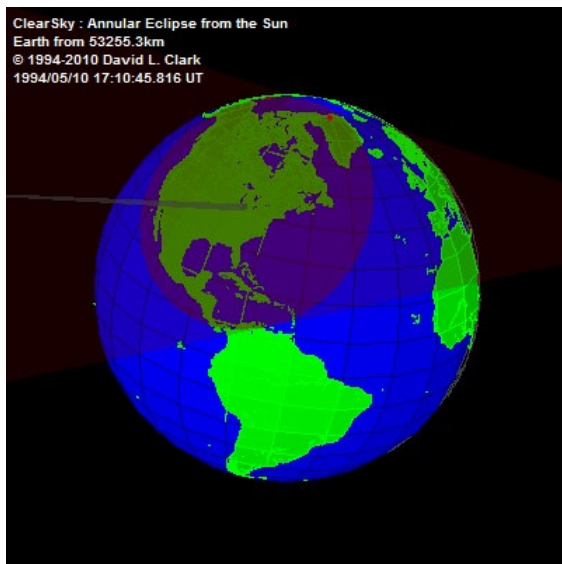
The umbral and penumbral shadows of the Moon during the 1994 annular eclipse over North America.

Figure 6-1. Sample outputs from ClearSky.
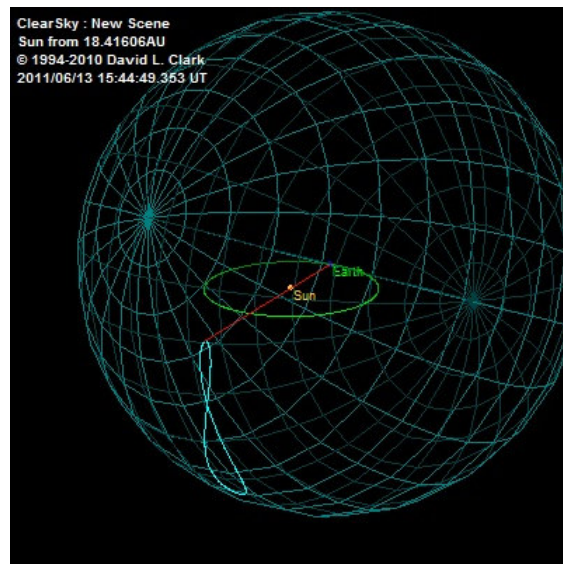
A projection of the Sun's position on the alt/az celestial sphere, with path tracking at discrete 1 day intervals for one year. The result is the solar analemma.
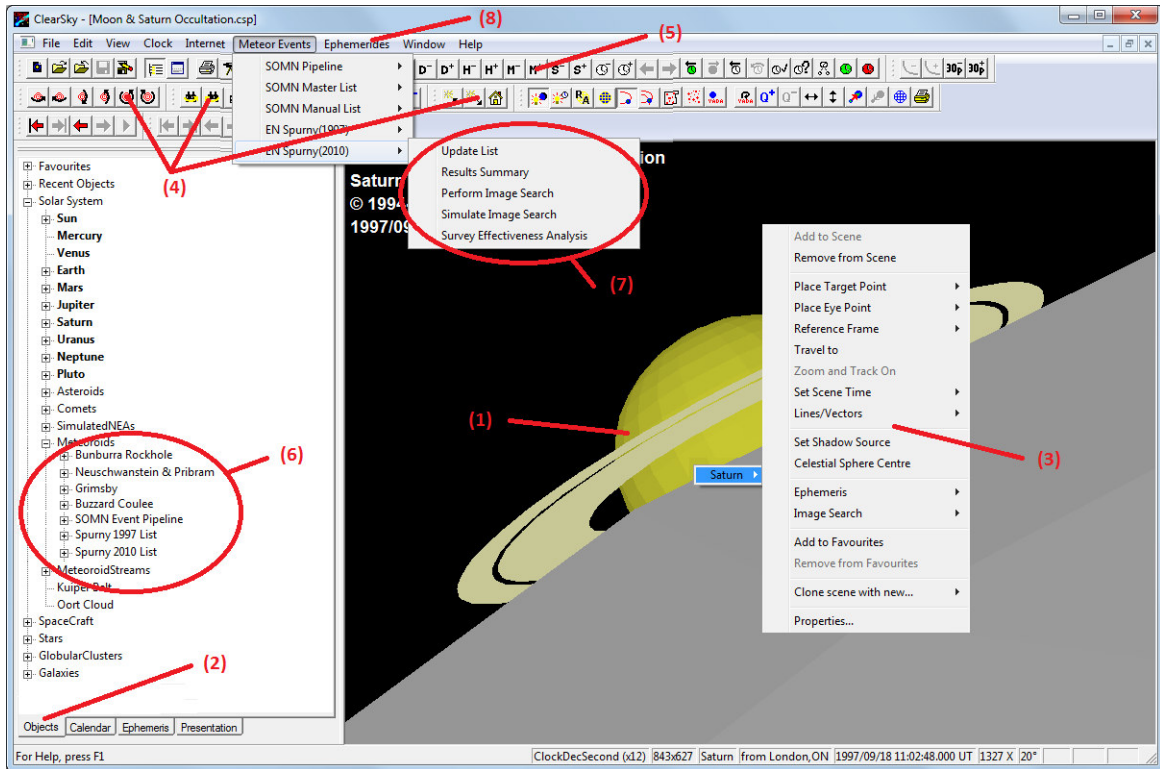
Figure 6-2. The sample of the ClearSky GUI, showing: (1) The interactive scene editor and viewer, (2) the celestial object tree, (3) the object action list available from the scene or the object list, (4) scene manipulation buttons, (5) time control buttons, (6) new meteor and meteor collection support, (7) new image search and sky survey analysis support.

6.2 Meteoroid and Meteoroid Collections

The meteoroid initial state determination and approach integration described in Chapter 4 are automated to allow for the ephemeris generation of probability clouds for individual events and event collections. Each event is described in textual file content as shown in Figure 6-3. This file content includes the object contact epoch, position, radiant and velocity, with error bars for each. The event data may be keyed manually for individual events, as was the case for the Bunburra Rockhole, Grimsby, and Buzzard Coulee events. Alternatively, multiple event data may be loaded en-masse into a single file from a meteor event collection, such as the ASGARD results and the event table in Spurný (1997). Custom plug-in code is written to implement the importing of collection data. To date, plug-ins have been written to import data from the ASGARD

system, and from Microsoft Excel spreadsheets used as a standard bridge format when importing data from papers by data copying or optical character recognition.

```
ClearSky                                            [EN070893(Polnā)]
Meteoroid Collection                                epoch=1993 Aug 07 21h08m15.00000s UT
1.0                                                 eq=J2000.000000
0                                                   orbitformat=Spherical
[EN220293(Meuse)]                                   lon=15.79370000°
epoch=1993 Feb 22 22h12m45.000000s UT               lat=49.41740000°
eq=J2000.000000                                     h=77.19400000 km
orbitformat=Spherical                               ra=278.67000000°
lon=5.50300000°                                     dec=36.01000000°
lat=49.53500000°                                    v=17.61000000 km/s
h=77.30000000 km                                    stddevt=15.000 s
ra=189.40000000°                                    stddevlon=0.00010000°
dec=43.30000000°                                    stddevlat=0.00010000°
v=26.74000000 km/s                                  stddevh=0.00300000 km
stddevt=2.000 s                                     stddevra=0.06000000°
stddevlon=0.00400000°                               stddevdec=0.01400000°
stddevlat=0.00300000°                               stddevv=0.02000000 km/s
stddevh=0.20000000 km                               cloudcount=1000
stddevra=0.20000000°                                diameter=0.3
stddevdec=0.30000000°                               albedo=.2
stddevv=0.09000000 km/s                             slopeparam=.15
cloudcount=1000                                     timestamp=2010/03/21 09:18:00
diameter=1.3                                         EphemerisRequired1=C:\dlc\ClearSky\Data\Spurny(1997)\EN07
albedo=.2                                            0893(Polnā)_30secs_moint_eph.csd
slopeparam=.15                                      EphemerisRequired2=C:\dlc\ClearSky\Data\Spurny(1997)\EN07
timestamp=2010/03/21 09:18:00                       0893(Polnā)_5mins_moint_eph.csd
EphemerisRequired1=C:\dlc\ClearSky\Data\Spurny(1997)\EN2202  EphemerisRequired3=C:\dlc\ClearSky\Data\Spurny(1997)\EN07
93(Meuse)_30secs_moint_eph.csd                      0893(Polnā)_1day_moint_eph.csd
EphemerisRequired2=C:\dlc\ClearSky\Data\Spurny(1997)\EN2202  EphemerisRequired4=C:\dlc\ClearSky\Data\Spurny(1997)\EN07
93(Meuse)_5mins_moint_eph.csd                       0893(Polnā)_2months_moint_eph.csd
EphemerisRequired3=C:\dlc\ClearSky\Data\Spurny(1997)\EN2202
93(Meuse)_1day_moint_eph.csd
EphemerisRequired4=C:\dlc\ClearSky\Data\Spurny(1997)\EN2202
93(Meuse)_2months_moint_eph.csd
```

Figure 6-3. A sample meteoroid collection file showing the definition of two meteor events. Such definitions are keyed manually for individual events, or are loaded en-masse for a given meteoroid collection by custom plug-ins written for those collections. Positional state, error bars in the form of standard deviation, probability cloud size desired, and object physical parameters must be specified for each event. The timestamp field is output by the software to avoid unnecessary rework if a collection load calculation is interrupted, or if minor changes are made to the source collection information. The EphemerisRequired lines are output by the software to identify the placement of the generated probability cloud ephemerides, and force the software to use the ephemerides for any simulation or analysis. Four ephemerides are generated for each event, 30 seconds at 1/30s. intervals, the reminder of the first 5 minutes at 1s. intervals, the remainder of the first day at 1m. intervals, and the remainder of the first 2 months at 1 hr. intervals.

6.3 Meteoroid Path Calculation and Verification

The process of determining the initial meteoroid contact state and probability cloud, and the back-integration of the object for ephemeris generation, is combined into a single operation. For individually keyed meteor events, this process is invoked from the object list of the program GUI. In the case of the batch importing of event collections, the process is performed for each event during the data import. This data import is invoked from the GUI menu which is

augmented with each meteor collection when the collection handling plug-in is implemented. The outputs of the integration process are probability clouds ephemeris files (as described in Figure 6-3), and orbit-at-infinity outputs. The orbital element outputs are collected statistically to arrive at means and standard deviations for each element. In the case of individually keyed events, the mean orbit must be compared manually to published orbits. In the case of collection import, if the published orbital data is provided, the software will automatically provide an orbital results summary comparing calculated and published orbits. Examples of such comparisons were shown and analysed in section 4.6. Figure 6-4 graphically describes the generation of ephemerides and orbital elements.
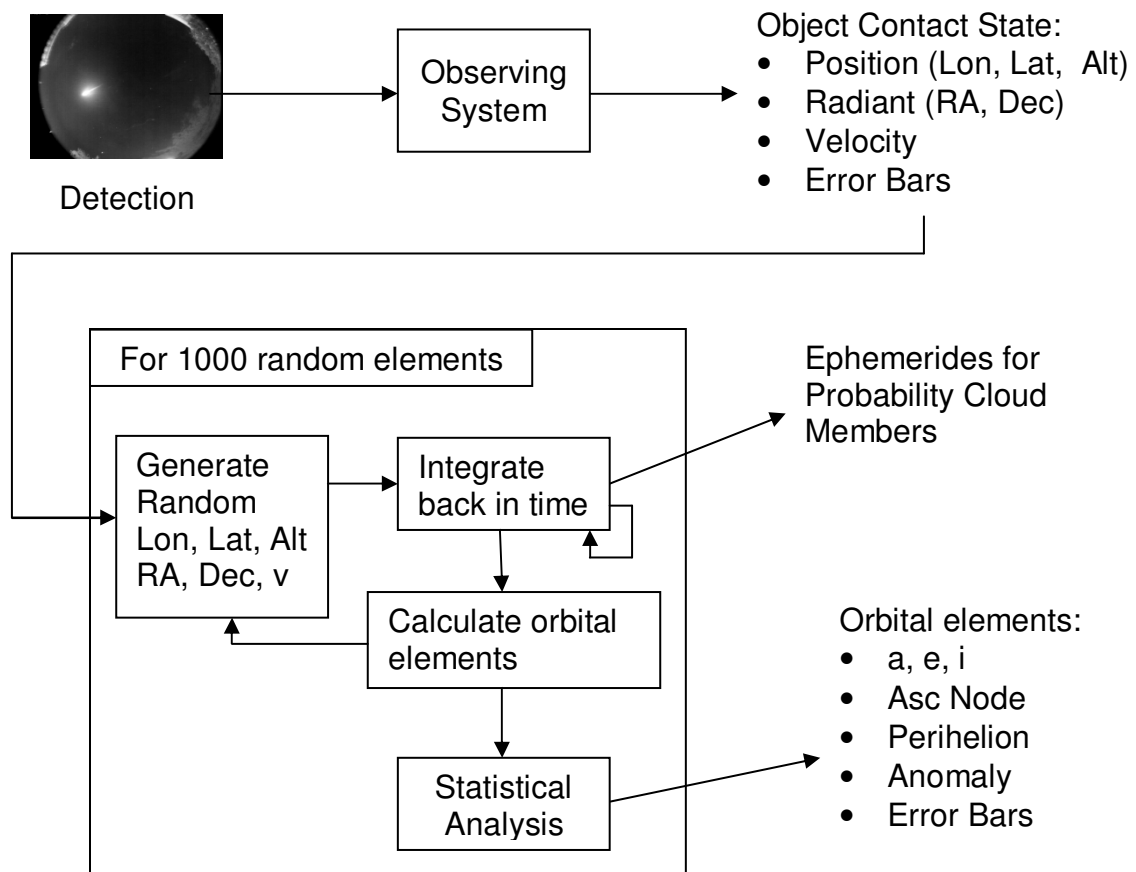
Figure 6-4. The flow of ephemeris and orbital element generation from contact state.

6.4 Survey Image Simulation

A successful search for a sky survey meteoroid image results only in the reporting of candidate image names. The images still require visual scanning. To facilitate the manual search of an image, ClearSky's scene rendering features were enhanced with visual aids: the displaying of significantly more stars from the US Naval Observatory A2.0 database, the displaying of a CCD grid simulating the segmentation of the actual image, and the horizontal and vertical reversals of the image field review as required on a survey-by-survey basis. The first two enhancements are works in progress. The USNO database records red and blue magnitudes for each star. The translation of these magnitudes to stellar discs of appropriate size is not straight forward. As can be seen in the sample image in Figure 6-5, stellar positioning does help orient one on the image, but the representation of relative stellar brightness still requires work. As well, the CCD grid simulation is quite simplistic at this point, only supporting a rectangular pattern of CCD segments. More complex patterns of usable CCD segments (such as the circular grid for Pan-STARRS) are not yet handled.
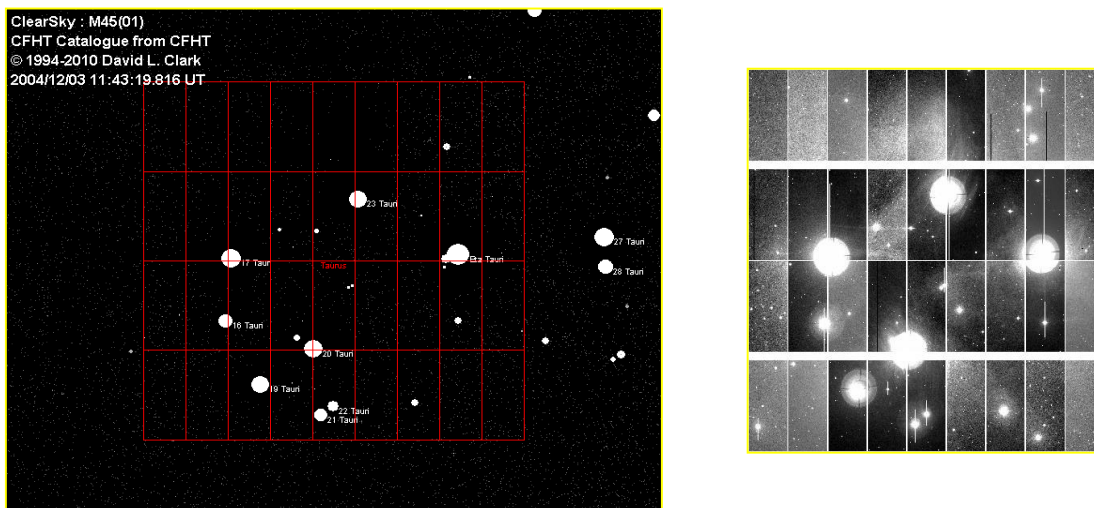
Figure 6-5. A simulated CFHTLS image and the corresponding true image. This sample illustrates the three significant enhancements made to the ClearSky software to improve sky survey image simulation: the inclusion of the USNO stellar database, the simulation of the image CCD grid, and the horizontal and vertical reversal of the field of view.

6.5 Image Searches, Results and Result Verification

Chapter 5 details both the process to periodically download image survey updates, and describes the 3D representation of survey images and how they are tested for object position intersections. The periodic refresh of the image catalogue is triggered by a command-line invocation of ClearSky, triggered by a schedule entry in the host systems task scheduler. The refresh may also be invoked from the GUI main menu, requesting an Internet update as either a specific image catalogue update or as part of an overall ClearSky database update. Image searches are currently always initiated from the GUI, however, a command-line invocation method is being considered as further work.

Meteoroid image searches may be requested in three manners. The GUI main "Meteor Event" menu is used to trigger searches for all events in a given collection over a period of 48 hours prior to the contact time of each event. An image search result file is generated for each event in the collection. The user may also request an individual 48-hour search by selecting a single meteor event item from the program's hierarchical object tree, and requesting a meteor search for that object. Finally, the user may use the general object search technique which may be used for any object in ClearSky's object tree. The user must build a simulation scene containing minimally the Sun, Earth and the object being searched. The user may optionally specify a scene starting and ending date and time, used to contain the time interval searched. If not specified, the entire image catalogue is searched. The user invokes the search by selecting the meteoroid (or other) object and requesting an image search. In the latter two use cases, a single image search result file is created.

Image result files are output in Microsoft Excel format. This format provides integrated text and graphics, with multiple results appearing on easily navigable tabs. The format is readable through readily available and widely used open source programs. Figure 6-6 is an example of an image search result file.

Since it is understood that the chance for successfully detecting an image for any one event is small, an additional step was taken to better guarantee that the search algorithms would identify image of object on a calculated ephemeris. The GUI allows the user to perform a simulated search on any object. This simulated search involves the generation of an ideal sky survey, a simple textual survey catalogue which contains image catalogue entries pointing directly at the object at periodic points along its trajectory. The survey generation code is written independently of the image catalogue load and search code. The simulated search process concludes with a search of the ideal catalogue, providing a search result file containing simulated images over time for those time periods where object observation is possible. Figure 6-6 shows results for an European Network detection as would be viewed from the CFHT under an ideal survey.
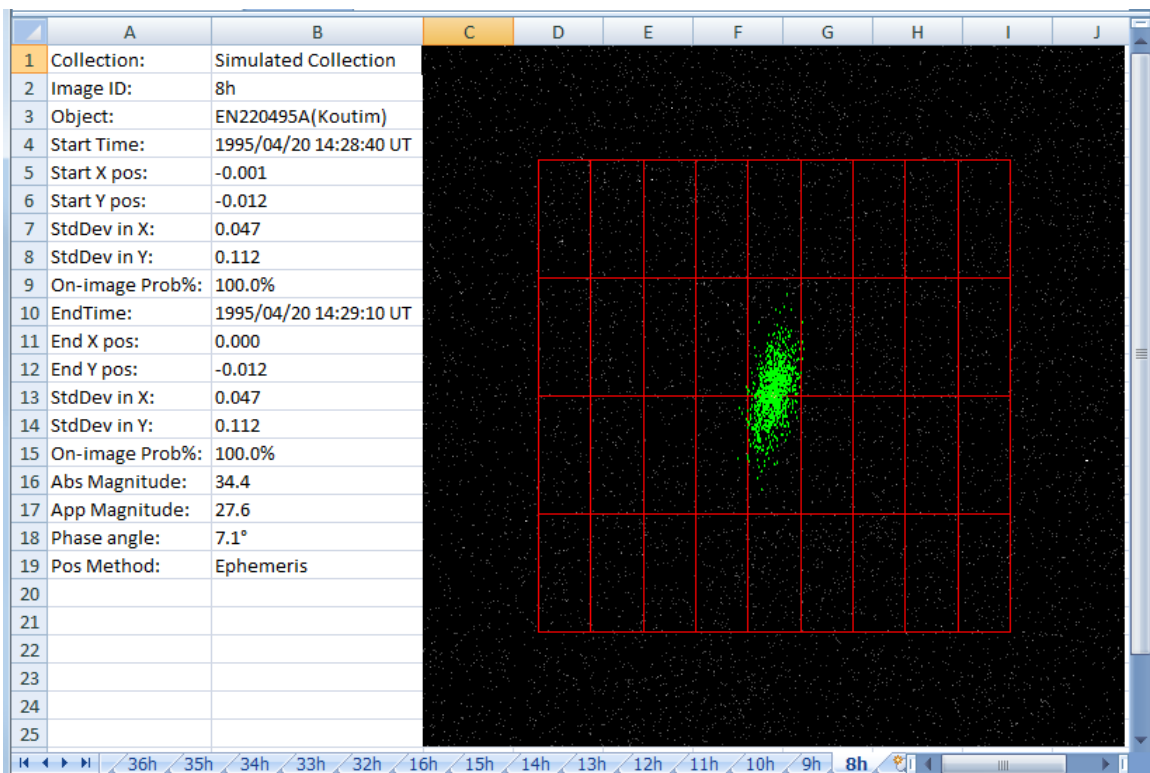
Figure 6-6. Am image survey search result file corresponding to the simulated ideal CFHT survey tracking the object EN220495A (Koutim). The file contains a single tab for each hour prior to contact where solar and object alignments are favourable for observation. The data displayed includes the survey and object identification, the start and end times for a simulated 30 sec. exposure, The mean position and spread of the positional probability cloud on the image (centred at 0,0 with image X and Y coordinates spanning -1 to 1), object magnitude information, and the method used to determine the object position (always "Ephemeris" for integrated meteoroid paths).

6.6 Survey Effectiveness

Extending on the simulation of ideal surveys is the concept of survey effectiveness. Taking any given event, one can compare the ability of telescopic observing systems to detect the event given the object is being tracked by the telescope. Consideration must be given to the object's elevation above the horizon over time, the Sun's angle below the horizon over time, and the object's apparent magnitude based on size, albedo and phase angle. The analysis of survey effectiveness can be done on an individual event, or can be performed over a series of events to arrive at a survey effectiveness measure with respect to a meteor detection program. The ClearSky GUI allows the user to request such an effectiveness survey for a configured set of sky surveys, by event or event collection, over the 48 hour period prior to contact. The mean probability point of the event is tracked at 1-hour intervals with respect to each observatory position. Object elevation, solar elevation, and the object's apparent magnitude are calculated for each point for each survey. The code counts the number of instances where each of the following occur: the object is above 10° in elevation, the Sun is below -15° in elevation, and the object's apparent magnitude is below that of the survey's limiting magnitude. The number of instances where all three scenarios apply is multiplied by the field of view of the survey to arrive at a relative survey effectiveness factor. The results of a survey request are output into a Microsoft Excel spreadsheet, with one tab containing the event-by-event detail across surveys (see Table 6-1), and one tab containing an event collection summarization (see Table 6-2).

Event	CFHT (M=24.0,A=1.0)					SPACEWATCH (M=22.2,A=2.9)					CATALINA (M=19.7,A=9.0)					LINEAR (M=22.0,A=4.0)					Pan-STARRS (M=24.0,A=9.0)					LSST (M=25.0,A=9.6)				
	Alt	Drk	Pos	<M	Vis	Alt	Drk	Pos	<M	Vis	Alt	Drk	Pos	<M	Vis	Alt	Drk	Pos	<M	Vis	Alt	Drk	Pos	<M	Vis	Alt	Drk	Pos	<M	Vis
EN220293(Meuse)	25	20	18	21	9	28	20	20	9	0	28	20	20	2	0	28	22	20	8	0	25	20	18	21	9	10	18	10	33	5
EN070893(Polná)	24	18	16	6	0	26	16	16	2	0	28	16	16	0	0	28	14	14	2	0	24	18	16	6	0	14	22	12	10	0
EN150294(Dresden)	30	20	8	1	0	44	20	16	0	0	44	20	16	0	0	48	22	22	0	0	31	20	8	1	0	0	18	0	2	0
EN070594(Leszno)	20	18	4	2	0	20	16	2	1	0	20	16	2	0	0	19	14	0	1	0	20	18	4	2	0	20	22	4	3	0
EN250594(Ulm)	22	18	0	1	0	22	14	0	0	0	22	14	0	0	0	24	16	0	0	0	22	18	0	1	0	18	22	0	1	0
EN220495A(Koutim)	20	18	18	11	4	20	18	18	4	0	20	18	18	1	0	18	16	16	4	0	20	18	18	11	4	22	22	20	17	5
EN241095B(Odra)	28	22	22	3	0	41	22	22	1	0	43	22	22	0	0	46	22	22	1	0	31	22	22	3	0	0	16	0	5	0
EN251095A(Tisza)	24	20	18	16	5	24	22	20	7	0	24	20	18	2	0	24	20	18	6	0	24	20	18	16	5	18	18	14	25	7
EN231195(J. Hradec)	24	22	20	37	13	28	22	22	16	4	28	22	22	5	0	28	24	24	14	2	24	22	20	37	13	11	14	10	48	10
EN150396(Dobriš II)	23	20	0	2	0	26	20	2	1	0	26	19	2	0	0	28	20	4	1	0	23	20	0	2	0	14	20	0	3	0
Mean:	24.0	19.6	12.4	10.0	3.1	27.9	19.0	13.8	4.1	0.4	28.3	18.7	13.6	1.0	0.0	29.1	19.0	14.0	3.7	0.2	24.4	19.6	12.4	10.0	3.1	12.7	19.2	7.0	14.7	2.7
	Vis x A: 3.1					Vis x A: 1.2					Vis x A: 0.0					Vis x A: 0.8					Vis x A: 27.9					Vis x A: 25.9				

Table 6-1. A detailed survey effectiveness analysis for the 10 largest events from Spurný (1997). For each event and for each survey, the number of hours over the 48 hour period prior to contact are shown for the following observational attributes: Alt = the object is above 10° in elevation, Drk = the Sun is below -15° in elevation, Pos = the object is favourably positioned (both Alt and Drk conditions apply), <M = the object's apparent magnitude is below that of the survey's limiting magnitude, and Vis = the object is visible (Alt, Drk, and <M conditions apply). The limiting magnitude (M) and the survey field of view in degree (A) are shown. The mean effectiveness over all events appears at the bottom, followed by the overall relative effectiveness (Vis x A). Note that this is a statement of survey effectiveness only. Event epochs in this case predate most surveys.

Survey	Alt	Drk	Pos	<M	Vis	Vis x A
CFHT (M=24.0,A=1.0)	24.0	19.6	12.4	10.0	3.1	3.1
SPACEWATCH (M=22.2,A=2.9)	27.9	19.0	13.8	4.1	0.4	1.2
CATALINA (M=19.7,A=9.0)	28.3	18.7	13.6	1.0	0.0	0.0
LINEAR (M=22.0,A=4.0)	29.1	19.0	14.0	3.7	0.2	0.8
Pan-STARRS (M=24.0,A=9.0)	24.4	19.6	12.4	10.0	3.1	27.9
LSST (M=25.0,A=9.6)	12.7	19.2	7.0	14.7	2.7	25.9

Table 6-2. A sample summarized report of survey effectiveness corresponding to Table 6-1.

7 RESULTS

At the time of writing, this project has not yielded a discovery of a PFM image, however, searching will continue. The results of the project have been of a more indirect nature, with our gaining understanding of PFM visibility and the nature of PFM orbits. The project has also contributed to the science with a confirmation of the heavily relied-upon analytical methods of the past 30 years, and by providing a useful general image catalogue search technique.   I summarize these results here, and then present various meteor event and event collection cases.

7.1 Modelling Results

Chapter 3 describes various forms of PFM modelling that all tend to support a pessimistic view of success in associating a fireball event with a survey image. However, the modelling does indicate that candidate objects do exist and object can be visible hours before contact. The question is whether one will be fortunate enough to catch such objects in both meteor and sky survey programs. All modelling performed in this project assumes PFM visibility based on diameter and albedo calculations from Bowell et al. (1989). Assuming a survey limiting magnitude 24, such as the CFHTLS, simple linear approach modelling indicates that brighter (albedo=0.25) 1.0 m objects may be visible from 3 to 48 hours depending on approach angle and speed. Dimmer objects (albedo=0.05) may not be visible at all, and are at most visible for 18 hours.   When we turn to a more sophisticated frequency model based on the NEA dynamical models of Bottke et al. (2002a), fireball size frequency distribution and flux model of Brown et al. (2002), and the albedo model of Morbidelli et al. (2002a), we see that a majority of >0.2 m objects are visible in the minutes prior to contact, but that the proportion of objects visible decreases rapidly over a short period of time. At six hours prior to contact only about 2% of >0.2 m objects would be visible. At 24 hours prior to contact, only a minute fraction are visible. These numbers are more sobering when combined with a rough estimation of large object detection

frequency in meteor observing systems using the Brown et al. (2002) size frequency distribution. We estimate that a >0.2 m. object observation in a system such as ASGARD occurs once every ten years.

7.2 Orbit Determination Results

The validation of the gravitational integration numerical method used in this project involved the comparison of integrated orbits with those calculated by the Ceplecha (1987) analytical method. Table 4-2 and Table 4-3 list the results from two collections of 10 events by Spurný, taken from the paper Spurný (1997) and unpublished data provided by personal correspondence (Spurný, 2010). There is a good correspondence of orbital elements between the analytical and numerical methods. Table 7-1 below summarizes the orbital comparisons.

Event Source	Orbital Element Comparison (not including the longitude of the ascending node)	Proportion in error bars
Spurný (1997)	Analytical results within numerical error bars	9/10
	Numerical results within analytical error bars	6/10
Spurný (2010)	Analytical results within numerical error bars	5/10
	Numerical results within analytical error bars	5/10

Table 7-1. A summary of comparisons of the orbits computed numerically in this project, compared to orbits calculated using the Ceplecha (1987) analytic method. Two collections of 10 events from Spurný (1997) and Spurný (2010) were used. This table disregards a systematic error in longitude of the ascending node, which is explained in the text.

Notable in this table are the significantly better results for the Spurný (1997) data than the newer Spurný (2010). Once the Spurný (2010) data is published, this comparison should be revisited to see if these increased variances persist. If they do, a systematic interpretation-of-data cause would be suspected, and should be investigated.   Regardless, in the case of both collections, variances between the calculation methods seldom go beyond one standard deviation outside the larger of the analytic and numerical error bars. The exceptions are some larger errors noted in inclination and argument of perihelion with the Spurný (2010) data, perhaps related to a systematic error suggested above.   Of additional note are the frequently larger error bars calculated via the numerical methods.   This may suggest an aggressive

evaluation of errors around the Ceplecha methods. It bears mentioning that none of the numerical results speak independently to a better accuracy or precision of the final orbits, as the numerical method is totally dependent on the correctness of the contact state error bars provided.

As explained in detail in section 4.6, there are persistent variances in the longitudes of the ascending node resulting from the Ceplecha and numeric methods. The variances are not large, the largest yet observed being 0.15°, but they are notable because of the extremely tight error bars quoted for this element. The inconsistency is due to the Ceplecha method not accounting for the gravitational impact of the Earth on the ascending node. This amount of shift in the ascending node depends on the trajectory of the object, with a noted preference to draw the ascending node back towards the Earth in the opposite direction of the Earth's travel. In the Ceplecha work, the longitude of the ascending node is used to calculate all other orbital elements with the exception of the semi-major axis. Analysing the impact of the ascending node variance on the other orbital elements is suggested as further work.

7.3 Image search success

The survey image search technique described in Chapter 5 is a generic technique, supporting an abstraction of object positioning calculations. For the purposes of PFM image searches, PFM ephemerides calculated from gravitational integrations are used. However, images of other solar system objects can be searched for by using orbital elements. In support of the article Gilbert and Wiegert (2009) "Searching for main-belt comets using the Canada-France-Hawaii Telescope Legacy Survey", ClearSky was used to search the CFHTLS for images of three main-belt comets: 133P/Elst-Pizzaro, P/2005 U1 (Read), and 176P/LINEAR. Images of 176P/LINEAR were located, including a set of three images dated 2007 January 15. Figure 7-1 shows the image search result file for that period. Figure 7-2 shows the three image simulations, and the

corresponding close inspection images created by Wiegert from CFHTLS image downloads.
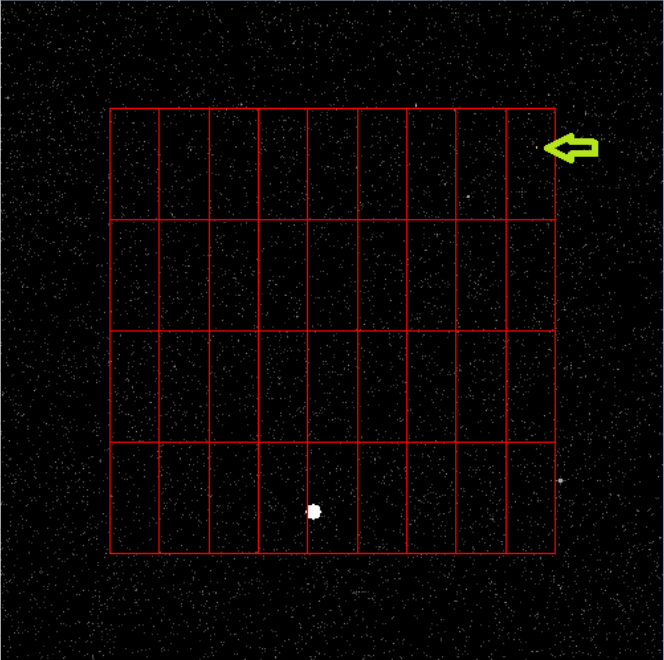
	A	B
1	Collection:	CFHT Catalogue
2	Image ID:	889493
3	Object:	(118401) LINEAR
4	Start Time:	2007/01/15 09:33:29 UT
5	Start X pos:	-0.926
6	Start Y pos:	-0.818
7	StdDev in X:	0.000
8	StdDev in Y:	0.000
9	On-image Prob%:	100.0%
10	EndTime:	2007/01/15 09:35:59 UT
11	End X pos:	-0.925
12	End Y pos:	-0.818
13	StdDev in X:	0.000
14	StdDev in Y:	0.000
15	On-image Prob%:	100.0%
16	Abs Magnitude:	15.1
17	App Magnitude:	19.7
18	Phase angle:	3.7°
19	Pos Method:	Ephemeris
20	@name:	889493
21	@ra:	463953750
22	@dec:	69058900
23	object:	5A10
24	category:	CAL
25	filter:	R.MP9601
26	obstype:	OBJECT
27	crunid:	06BM06
28	runid:	2006BF41
29	@exp:	150.1100006
30	@time:	Jan 15 2007 9:33:29:000AM
31	public_date:	Feb 29 2008 10:00:00:000AM
32	qso_status:	
33	is_phot:	
34	obs_iq_refccd:	
35	procdate:	Feb 17 2007 11:22:18:000AM
36	elixirswv:	2
37	flipssvw:	3
38	URL:	http://www.cadc.hia.nrc.gc.ca/authProxy/getData?archive=CFHT&asf=true&file_id=889493p

Summary | 889493 | 889504 | 889515

Figure 7-1. One image result from the CFHTLS catalogue search result file for 176P/LINEAR for the period of January 2007. Three images were located, the details of each circumstance represented in an Microsoft Excel spreadsheet tab. The result file text contains image description information (including the URL for downloading the CFHTLS image), object visibility, and the position of the object in the image. The X,Y coordinates of the object in the image (ranging from -1 to 1) are reversed due to the orientation of the image. The green arrow has been added to show the position of the object.

Image 889493   Image 889504   Image 889515

2007/01/15 09:33:29 UT   2007/01/15 10:15:40 UT   2007/01/15 10:56:21 UT
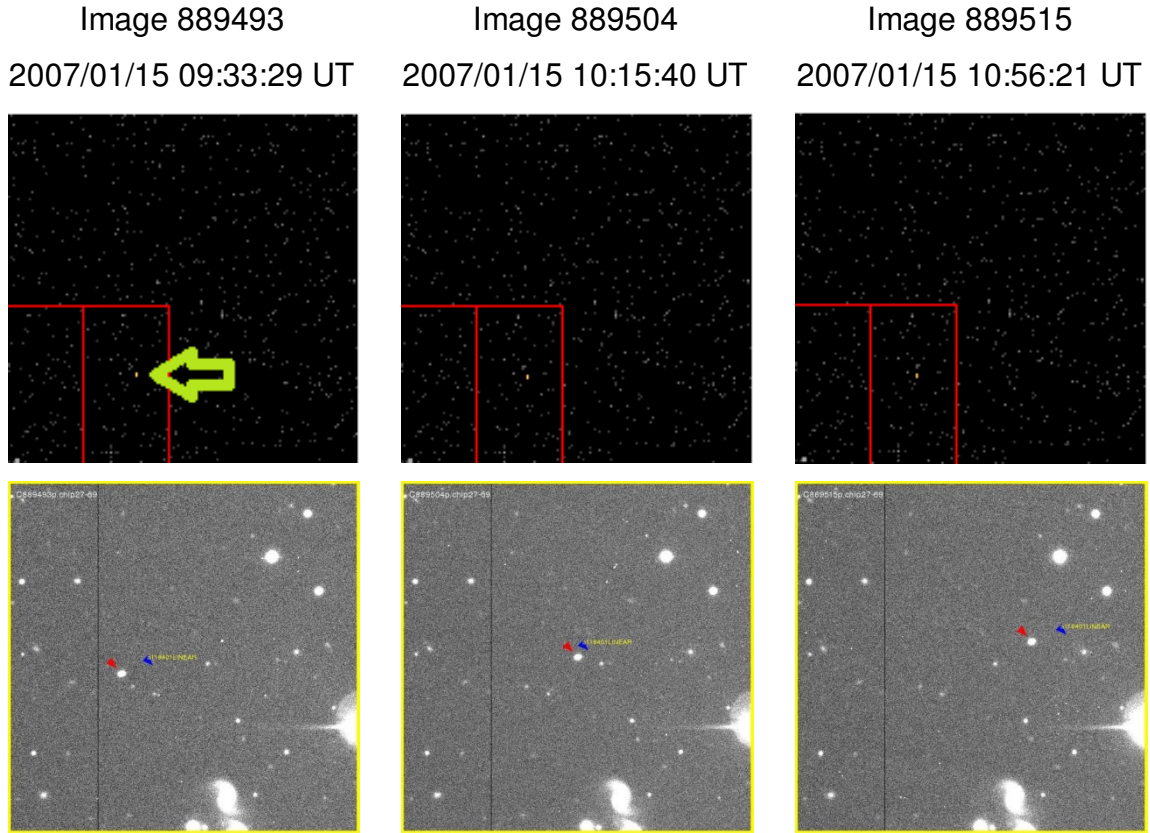
Figure 7-2. Top row: Detail from the three simulated CFHTLS images from 2007 January 15 showing object 176P/LINEAR. The green arrow has been added to highlight the object position. Note the slight movement in the object. Bottom row: Extractions from the actual CFHTLS images created by Dr. Paul Wiegert. The red arrow indicates the actual object; the blue arrow indicated the expected position based on the MPC orbit published at the time. Orientations between the simulations and the extractions are opposite.

7.4 Case Studies

The initial intent of this project was to automate a search of ASGARD objects based on past and current ASGARD observations. As the project progressed, it became evident that sufficiently large ASGARD events were few and far between. Consequently, additional large events were studied, with the intent of confirming published orbits, performing images searches, and analysing various sky surveys for discovering like events. In addition, it became apparent that the analysis of event circumstances with respect to sky survey effectiveness is of interest, both on an event-by-event basis, and in evaluating survey

effectiveness with respect to collective observations from a given observing network. The Individual events and event collections presented here as case studies are:

- The Grimsby event over Ontario in September 2009
- The Bunburra Rockhole event over Australia in July 2007
- The Buzzard Coulee event over Saskatchewan in November 2008
- 10 large events over Central Europe from 1993-1996 from Spurný (1997)
- 10 more recent events recorded by the European Network as provided in Spurný (2010)
- A collection of large events selected from ASGARD

In all cases, a survey effectiveness table is provided. The content of these tables is described in Section 6.6 and Table 6-1.

7.4.1 Grimsby

Reference: McCausland et al. **(2010)**

Circumstances: A bright fireball was observed and detected over South Western Ontario in the evening of September 25, 2009. The object was detected by all-sky camera, radar, and ultrasound systems. The estimated diameter of the object was 0.25 m. with a mass of hundreds of kilograms. Orbital elements have yet to be published, so a comparison of numerically and analytically derived orbits is not provided. The object is believed to be an H5 chondrite.

Contact State:

Epoch:	2009/11/26 01:02:58.15 UT
λ_B	-80.19399 ± .00057°
φ_B	43.53382 ± .00022°
h	100.498 ± .023 km
α_R	248.928 ± .223°

δ_R $55.849 \pm .107°$

v_∞ 20.91 ± 0.19 km/s

Orbital Elements:

Published: Not available.

Calculated by integration:

Epoch:	2009/07/28 01: 02:58.15 UT
a:	2.042 ± 0.0476 AU
e:	0.518 ± 0.011
i:	$28.102 \pm 0.275°$
Ω:	$182.9670 \pm 0.0003°$
ω:	$159.991 \pm 0.276°$
f:	$310.064 \pm 0.321°$

Survey Effectiveness:

Survey	Alt	Drk	Pos	<M	Vis	Vis x A
CFHT (M=24.0,A=1.0)	26	20	6	2	0	0.0
SPACEWATCH (M=22.2,A=2.9)	32	20	10	0	0	0.0
CATALINA (M=19.7,A=9.0)	32	20	10	0	0	0.0
LINEAR (M=22.0,A=4.0)	34	18	10	0	0	0.0
Pan-STARRS (M=24.0,A=9.0)	28	20	8	2	0	0.0
LSST (M=25.0,A=9.6)	0	20	0	3	0	0.0

Table 7-2. The survey effectiveness analysis for the Grimsby event, showing hours of visibility in the 48 hours prior to contact. A full explanation of effectiveness tables is provided in Section 6.6 and Table 6-1.

The survey effectiveness analysis shows that the Grimsby meteoroid, or objects with similar trajectories, had a relatively low chance of being detected. Sealing the fate that such objects would be undetectable is the small size and high apparent magnitude of the object. It is sufficiently close for observation only during the final hours before contact, while it was in the daytime sky for the observatories. Figure 7-3 assists in explaining the low visibility. Grimsby approached the Earth from above and sun-side, placing the object high above the horizon during daylight hours for continental American surveys. When the Earth is viewed from the object, we see the North American and Hawaiian surveys rotating along the right-most limb of the Earth as we travel back in time,

placing the meteoroid near the horizon from the observer's perspective. This effect is worse for the Hawaii surveys, being at lower latitude. As we travel further back in time, observatories rotate into plane view from the object, but they are beginning to approach the terminator, providing few opportunities where the object is sufficiently above the horizon, while the Sun is sufficiently below. Since Grimsby approached from the North, a South American survey such as the LSST would have no opportunity to view such objects.
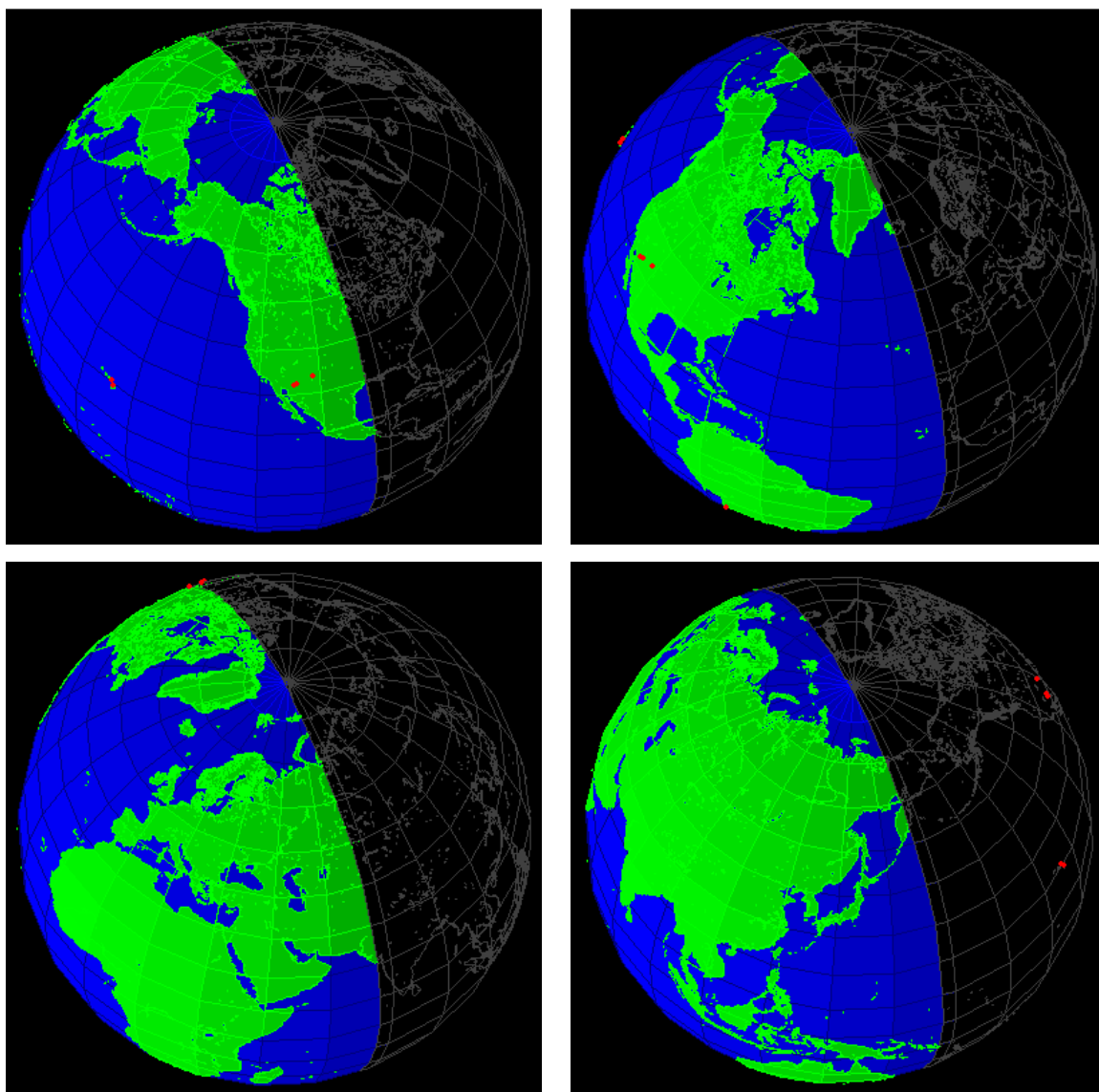
Figure 7-3. The Earth as viewed from the Grimsby meteoroid 1, 6, 12, and 18 hours prior to contact. Observatories referenced in survey effective analyses are shown in red. The size of the Earth is scaled to be the same size in all images.

7.4.2 Bunburra Rockhole

Reference: Bland et al. **(2009)**, Spurný **(2009)**

Circumstances: An approximately .3 m. diameter meteor was detected over south-western Australia by two stations of the Desert Fireball Network. Meteorites have been recovered near the Bunburra Rockhole landmark. The meteorites are classified as basaltic eucrites.

Contact State:

Epoch:	2007 July 20 19:13:53.24 ± .03s UT
λ_B	129.82721 ± .00006°
φ_B	-31.44957 ± .00009°
h	62.833 ± .009 km
α_R	62.704 ± .032°
δ_R	-22.568 ± .030°
v_∞	13.40 ± 0.05 km/s

Orbital Elements:

Published:

a:	0.851 ± 0.002 AU
e:	0.245 ± 0.003
i:	9.07 ± 0.17°
Ω:	297.59525 ± 0.00010°
ω:	209.9 ± 0.2°

Calculated by integration:

Epoch:	2007/05/21 19:14:53.24 UT
a:	0.851 +/- 0.002 AU
e:	0.246 +/- 0.003
i:	9.11 +/- 0.17°
Ω:	297.696 +/- 0.003°
ω:	209.8 +/- 0.2°
f:	85.55 +/- 0.17°

Note that the published and integrated orbits compare well. As previously seen in other examples in this paper, the longitude of the ascending node is the only element outside of the corresponding error bars.

Survey Effectiveness:

Survey	Alt	Drk	Pos	<M	Vis	Vis x A
CFHT (M=24.0,A=1.0)	20	18	0	3	0	0.0
SPACEWATCH (M=22.2,A=2.9)	18	15	0	1	0	0.0
CATALINA (M=19.7,A=9.0)	18	14	0	0	0	0.0
LINEAR (M=22.0,A=4.0)	18	14	0	1	0	0.0
Pan-STARRS (M=24.0,A=9.0)	20	17	0	3	0	0.0
LSST (M=25.0,A=9.6)	22	24	4	5	0	0.0

Table 7-3. The survey effectiveness analysis for the Bunburra Rockhole event, showing hours of visibility in the 48 hours prior to contact. A full explanation of effectiveness tables is provided in Section 6.6 and Table 6 1.
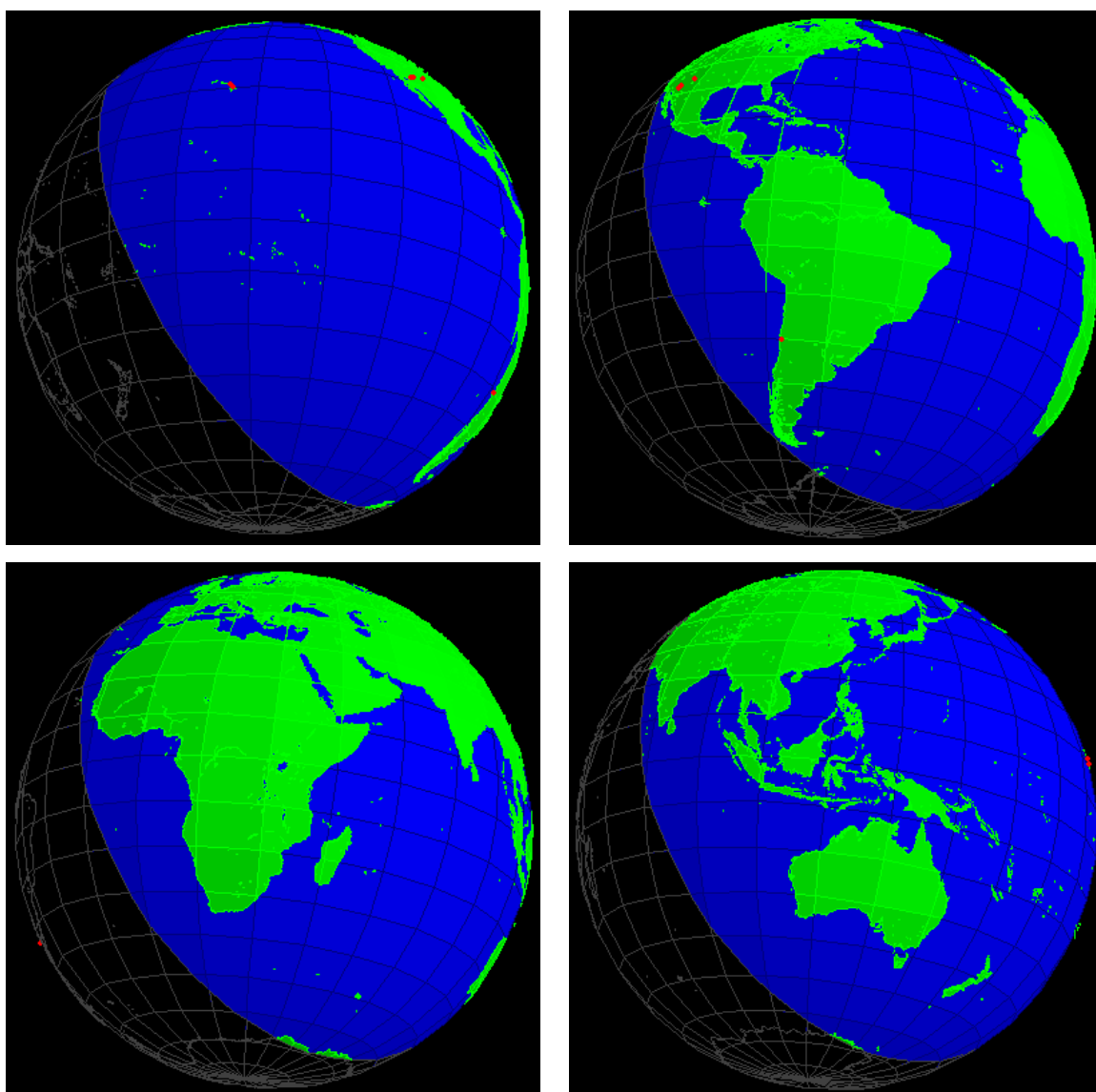
Figure 7-4. The Earth as viewed from the Bunburra Rockhole meteoroid 1, 6, 12, and 18 hours prior to contact. Observatories referenced in survey effective analyses are shown in red. The size of the Earth is scaled to be the same size in all images.

The survey effectiveness survey in Table 7-3, and the accompanying views of Earth in Figure 7-4 demonstrate that the Bunburra Rockhole meteoroid, and meteoroids of like trajectory, are unlikely to be detected. The object approached the Earth sun-side, slightly south, with a very small proportion of the Earth in night-time being able to observe the object. When in the night-time sky, the object would be very close to the horizon. In fact, for North American and Hawaiian telescopes, there are no times when the object is above the horizon while the Sun is sufficiently below. For a South American telescope, such as the LSST, there are only 2 hours per day, or 4 hours in 48, where the Bunburra Rockhole meteoroid could be visible. As with the Grimsby event, Bunburra Rockhole was also too small to be visible for any significant number of hours prior to contact.

7.4.3 Buzzard Coulee

Reference: Hildebrand et al. **(2009)**

Circumstances: In the early evening of November 27, 2008, a bright north-to-south fireball was observed throughout the prairie provinces. The object was detected by all-sky cameras, by shadow casts captured in security videos, and by infrasound. Meteorites were collected near Buzzard Coulee, Saskatchewan. The estimated diameter of the object is 2 m. The meteoroid is classified as an H4 chondrite. Orbital elements have not yet been published.

Contact State:

Epoch:	2008/11/21 00:26:43 UT
λ_B	250.05869 ± .00172°
φ_B	53.16962 ± =.00100°
h	63.920 ± =.081km
α_R	299.980 ± .588°
δ_R	74.966 ± .259°
v_∞	18.0 ± 0.4 km/s

Orbital Elements:

Published: Not available.

Calculated by integration:

Epoch:	2008/09/22 00:26:43 UT
a:	1.246/ +/- 0.028 AU
e:	0.228 +/- 0.017
i:	25.049 +/- 0.759°
Ω:	238.9550 +/- 0.0014°
ω:	211.448 +/- 1.429°
f:	272.052 +/- 1.385°

Survey Effectiveness:

Survey	Alt	Drk	Pos	<M	Vis	Vis x A
CFHT (M=24.0,A=1.0)	36	22	12	35	6	6.0
SPACEWATCH (M=22.2,A=2.9)	48	22	22	15	4	11.6
CATALINA (M=19.7,A=9.0)	48	22	22	4	0	0.0
LINEAR (M=22.0,A=4.0)	48	24	24	13	2	8.0
Pan-STARRS (M=24.0,A=9.0)	37	22	12	35	6	54.0
LSST (M=25.0,A=9.6)	0	14	0	48	0	0.0

Table 7-4. The survey effectiveness analysis for the Buzzard Coulee event, showing hours of visibility in the 48 hours prior to contact. A full explanation of effectiveness tables is provided in Section 6.6 and Table 6 1.

Buzzard Coulee approached the Earth from almost directly over the Earth's North Pole (see Figure 7-5). Being a winter event, a large proportion of the northern hemisphere is in night-time sky. However, with a large number of observatories in lower latitudes, the meteoroid's extreme northern positioning creates observing challenges. For much of the night, the meteoroid hangs close to the horizon, ranging from approximately 10-30° altitude for major North American observatories. Hawaiian telescopes are less favoured with the meteoroid skirting the horizon below the 10° minimum altitude for one half of the night. Even with its relatively large size, the effect of time is notable, with much of the favourable positioning opportunities being lost to the object being too dim. Finally, we note that the observing field is important, as we see the large field of the LSST making Pan-STARRS nine times as effective as CFHT.
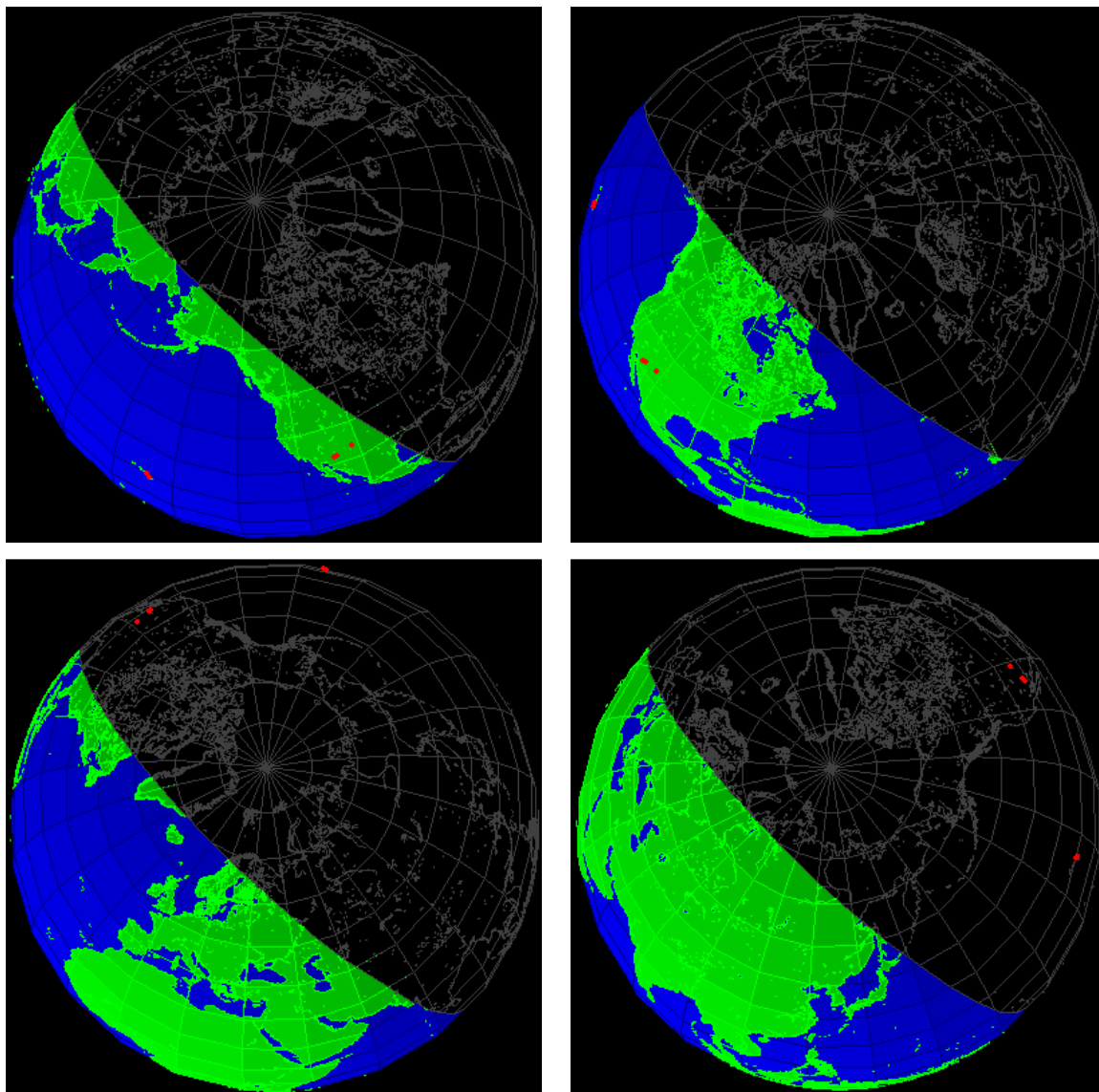
Figure 7-5. The Earth as viewed from the Buzzard Coulee meteoroid 1, 6, 12, and 18 hours prior to contact. Observatories referenced in survey effective analyses are shown in red. The size of the Earth is scaled to be the same size in all images.

7.4.4 European Events (1993-1996)

Reference: Spurný **(1997)**

Introduction:

In his 1997 paper "Exceptional fireballs photographed in central Europe during the period 1993-1996", Spurný provides detailed contact and derived

orbital information on 32 fireballs detected by the European Meteor Network. Although the time period covered by this paper predates most sky surveys, the list of objects does provide well confined data with which a sky survey effective study can be performed with respect to the European Network. The 10 largest objects from the paper were selected, corresponding to those objects with an estimated diameter greater than 0.2 m., the assumed minimum diameter supporting detection in a sky survey image. Table 7-5 and Table 7-6 list the 10 selected objects, with the data describing contact state highlighted.

Contact States and Published Orbits:

Fireball No.	EN220293	EN070893	EN150294	EN070594	EN250594
Name	Meuse	Polnã	Dresden	Leszno	Ulm
Year and Time (UT)	1993 Feb 22 22 h 12 min 45 s ± 2 s[a]	1993 Aug 7 21 h 08 min 15 s ± 15 s[a]	1994 Feb 15 23 h 06 min 23 s ± 5 s	1994 May 7 20 h 03 min 41 s ± 1 s[a]	1994 May 25 21 h 28 min ± 1 min[a]
EN station No.	97, 73, 43, 87, 42	15, 9, 14, 16	3, 20, 9, 11, 20A	9, 14	42, 45, 4, 11
M_p	-17.3	-12.0	-10.6	-8.36	-11.7
m_∞ (kg)	≈3000	37.7	12.9	20.7	≈500
m_E (kg)	2.7	≈0.1	<0.05	<0.01	0
v_B (km s^{-1})	26.73 ± 0.09	17.60 ± 0.02	23.890 ± 0.008	13.71 ± 0.02	15.63 ± 0.03
h_B (km)	77.3 ± 0.2	77.194 ± 0.003	81.64 ± 0.06	63.56 ± 0.04	80.6 ± 0.2
λ_B °	5.503 ± 0.004	15.7937 ± 0.0001	14.1013 ±0.0010	15.4953 ± 0.0002	9.012 ± 0.003
φ_B °	49.535 ± 0.003	49.4174 ± 0.0001	51.3766 ± 0.0004	51.4614 ± 0.0004	48.708 ± 0.002
v_E (km s^{-1})	7. ± 2.	5.7 ± 0.4	4.0 ± 0.9	8.6 ± 0.3	8. ± 1.
h_E (km)	21.5 ± 0.4	29.407 ± 0.004	34.04 ± 0.06	42.71 ± 0.04	47.5 ± 0.2
λ_E °	4.892 ± 0.006	15.8955 ± 0.0002	13.7854 ± 0.0011	16.3124 ± 0.0002	11.537 ± 0.002
φ_E °	49.436 ± 0.005	49.5156 ± 0.0001	50.8371 ± 0.0005	51.5637 ± 0.0004	47.480 ± 0.002
l (km)	72.3	49.60	80.20	61.95	242.24
t (s)	3.2	3.36	4.46	5.14	23.45
$(Z_R°)_E$	39.7 ± 0.4	15.600 ± 0.013	53.852 ± 0.013	70.6 ± 0.3	83.2 ± 0.2
σ (s^2 km^{-2})	0.011 ± 0,002	0.014 ± 0.002	0.0130 ± 0.0002	0.048 ± 0.005	0.225 ± 0.004
PE	-5.24	-4.81	-4.53	-5.06	-4.79
Type	I	I	I	II	IIIA
α_R°	189.4 ± 0.2	278.67 ± 0.06	273.96 ± 0.03	113.3 ± 0.3	102.9± 0.3
δ_R°	43.3 ± 0.3	36.01 ± 0.014	69.41 ± 0.02	8.5 ± 0.3	29.35 ± 0.07
v_∞ (km s^{-1})	26.74 ± 0.09	17.61 ± 0.02	23.849 ±0.008	14.01 ± 0.02	15.70 ± 0.03
α_G°	191.3 ± 0.2	276.25 ± 0.07	280.81 ± 0.03	101.4 ± 0.3	92.9 ± 0.3
δ_G°	42.7 ± 0.3	34.12 ± 0.02	67.01 ± 0.02	-6.3 ± 0.3	15.79 ± 0.11
v_G (km s^{-1})	24.09 ± 0.10	13.70 ± 0.02	21.002 ± 0.010	8.93 ± 0.04	11.43 ± 0.04
v_H (km s^{-1})	35.69 ± 0.10	36.15 ± 0.02	37.636 ± 0.007	36.56 ± 0.05	36.28 ± 0.05
a (AU)	1.50 ± 0.02	2.003 ± 0.006	2.338 ± 0.003	2.10 ± 0.02	2.04 ± 0.02
e	0.567 ± 0.004	0.5162 ± 0.0013	0.5783 ± 0.0006	0.532 ± 0.004	0.560 ± 0.003
q (AU)	0.651 ± 0.004	0.9691 ± 0.0002	0.9859 ± 0.0001	0.9842 ± 0.0005	0.8978 ± 0.0010
Q (AU)	2.36 ± 0.03	3.038 ± 0.011	3.690 ± 0.007	3.22 ± 0.04	3.18 ± 0.03
ω°	266.9 ± 0.8	209.52 ± 0.07	173.90 ± 0.02	338.2 ± 0.2	313.1 ± 0.3
Ω°	334.4071 ± 0.0001	135.4415 ± 0.0002	327.1296 ± 0.0001	227.1096 ± 0.0001	244.5262 ± 0.0007
i°	32.6 ± 0.2	18.90 ± 0.03	33.841 ± 0.012	6.91 ± 0.07	2.50 ± 0.04
Shower			δ Draconid?		
Note	[a] time from visual observation	[a] time from visual observation		[a] time from very precise visual observation	[a] visual time breaks in second part are blurred

Table 7-5. 5 of the 10 largest mass events from Spurný (1997) "Exceptional fireballs photographed in central Europe during the period 1993-1996." Trajectory back-integrations were performed using the highlighted data (time, height, latitude, longitude, radian right ascension and declination, and contact speed).

Fireball No.	EN220495A	EN241095B	EN251095A	EN231195	EN150396
Name	Koutim	Odra	Tisza	J. Hradec	Dobříš II
Year and Time (UT)	**1995 Apr 22 22 h 28 min 40 s ± 3 s**	**1995 Oct 24 21 h 01 min ± 1 min[a]**	**1995 Oct 25 2 h 25 min 53 s ± 1 s[a]**	**1995 Nov 23 1 h 29 min ± 1 min[a]**	**1996 March 15 19 h 24 min 36 s ± 9 s[a]**
EN station No.	20, 15,9, 17, 4, 11, 14, 16, 12, 20A	14, 16, 9, 11, 15, 3	16, 14, 9, 20, 15, 20H, 20A	9, 14, 16, 12	14, 85, 88
M_p	-13.1	-12.6	-16.1	-16.9	-14.9
m_∞ (kg)	109	39	890	3600	620
m_E (kg)	<0.1	<0.01	26[b]	2.[b]	<0.1
v_B (km s^{-1})	27.531 ± 0.006	33.12 ± 0.10	29.22 ± 0.04	22.197 ± 0.013	19.1 ± 0.2
h_B (km)	89.01 ± 0.03	71.9 ± 0.3	80.54 ± 0.10	93.79 ± 0.05	73.6 ± 0.9
λ_B °	15.3106 ± 0.0005	17.168 ± 0.009	20.197 ± 0.002	14.1185 ± 0.0008	13.392 ± 0.013
φ_B °	49.2208 ± 0.0002	51.965 ± 0.005	47.4624 ± 0.0012	49.2463 ± 0.0006	50.07 ± 0.02
v_E (km s^{-1})	5.3 ± 0.5	11. ± 2.	12.1 ± 0.8	0.93 ± 0.13	3.9 ± 1.1
h_E (km)	29.69 ± 0.04	29.7 ± 0.3	26.5 ± 0.2	20.40 ± 0.04	34.2 ± 0.6
λ_E °	14.9880 ± 0.0007	16.984 ± 0.009	20.688 ± 0.003	1 4.9579 ± 0.0007	14.412 ± 0.007
φ_E °	50.0091 ± 0.0003	51.8274 ± 0.005	47.716 ± 0.002	49. 1576 ± 0.0006	49.729 ± 0.011
l (km)	109.10	46.72	71.57	96.40	92.2
t (s)	4.78	1.61	2.76	6.74	5.8
$(Z_R°)_E$	57.474 ± 0.009	25.48 ±0.02	41.1 ± 0.2	40.703 ± 0.012	65.0 ± 0.9
σ (s^2 km^{-2})	0.0098 ± 0.0005	0.0120 ±0.001	0.0031 ± 0.0009	0.0190 ± 0.0007	0.047 ± 0.002
PE	-4.47	-4.43	-4.64	-4.67	-5.12
Type	I	I	I	I	II
α_R°	215.36 ± 0.02	47.8 ± 0.3	57.0 ± 0.2	41.6 ± 0.3	25.7 ± 0.7
δ_R°	-6.397 ± 0.009	66.17 ± 0.02	16.87 ±0.10	40.09 ± 0.02	36.6 ± 1.3
v_∞ (km s^{-1})	27.534 ± 0.006	33.17 ± 0.10	29.23 ± 0.04	22.200 ± 0.013	19.1 ± 0.2
α_G°	215.23 ± 0.02	48.7 ± 0.3	55.5 ± 0.2	37.8 ± 0.3	19.7 ± 07
δ_G°	-9.167 ± 0.010	66.66 ± 0.02	15.40 ± 0.10	37.97 ± 0.02	30.8 ± 1.5
v_G (km s^{-1})	25.117 ± 0.006	31.16 ± 0.11	27.21 ± 0.04	19.43 ± 0.02	15.8 ± 0.2
v_H (km s^{-1})	37.299 ± 0.009	33.40 ± 0.08	30.99 ± 0.10	39.18 ± 0.06	40.7 ± 0.2
a (AU)	2.374 ± 0.004	1.327 ± 0.011	1.077 ± 0.009	3.39 ± 0.05	7.2 ± 1.1
e	0.7878 ± 0.0003	0.571 ± 0.002	0.8067 ± 0.0010	0.779 ± 0.003	0.88 ± 0.02
q (AU)	0.5039 ± 0.0003	0.569 ± 0.002	0.208 ± 0.002	0.749 ± 0.002	0.892 ± 0.004
Q (AU)	4.245 ± 0.008	2.08 ± 0.02	1.946 ± 0.014	6.03 ± 0.10	13. ± 2.
ω°	277.58 ± 0.05	280.2 ± 0.4	140.4 ± 0.4	243.3 ± 0.3	141.2 ± 0.9
Ω°	32.3858 ± 0.0001	211.0381 ± 0.0007	31.2595 ± 0.0001	240.3362 ± 0.0007	355.5530 ± 0.0001
i°	4.119 ± 0.012	52.8 ± 0.2	6.2 ± 0.2	11.99 ± 0.02	8.3 ± 0.5
Shower				Andromedid?	
Note	1 grating and 2 prism spectra, very probably ordinary chondrite	a used time is from only one uncertain visual observation	a reliable visual time b meteorite fall is very probable	a visual time b meteorite fall is quite certain	a time from visual observation

Table 7-6. A continuation of Table 7-5 with the remaining 5 of the 10 largest mass events from Spurný (1997)

Survey Effectiveness:

	CFHT (M=24.0,A=1.0)					SPACEWATCH (M=22.2,A=2.9)					CATALINA (M=19.7,A=9.0)					LINEAR (M=22.0,A=4.0)					Pan-STARRS (M=24.0,A=9.0)					LSST (M=25.0,A=9.6)				
Event	Alt	Drk	Pos	<M	Vis	Alt	Drk	Pos	<M	Vis	Alt	Drk	Pos	<M	Vis	Alt	Drk	Pos	<M	Vis	Alt	Drk	Pos	<M	Vis	Alt	Drk	Pos	<M	Vis
EN220293(Meuse)	25	20	18	21	9	28	20	20	9	0	28	20	20	2	0	28	22	20	8	0	25	20	18	21	9	10	18	10	33	5
EN070893(Polnă)	24	18	16	6	0	26	16	16	2	0	28	16	16	0	0	28	14	14	2	0	24	18	16	6	0	14	22	12	10	0
EN150294(Dresden)	30	20	8	1	0	44	20	16	0	0	44	20	16	0	0	48	22	22	0	0	31	20	8	1	0	0	18	0	2	0
EN070594(Leszno)	20	18	4	2	0	20	16	2	1	0	20	16	2	0	0	19	14	0	1	0	20	18	4	2	0	20	22	4	3	0
EN250594(Ulm)	22	18	0	1	0	22	14	0	0	0	22	14	0	0	0	24	16	0	0	0	22	18	0	1	0	18	22	0	1	0
EN220495A(Koutim)	20	18	18	11	4	20	18	18	4	0	20	18	18	1	0	18	16	16	4	0	20	18	18	11	4	22	22	20	17	5
EN241095B(Odra)	28	22	22	3	0	41	22	22	1	0	43	22	22	0	0	46	22	22	1	0	31	22	22	3	0	0	16	0	5	0
EN251095A(Tisza)	24	20	18	16	5	24	22	20	7	0	24	20	18	2	0	24	20	18	6	0	24	20	18	16	5	18	18	14	25	7
EN231195(J. Hradec)	24	22	20	37	13	28	22	22	16	4	28	22	22	5	0	28	24	24	14	2	24	22	20	37	13	11	14	10	48	10
EN150396(Dobříš II)	23	20	0	2	0	26	20	2	1	0	26	19	2	0	0	28	20	4	1	0	23	20	0	2	0	14	20	0	3	0
Mean:	24.0	19.6	12.4	10.0	3.1	27.9	19.0	13.8	4.1	0.4	28.3	18.7	13.6	1.0	0.0	29.1	19.0	14.0	3.7	0.2	24.4	19.6	12.4	10.0	3.1	12.7	19.2	7.0	14.7	2.7
	Vis x A:	3.1				Vis x A:	1.2				Vis x A:	0.0				Vis x A:	0.8				Vis x A:	27.9				Vis x A:	25.9			

Table 7-7. The survey effectiveness analysis for the 10 largest events from Spurný (1997) showing hours of visibility in the 48 hours prior to contact. A full explanation of effectiveness tables is provided in Section 6.6 and Table 6-1.

Survey	Alt	Drk	Pos	<M	Vis	Vis x A
CFHT (M=24.0,A=1.0)	24.0	19.6	12.4	10.0	3.1	3.1
SPACEWATCH (M=22.2,A=2.9)	27.9	19.0	13.8	4.1	0.4	1.2
CATALINA (M=19.7,A=9.0)	28.3	18.7	13.6	1.0	0.0	0.0
LINEAR (M=22.0,A=4.0)	29.1	19.0	14.0	3.7	0.2	0.8
Pan-STARRS (M=24.0,A=9.0)	24.4	19.6	12.4	10.0	3.1	27.9
LSST (M=25.0,A=9.6)	12.7	19.2	7.0	14.7	2.7	25.9

Table 7-8. A summarized effectiveness analysis corresponding to Table 7-7.

The effectiveness of sky surveys in detecting the Spurný (1997) meteoroids varies significantly from event to event. Of particular note are Dresden, Lezno, Ulm and Dobříš II which appear to be Sun-side approaches. These meteoroids' visibility is severely constrained by the relatively few periods of time where the object at a favourable altitude while the observatory is in darkness. In stark comparison, the other meteoroids' visibility is hardly impacted by solar elevation at all. The solar elevation effect on Dresden is noticeably less for Hawaii-based telescopes than for North and South American telescopes, indicating an improved visibility due to longitudinal approach angle. The wide variation of visibility profiles indicates that individual approach circumstances have a great impact on visibility. A quick look at the LSST and Pan-STARRS effectiveness shows an almost across-the-aboard impact on the altitudinal component of visibility, indicating support for what might seem an obvious bias against telescope observations of northern events from southern surveys. However, two factors serve to increase LSST effectiveness. Close inspection of meteoroid magnitudes show that the small increase in limiting magnitude from M=24 to M=25 captures a number of meteoroids with magnitudes within that range over later hours of visibility. As well, the large field of view increases LLST effectiveness, approximating that of Pan-STARRS.

7.4.5 European Events (1999-2007)

Reference: Spurný **(2010)**

Introduction:

The recognition that few significant events had been recorded by the South-western Ontario ASGARD system, and the success of duplicating analytical results from the Spurný (1997) collection led to a request to Spurný for data on more recent events from the European Network. Spurný provided unpublished contact state and orbital information on 10 significant events.

Table of Events:

Meteor No.	DATE	Geocentric radiant (J2000.0)			Orbital elements (J2000.0)							Type /Orbital origin	Apparent radiant	
		RA (deg)	DE (deg)	V_G (km/s)	a (AU)	e	q (AU)	w (deg)	W (deg)	i (deg)	TP_J		RA (deg)	DE (deg)
EN210199	21.1.1999	13.2 ± 1.5	83.07 ± 0.18	11.99 ± 0.05	1.73 ± 0.011	0.44 ± 0.003	0.9694 ± 0.0003	198 ± 0.2	301.2713 ± 0.0007	17.56 ± 0.06		a/a	36.1616 ± 0.8544	79.4351 ± 0.1570
EN310800	31.8.2000	117.79 ± 0.07	69.69 ± 0.03	9.816 ± 0.006	0.7969 ± 0.0002	0.2958 ± 0.0003	0.5612 ± 0.0004	19.13 ± 0.03	158.8169 ± 0.00001	16.74 ± 0.02		a/a	91.3351 ± 0.0740	76.5341 ± 0.0290
EN171101	17.11.2001	48.71 ± 0.14	34.3 ± 0.3	14.46 ± 0.02	1.326 ± 0.004	0.4844 ± 0.0011	0.684 ± 0.0011	266.8 ± 0.2	235.3927 ± 0.00002	7.41 ± 0.13		a/a	43.1453 ± 0.1283	37.5387 ± 0.2537
EN060402	6.4.2002	192.33 ± 0.03	19.54 ± 0.04	17.51 ± 0.05	2.4 ± 0.02	0.67 ± 0.002	0.7929 ± 0.0004	241.2 ± 0.06	16.82664 ± 0.00001	11.41 ± 0.03		a/a	190.6207 ± 0.0147	21.9712 ± 0.0134
EN170702	17.7.2002	310.68 ± 0.05	2.78 ± 0.06	17.485 ± 0.010	1.0002 ± 0.0011	0.5343 ± 0.0004	0.4658 ± 0.0007	303.7 ± 0.11	115.1884 ± 0.00001	14.12 ± 0.04		a/a	311.563 ± 0.0511	6.6323 ± 0.0507
EN290903	29.9.2003	0.85 ± 0.03	10.77 ± 0.03	20.481 ± 0.007	2.019 ± 0.004	0.7027 ± 0.0004	0.6001 ± 0.0004	268.4 ± 0.07	185.454 ± 0.00001	6.48 ± 0.02		a/a	3.5075 ± 0.0324	13.7641 ± 0.0314
EN280506	28.5.2006	241.37 ± 0.01	-15 ± 0.02	13.65 ± 0.007	1.3936 ± 0.0006	0.4691 ± 0.0003	0.73983 ± 0.00015	261.1 ± 0.03	67.41318 ± 0.00007	2.55 ± 0.01	7.14	a/a	243.4151 ± 0.0133	-7.0082 ± 0.0176
EN231006	23.10.2006	35.59 ± 0.05	14.72 ± 0.03	26.58 ± 0.02	2.39 ± 0.01	0.8226 ± 0.0007	0.4247 ± 0.0006	285.7 ± 0.09	210.281 ± 0.003	0.53 ± 0.03	3.85	a/a	36.6319 ± 0.0442	16.1281 ± 0.0251
EN040207	4.2.2007	133.6 ± 0.02	29.98 ± 0.02	19.04 ± 0.04	2.34 ± 0.01	0.6997 ± 0.0015	0.7032 ± 0.0004	252.3 ± 0.03	315.6472 ± 0.00001	6.92 ± 0.02	4.33	c/a!	134.8135 ± 0.0173	31.267 ± 0.0209
EN300807	30.8.2007	295.24 ± 0.10	12.9 ± 0.10	12.59 ± 0.01	2.529 ± 0.009	0.629 ± 0.001	0.9381 ± 0.0004	215.3 ± 0.11	157.0605 ± 0.00001	11.06 ± 0.03	4.25	a/a	299.7257 ± 0.0944	18.2077 ± 0.0896

Table 7-9. Unpublished radiant and orbital element data from Spurný (2010) for 10 bright European Network fireball events from 1999-2007. Trajectory back-integrations were performed using the highlighted date and radiant data.

Meteor No.	Time* (UT)	H_B (km)	λ_B (deg)	φ_B (deg)	H_E (km)	λ_E (deg)	φ_E (deg)	L_{obs} (km)	ZD_E (deg)	V_{inf} (km/s)	M_{max}	m_{inf} (kg)	PE	Type
EN210199	18:05:00	80.38	18.79	50.14	20.67	18.834	49.835	68.87	29.7	16.3389±0.0339	-18	≈1000	-4.8	II
EN310800	22:51:56.0	81.82	14.0843	49.5048	21.46	13.8251	48.9407	89.47	47.88	14.9150±0.0041	-13.8	105	-4.29	I
EN171101	16:52:46.7	81.37	23.7428	48.9196	13.5	26.671	48.733	106.43	51.7	18.4825±0.0138	-18.5	4300	-4.27	I
EN060402	20:20:17.7	84.95	11.5524	47.3039	16.04	10.8507	47.5257	90.6	40.77	20.9460±0.0400	-17.2	300	-3.98	I
EN170702	23:51:01.5	87.14	17.3698	49.8902	30.12	17.3543	50.3722	78.61	43.74	20.7277±0.0088	-14.6	410	-4.96	II
EN290903	01:20:12.6	89.39	18.2982	49.6852	30.53	19.1283	50.0056	91.59	50.33	23.1116±0.0064	-14.7	420	-4.85	II
EN280506	23:16:42.0	88.04	15.8335	50.4327	30.5	16.0474	51.2503	109.41	58.68	17.5755±0.0050	-11.4	65	-4.59	I (II)
EN231006	23:38:06.0	78.05	18.6956	48.2487	25.86	18.8195	48.5405	62.28	33.23	28.7781±0.0230	-13.3	98	-4.28	I
EN040207	22:59:15.0	86.1	16.9313	48.7966	32.69	16.9501	48.9475	56.06	17.73	22.0526±0.0307	-18	1000	-5.44	IIIA
EN300807	22:17:43.1	72.91	18.2469	48.8046	26.96	18.6546	49.0202	60.03	40.21	16.6560±0.0090	-10.9	26	-4.4	I

Table 7-10. Unpublished atmospheric trajectory data from Spurný (2010) for 10 bright European Network fireball events from 1999-2007. Trajectory back-integrations were performed using the highlighted time, longitude, latitude and velocity data. Note that errors in longitude and latitude are not provided. According to Spurný, these errors are accounted for in the radiant errors in Table 7-9.

Survey Effectiveness:

Event	CFHT (M=24.0,A=1.0)					SPACEWATCH (M=22.2,A=2.9)					CATALINA (M=19.7,A=9.0)					LINEAR (M=22.0,A=4.0)					Pan-STARRS (M=24.0,A=9.0)					LSST (M=25.0,A=9.6)				
	Alt	Drk	Pos	<M	Vis	Alt	Drk	Pos	<M	Vis	Alt	Drk	Pos	<M	Vis	Alt	Drk	Pos	<M	Vis	Alt	Drk	Pos	<M	Vis	Alt	Drk	Pos	<M	Vis
EN210199	40	20	18	16	10	48	24	24	7	3	48	24	24	2	0	48	22	22	6	1	40	20	18	16	10	0	16	0	26	0
EN310800	32	20	12	4	0	48	16	16	2	0	48	16	16	0	0	48	18	18	2	0	32	20	12	4	0	0	22	0	7	0
EN171101	23	22	21	42	21	27	22	22	18	11	27	22	22	5	1	27	22	22	16	11	23	22	21	42	21	12	16	12	48	12
EN060402	23	18	18	13	8	24	18	18	5	0	24	18	18	0	0	24	18	18	4	0	23	18	18	13	8	17	20	17	21	8
EN170702	21	16	16	16	7	22	16	16	7	0	21	16	16	2	0	22	14	14	6	0	21	16	16	16	7	21	22	20	25	10
EN290903	22	20	20	18	8	24	18	18	7	0	23	19	19	0	0	24	20	20	6	0	22	20	20	18	8	20	18	18	29	10
EN280506	20	18	17	9	0	20	14	14	0	0	20	14	14	0	0	20	14	14	0	0	19	18	17	9	0	23	24	21	18	4
EN231006	22	20	20	9	1	23	20	20	0	0	23	20	20	0	0	24	22	22	0	0	22	20	20	9	1	20	18	18	17	3
EN040207	22	20	19	21	9	27	22	21	7	0	27	22	21	0	0	28	22	22	6	0	23	20	19	21	9	16	18	14	36	7
EN300807	21	18	13	0	0	22	18	14	0	0	22	18	14	0	0	23	18	13	0	0	21	18	13	0	0	21	20	13	5	0
Mean:	24.6	19.2	17.4	14.8	6.4	28.5	18.8	18.3	5.3	1.4	28.3	18.9	18.4	0.9	0.1	28.8	19.0	18.5	4.6	1.2	24.6	19.2	17.4	14.8	6.4	15.0	19.4	13.3	23.2	5.4
Vis x A:				6.4					4.1					0.9					4.8					57.6					51.8	

Table 7-11. The survey effectiveness analysis for the events from Spurný (2010) showing hours of visibility in the 48 hours prior to contact. A full explanation of effectiveness tables is provided in Section 6.6 and Table 6 1.

Survey	Alt	Drk	Pos	<M	Vis	Vis x A
CFHT (M=24.0,A=1.0)	24.6	19.2	17.4	14.8	6.4	6.4
SPACEWATCH (M=22.2,A=2.9)	28.5	18.8	18.3	5.3	1.4	4.1
CATALINA (M=19.7,A=9.0)	28.3	18.9	18.4	0.9	0.1	0.9
LINEAR (M=22.0,A=4.0)	28.8	19.0	18.5	4.6	1.2	4.8
Pan-STARRS (M=24.0,A=9.0)	24.6	19.2	17.4	14.8	6.4	57.6
LSST (M=25.0,A=9.6)	15.0	19.4	13.3	23.2	5.4	51.8

Table 7-12. A summarized effectiveness analysis corresponding to Table 7-11.

Survey effective numbers for the Spurný (2010) collection parallel those for Spurný (1997). Specifically, we see variability of visibility by event and altitudinal bias against the southerly LSST survey for northern events compensated by increased field and limiting magnitude.

7.4.6 Large ASGARD Events

Introduction:

The intended selections of ASGARD events for survey image searching was somewhat hampered by the small number of large candidate events. In addition, all-sky camera saturation on bright events made mass estimations disputable. It was therefore decided to select a small set of the most prominent ASGARD events, chosen by visual inspection of video images. Bright bolides with smaller apparent velocities and multiple camera observations were favoured. Zbyszek Krzeminski manually reduced the video data for each event, visually selecting images of lesser saturation and apparent lack of deceleration to arrive at the most precise initial contact state as possible.

Table of Events:

	20080805-035536	20081102-225458	20090316-013726	20090320-075820	20090331-053152	20090331-053152	20090428-044339	20090622-022124	20090825-011436
	2008 Aug 05	2008 Nov 02	2009 Mar 16	2009 Mar 20	2009 Mar 31	2009 Mar 31	2009 Apr 28	2009 Jun 22	2009 Aug 25
Epoch	03h56m41s TD	22h56m09s TD	01h38m32s TD	07h59m26s TD	05h32m58s TD	05h32m58s TD	04h44m44s TD	02h22m30s TD	01h14m36.s UT
lon (°)	-81.30441	-77.88091	-78.87712	-79.76814	-81.63827	-81.62455	-80.092	-81.16655	-78.43226
lat (°)	42.63616	44.9426	43.86249	46.08814	42.11676	42.13046	43.78197	43.54882	44.59966
h (km)	71.782	98.467	72.935	79.975	92.835	91.947	83.592	90.322	90.137
ra (°)	290.663	250.303	161.724	184.3	271.152	267.649	214.09	233.281	319.511
dec (°)	-28.659	16.591	11.843	5.309	43.344	43.112	12.554	19.075	16.085
v (km/s)	15.50	30.49	13.81	25.52	39.71	38.41	21.345	19.34	24.30
± lon (°)	0.0018	0.00154	0.0013	0.00128	0.0011	0.00148	0.002	0.00085	0.00207
± lat (°)	0.00058	0.00183	0.0023	0.01265	0.00305	0.00405	0.00368	0.00148	0.00262
± h (km)	0.061	0.146	0.156	0.635	0.383	0.508	0.209	0.088	0.176
± ra (°)	0.349	0.12	0.852	0.407	1.556	2.16	0.94	0.427	0.78
± dec (°)	0.084	0.067	0.581	3.092	0.139	0.238	1.062	0.541	0.553
± v (km/s)	0.20	0.30	0.99	0.60	1.07	0.68	0.60	0.21	0.30

Table 7-13. The Milig data for 10 selected ASGARD events. Events were chosen visually from event videos, selecting those multiple-station events with a combination of high brightness and low velocity.

Survey Effectiveness:

Event	CFHT (M=24.0,A=1.0)					SPACEWATCH (M=22.2,A=2.9)					CATALINA (M=19.7,A=9.0)					LINEAR (M=22.0,A=4.0)					Pan-STARRS (M=24.0,A=9.0)					LSST (M=25.0,A=9.6)				
	Alt	Drk	Pos	<M	Vis	Alt	Drk	Pos	<M	Vis	Alt	Drk	Pos	<M	Vis	Alt	Drk	Pos	<M	Vis	Alt	Drk	Pos	<M	Vis	Alt	Drk	Pos	<M	Vis
20080805-035536-Zmili-356-milig	14	16	12	-	12	8	16	8	-	8	8	16	8	-	8	7	16	7	-	7	14	16	12	-	12	28	22	22	-	22
20081102-225458-Zmili-567-first100pts	22	22	6	-	6	22	22	6	-	6	20	22	4	-	4	20	22	4	-	4	22	22	6	-	6	22	16	2	-	2
20090316-013726-man-zmili-2346-milig	20	20	20	-	20	20	18	18	-	18	20	20	20	-	20	21	20	20	-	20	20	20	20	-	20	21	18	18	-	18
20090320-075820-man-Zmili-456-milig	22	20	20	-	20	22	20	20	-	20	22	20	20	-	20	20	20	20	-	20	22	20	20	-	20	21	18	18	-	18
20090331-053152-cen-Zmili-456-milig	24	18	10	-	10	28	18	12	-	12	28	18	12	-	12	30	18	14	-	14	24	18	10	-	10	10	20	4	-	4
20090331-053152-cen-Zmili-4562-milig	25	18	10	-	10	28	18	12	-	12	28	18	12	-	12	28	18	12	-	12	26	18	10	-	10	10	20	4	-	4
20090331-053152-man-Zmili-564-milig	26	18	12	-	12	29	18	13	-	13	30	18	14	-	14	29	18	14	-	14	26	18	12	-	12	9	20	5	-	5
20090331-053152-man-Zmili-5642-milig	26	18	12	-	12	28	18	12	-	12	28	18	12	-	12	30	18	14	-	14	26	18	12	-	12	8	20	4	-	4
20090428-044339-max-Zmili-1246-milig	22	18	18	-	18	24	16	16	-	16	24	16	16	-	16	22	16	16	-	16	22	18	18	-	18	18	22	18	-	18
20090622-022124-man-Zmili-246-milig	20	18	4	-	4	20	14	2	-	2	20	14	2	-	2	20	14	2	-	2	20	18	4	-	4	22	24	8	-	8
20090825-011436-man-Zmili-256-milig	22	18	18	-	18	24	18	18	-	18	24	18	18	-	18	22	18	18	-	18	23	18	18	-	18	18	20	18	-	18
Mean:	22.1	18.5	12.9	-	12.9	23.0	17.8	12.5	-	12.5	22.9	18.0	12.5	-	12.5	22.6	18.0	12.8	-	12.8	22.3	18.5	12.9	-	12.9	17.0	20.0	11.0	-	11.0
	Vis x A: 12.9					Vis x A: 36.1					Vis x A: 112.9					Vis x A: 51.3					Vis x A: 116.2					Vis x A: 105.6				

Table 7-14. The survey effectiveness analysis for 10 major ASGARD events showing hours of visibility in the 48 hours prior to contact. Accurate mass, and therefore diameter and magnitude estimates are not available. A full explanation of effectiveness tables is provided in Section 6.6 and Table 6 1.

Survey	Alt	Drk	Pos	<M	Vis	Vis x A
CFHT (M=24.0,A=1.0)	22.1	18.5	12.9	-	12.9	12.9
SPACEWATCH (M=22.2,A=2.9)	23.0	17.8	12.5	-	12.5	36.1
CATALINA (M=19.7,A=9.0)	22.9	18.0	12.5	-	12.5	112.9
LINEAR (M=22.0,A=4.0)	22.6	18.0	12.8	-	12.8	51.3
Pan-STARRS (M=24.0,A=9.0)	22.3	18.5	12.9	-	12.9	116.2
LSST (M=25.0,A=9.6)	17.0	20.0	11.0	-	11.0	105.6

Table 7-15. A summarized effectiveness analysis corresponding to Table 7-14.

The survey effectiveness results are quite consistent across events, with the notable exception of event 20080805-035536. This event has substantially lesser visibility in northern surveys and higher visibility in the South American LSST survey. This is entirely consistent with the extreme southerly radiant of that object. As with the European Network events, the majority of events recorded in the northerly ASGAD system appear more detectable in northern hemisphere surveys that in the LSST. As before, the LSST limiting magnitude and field of view serve to compensate for the geographical bias.

8 CONCLUSIONS AND FUTURE WORK

8.1 Comments on work and results to date

As the project progressed, the realization developed that the chance of linking a fireball observation to a serendipitous PFM image is low. The modelling described in Chapter 3 shows that a sufficiently large event in any one given meteor detection network is, at the optimistic end, a yearly event. Conservatively, in the case of ASGARD, it is a decadal event. Survey effectiveness analyses show that the chances for telescope detection can be severely reduced by object or solar geometry, as well as the quickly reducing apparent magnitude of the PFM with time.   Finally, the chance of success is further reduced by the unmodelled but evidently small probability of a survey telescope being pointed at the correct field in relation to its overall sky coverage capability or preference. However, the possibility of success remains enticing. Of particular note is the level of genuine interest shown for this project by the many people with whom I have discussed the work. Those involved in sky surveys seem eager to make their data available and those analysing various fireball events are eager to provide and transform their data for use in this project.

A major accomplishment of this project was the confirmation of the Ceplecha (1987) orbit determination methods and the offering of an adjustment of that work to account for a shift in the PFM's longitude of the ascending node. In verbal conversations with Dr. Pavel Spurný and others, it has been stated that this validation of Ceplecha's methods has not been done before, even though they are widely used. There can now be an increased level of confidence in the orbits derived from those methods.

The image search technique described in Chapter 5 is a generic method which is independent of the source of the image and the target being searched. The technique is, therefore, easily adapted to any use where the image source

and target object are in motion. Whereas the original need of this project was to provide a flexible system that would support a variety of telescopic sky surveys, the approach can be easily extended to cover other image sources, such as spacecraft image databases, and amateur astrophoto collection.

8.2 Planned future publications

Four works have been immediately identified as output of this project: 1) a paper describing the full breadth of this project, 2) a brief paper to be submitted to the NASA Technical Report, containing submissions of many of the presenters at the Meteoroid 2010 conference, 3) a paper on the details of the image search algorithm as a general tool for image catalogue searching, and 4) a paper describing the required adjustment to the Ceplecha (1987) methods to properly account for a shift in the PFM's longitude of the ascending node.

8.3 Possible future work

8.3.1 Modelling

As discussed in section 3.3, the Bottke/Brown/Morbidelli modelling described in section 3.2 could be combined with the gravitation integration work in section 4.5 to drive an analysis of actual object detectability within a variety of meteor observation networks. This model could also be used to generate sky survey effective analyses similar to those reported on in Chapter 7.

The Bottke/Brown/Morbidelli modelling resulted in an approach angle distribution with unexpected ecliptical latitude asymmetry. This modelling result requires more investigation (see Appendix D).

8.3.2 Further analysis of Spurný (2010) Orbits

The comparison of the orbits from the numerical integration method to the unpublished Spurný (2010) collection of events yielded slightly larger deltas in orbital elements than did the comparison done with the Spurný (1997) events.

Once Spurný has published his final elements, the comparison of orbits should be repeated. If these small discrepancies still exist, a systematic cause for that discrepancy should be investigated.

8.3.3 Impact of Ascending Node Discrepancy

Section 4.6 describes a shift in instantaneous longitude of the ascending node Ω that occurs as an object approaches the Earth. This shift was identified as a result of the ClearSky gravitational integrations, but is not accounted for in the analytical methods of Ceplecha (1987). The incorrect assumption in the Ceplecha paper is that Ω is immediately derived from the Earth's solar longitude L_{SUN} at the time of contact. In that paper, all orbital elements except semimajor axis are derived from this L_{SUN} assumption and the resulting Ω. The impact on of these orbital elements as calculated by the Ceplecha method should be quantified.

8.3.4 Searching Additional Sky Surveys

This project concentrated on searching the CFHT image catalogue. An attempt was made to use the MPC Sky Coverage catalogue to search a number of other catalogues, but the lack of time information in this catalogue forced the need for an artificial day-long exposure assumption, which tended to confuse the image search algorithm. Direct access to the survey results is required and small plug-ins need to be written. At the time of writing, the Spacewatch program has provided a textual log file via private email conversation, giving sufficient information on every image from their wide-angle camera installed in 2003 (McMillan, 2010). McMillan has agreed to provide period updates by additional logs when requested periodically to do so. Automation of a bi-weekly update request and parsing of received emails is being considered. The Catalina Sky Survey has indicated that an image access interface can be set up (Beshore, 2010). Conversation continues as to the form of that interface. Dr. Robert Jedicke, in private conversation has confirmed that the process continues for my being designated an external scientist on the Pan-STARRS project (Jedicke,

2010). This should result in access to the Pan-STARRS survey. The format of that catalogue and interface has yet to be investigated.

8.3.5 Use of Additional Meteoroid Data Sources

This project has been concerned with major fireball events reported by ad hoc means: personal emails, papers, etc., and has looked at the general effective of Sky surveys to detect events from one fireball detection network, namely SOMN. Software has been developed that automates the trajectory integration and image search of an object given the manual keying of a contact state position and velocity vector. Further searches for ad hoc fireball meteoroids should continue as fireball events occur or as they are discovered in the literature. A thorough search for papers on bolide events could be undergone.

At the time of writing, I have received the state data on a superbolide event of July 23, 2008 over Tajikistan (Konovalova, Madiedo, & Trigo-Rodriguez, 2010), the data provided in a personal email from Konovalova (Konovalova, 2010). The conversation around this data highlights an ongoing issue around meteor contact state information. The data provided is not consistent across event. Reference frames may vary, for example: the equinox used (J2000, epoch of the date, J1950 for the Tajikistan event), the coordinate system (equatorial, geographic, etc.), and the Earth geoid model used. As well, the data form may be fundamentally different, for example: errors in contact longitude and latitude are not provided by Konovalova (2010), but instead, the errors in reference star positions and mid path object position are given. Ceplecha (1987) will need to be referenced to transform these errors to the needed initial contact position errors. A decision will then need to be made, as is often the case when a new form of data arrives, around performing a one-time transformation outside the existing code, or modifying the existing code to be more flexible on input forms supported.

Analysis of the effectiveness of sky surveys could be extended to other meteor detection networks, including the European Network and the Australian Network. This work would require the development of plug-ins that are able to convert event data from these networks to a standardized form used by the project software.

8.3.6 Enhancements to Software Performance

The existing software is very processor intensive, most noticeably in areas of object probability cloud integration. The software could benefit immensely by moving to a multithreaded model to take full advantage of multiple CPU systems and multiple core CPUs.

8.3.7 Enhancements to Automation

The ClearSky software was originally conceived and developed as a interactive program and is, therefore, very user-interface focused. The program does support limited function execution by command line arguments, as used in the automation of object database downloads and image catalogue downloads. However, the adding of new meteoroids and the invocation of image search or survey effectiveness analyses are manual operations. The command line argument interface should be extended to support the importing of new fireball observation data, and the invoking of an image search for such an object.

8.3.8 Stacking of All-Sky Images for Pre-atmospheric Imaging

In conversation with Dr. Peter Brown, we discussed the possibility of constructing an image of an object prior to atmospheric contact by stacking a number of pre-contact image frames captured by an all-sky camera. The back integration in time steps corresponding to the camera frame rate (30 frames/sec in the case of AGARD) required for this process has been completed. The

outstanding work is the conversion of this ephemeris back to the all-sky camera image coordinates to drive image alignment.

REFERENCES

Barentsen, G. (2006). Concept and presentation of a Unified Meteor DataBase. (L. Bastiaens, J. Verbert, J.-M. Wislez, & C. Verbeeck, Eds.) *Proceedings of the International Meteor Conference, Oostmalle, Belgium, 15-18 September, 2005* , 34-36.

Bate, R. R., Mueller, D. D., & White, J. E. (1971). *Fundamentals of Astrophysics.* New York: Dover Publications Inc.

Beatty, J. (1980). Computer Science 688. University of Waterloo, Ontario: Unpublished.

Beshore, E. (2010, June 02). Access to the CatalinaSky Survey Catalogue (Personal email).

Binzel, R. P., Bus, S. J., & Burbine, T. H. (1998). Size Dependence of Asteroid Spectral Properties: SMASS Results for Near-Earth and Main-Belt Asteroids. *29th Annual Lunar and Planetary Science Conference, March 16-20, 1998, Houston, TX* , abstract no. 1222.

Binzel, R. P., Harris, A. W., Bus, S. J., & Burbine, T. H. (2001). Spectral Properties of Near-Earth Objects: Palomar and IRTF Results for 48 Objects Including Spacecraft Targets (9969) Braille and (10302) 1989 ML. *Icarus , 151* (2), 139-149.

Binzel, R. P., Lupishko, D., di Martino, M., Whiteley, R. J., & Hahn, G. J. (2002). Physical Properties of Near-Earth Objects. (W. F. Bottke, A. Cellino, P. Paolicchi, & B. R. P., Eds.) *Asteroids III* , 255-271.

Bland, P. A., Spurný, P., Towner, M. C., Bevan, A. W., Singleton, A. T., Chesley, S. R., et al. (2009). A Eucrite Delivered from an Aten-type Orbit: The Last Link in the Chain from 4 Vesta to Earth. *40th Lunar and Planetary Science Conference, (Lunar and Planetary Science XL), held March 23-27, 2009 in The Woodlands, Texas, id.1664* .

Bottke, W. F., Jedicke, R., Morbidelli, A., Petit, J.-M., & Gladman, B. (2000). Understanding the Distribution of Near-Earth Asteroids. *Science , 288* (5474), 2190-2194.

Bottke, W. F., Morbidelli, A., Jedicke, R., Petit, J.-M., Levison, H. F., Michel, P., et al. (2002a). Debiased Orbital and Absolute Magnitude Distribution of the Near-Earth Objects. *Icarus , 156* (2), 399-433.

Bottke, W. F., Vokrouhlický, D., Rubincam, D. P., & Broz, M. (2002b). The effect of Yarkovsky thermal forces on the dynamical evolution of asteroids and meteoroids. (W. F. Bottke, A. Cellino, P. Paolicchi, & B. R. P., Eds.) *Asteroids III* .

Bowell, E., Hapke, B., Domingue, D., Lumme, K., Peltoniemi, J., & Harris, A. W. (1989). Application of photometric models to asteroids. *Asteroids II; Proceedings of the Conference, Tucson, AZ, Mar. 8-11, 1988 (A90-27001 10-91)* , 524-556.

Brown, H. (1960). The Density and Mass Distribution of Meteoritic Bodies in the Neighborhood of the Earth's Orbit. *Journal of Geophysical Research , 65*, 1679.

Brown, P. (2009, November 18). ASGARD Sky Coverage related to 2800 objects/year flux of objects of interest. (D. L. Clark, Interviewer)

Brown, P. (2007, April 2). Private email on conversions between heliocentic rectangular coordinates and Keplerian orbital elements.

Brown, P., Spalding, R. E., ReVelle, D. O., Tagliaferri, E., & Worden, S. P. (2002). The flux of small near-Earth objects colliding with the Earth. *Nature , 420*, 294-296.

Burbine, T. H., McCoy, T. J., Meibom, A., Gladman, B., & Keil, K. (2002). Meteoritic Parent Bodies: Their Number and Identification. (W. F. Bottke, A. Cellino, P. Paolicchi, & B. R. P., Eds.) *Asteroids III* , 653-667.

Ceplecha, Z. (1987). Geometric, dynamic, orbital and photometric data on meteoroids from photographic fireball networks. *Astronomical Institutes of Czechoslovakia, Bulletin , 38* (July 1987), 222-234.

Ceplecha, Z. (1992). Influx of interplanetary bodies onto earth. *Astronomy and Astrophysics , 263, no. 1-2*, 361-366.

Ceplecha, Z. (1994). Meteoroid Properties from Photographic Records of Meteors and Fireballs. (A. Milani, M. Di Martino, & A. Cellino, Eds.) *Asteroids, comets, meteors 1993: proceedings of the 160th International Astronomical Union, held in Belgirate, Italy, June 14-18, 1993 , 343*.

Ceplecha, Z., & Revelle, D. O. (2005, January). Fragmentation model of meteoroid motion, mass loss, and radiation in the atmosphere. *Meteoritics & Planetary Science , 40*, p. 35.

Ceplecha, Z., Borovička, J., Elford, W. G., Revelle, D. O., Hawkes, R. L., Porubčan, V., et al. (1998). Meteor Phenomena and Bodies. *Space Science Reviews , 84* (3/4), 327-471.

CFHT. (2009, 11 12). *Canada-France-Hawaii Telescope Legacy Survey*. Retrieved 11 14, 2009, from Canada-France-Hawaii Telescope: http://www.cfht.hawaii.edu/Science/CFHTLS/

Chapman, C. R., & Harris, A. W. (2009). Near-Earth Asteroid/Meteoroid Impacts: Prospects for Linking Telescopic Observations with Recovered Meteorites. *72nd Annual Meeting of the Meteoritical Society, held July 13-18, 2009 in Nancy, France. Published in Meteoritics and Planetary Science Supplement* , p. 5041.

Chapman, C. R., Harris, A. W., & Binzel, R. (1994). Physical Properties of Near-earth Asteroids: Implications for the Hazard Issue. Hazards due to comets and asteroids, Space Science Series, Tucson, AZ. (T. Gehrels, Matthews.M.S., & A. Schumann, Eds.) 537.

Chesley, S. R., & Spahr, T. B. (2004). Earth impactors: orbital characteristics and warning times. Mitigation of hazardous comets and asteroids. (M. Belton, T. H. Morgan, N. Samarasinha, & D. K. Yeomans, Eds.) 22.

Durda, D. D., Greenberg, R., & Jedicke, R. (1998). Collisional models and scaling laws: A new interpretation of the shape of the main-belt asteroid size distribution. *Icarus , 135*, 431–440.

Edwards, W. N., Brown, P. G., Weryk, R. J., & Revelle, D. O. (2008). Infrasonic Observations of Meteoroids: Preliminary Results from a Coordinated Optical-radar-infrasound Observing Campaign. *Earth, Moon, and Planets , 102* (1-4), 221-229.

Erikson, A., Mottola, S., Lagerros, J. S., Lindgren, M., Piironen, J., Oja, T., et al. (2000). The Near-Earth Objects Follow-up Program III. 32 Lightcurves for 12 Objects from 1992 and 1995. *Icarus , 147* (2), 487-497.

Everhart, E. (1985). An efficient integrator that uses Gauss-Radau spacings. (A. Carus, & G. B. Valsecchi, Eds.) *Dynamics of Comets: Their Origin and Evolution, Proceedings of IAU Colloq. 83, held in Rome, Italy, June 11-15, 1984 , 115*, 185.

Farinella P., F. C. (1994). Asteroids falling into the Sun. *Nature , 371*, 314–317.

Gilbert, A. M., & Wiegert, P. A. (2009, June). Searching for main-belt comets using the Canada-France-Hawaii Telescope Legacy Survey. *Icarus , 201* (2), pp. 714-718.

Gladman, B., Migliorini, F., Morbidelli, A., Zappalà, V., Michel, P., Cellino, A., et al. (1997). Dynamical lifetimes of objects injected into asteroid belt resonances. *Science , 277*, 197–201.

Greenberg, R., & Nolan, M. (1989). Delivery of asteroids and meteorites to the inner solar system. (R. P. Binzel, T. Gehrels, & M. S. Matthews, Eds.) *Asteroids II* .

Hahn, G. (2009, Oct 28). *The Near-Earth Asteroids Data Base*. Retrieved Oct 30, 2009, from Institute of Planetary Research of the German Aerospace Center (DLR): http://earn.dlr.de/nea/

Halliday, I., Griffin, A. A., & Blackwell, A. T. (1996). Detailed data for 259 fireballs from the Canadian camera network and inferences concerning the influx of large meteoroids. *Meteoritics and Planetary Science , 31*, 185-217.

Halliday, I., Griffin, A. A., & Blackwell, A. T. (1984). The frequency of meteorite falls on the earth. *Science , 223* (March 30, 1984), 1405-1407.

Hammergren, M. (1998). The Composition of Near-Earth Objects. *Thesis (PHD). UNIVERSITY OF WASHINGTON , Source DAI-B 59/09* , 4872,110 pages.

Harris, A. W. (2002). A New Estimate of the Population of Small NEAs. American Astronomical Society, DPS Meeting #34, #02.02. *Bulletin of the American Astronomical Society , 34*, 835.

Harris, A. W. (1998). A Thermal Model for Near-Earth Asteroids. *Icarus , 131* (2), 291-301.

Harris, A. W., & Davies, J. K. (1999). Physical Characteristics of Near-Earth Asteroids from Thermal Infrared Spectrophotometry. *Icarus , 142*, 464-475.

Hawkins, G. S. (1960). Asteroidal fragments. *Astronomical Journal , 65*, 318.

Hicks, M. D., Buratti, B. J., Newburn, R. L., & Rabinowitz, D. L. (2000). Physical Observations of 1996 PW and 1997 SE5: Extinct Comets or D-Type Asteroids? *Icarus , 354-359*, 354-359.

Hicks, M., Fink, U., & Grundy, W. (1998). The Unusual Spectra of 15 Near-Earth Asteroids and Extinct Comet Candidates. *Icarus , 133* (1), 69-78.

Hildebrand, A. R., Milley, E. P., Brown, P. G., McCausland, P. J., Edwards, W., Beech, M., et al. (2009). Characteristics of a Bright Fireball and Meteorite Fall at Buzzard Coulee, Saskatchewan, Canada, November 20, 2008. *40th Lunar and Planetary Science Conference, (Lunar and Planetary Science XL), held March 23-27, 2009 in The Woodlands, Texas, id.2505* .

Hughes, D. W. (1981). Meteorite falls and finds - Some statistics. *Meteoritics , 16, Sept.30, 1981*, 269-281.

Ivanov, B. A., Neukum, G., & Wagner, R. (1999). Impact Craters, NEA, and Main Belt Asteroids: Size-Frequency Distribution. *30th Annual Lunar and Planetary Science Conference, March 15-29, 1999, Houston, TX, abstract no. 1583* .

Ivanov, B. A., Neukum, G., & Wagner, R. (2001). Size-frequency distributions of planetary impact craters and asteroids. (M. Y. Marov, & H. Rickman, Eds.) *Collisional processes in the solar system* , 1-34.

Ivezić, Ž., Tabachnik, S., Rafikov, R., Lupton, R. H., Quinn, T., Hammergren, M., et al. (2001). Solar System Objects Observed in the Sloan Digital Sky Survey Commissioning Data. *The Astronomical Journal , 122* (5), 2749-2784.

Jedicke, R. (2010, May 27). Access to the PanSTARRS Image Catalogue (Private conversation). Breckenridge, Colorado.

Jedicke, R. (1996). Detection of Near Earth Asteroids Based Upon Their Rates of Motion. *Astronomical Journal , 111*, 970.

Jedicke, R., & Metcalfe, T. S. (1998). The Orbital and Absolute Magnitude Distributions of Main Belt Asteroids. *Icarus , 131* (2), 245-260.

Jedicke, R., Larsen, J., & Spahr, T. (2002). Observational Selection Effects in Asteroid Surveys. (W. F. Bottke, A. Cellino, P. Paolicchi, & R. P. Binzel, Eds.) *Asteroids III,* , 71-87.

Jenniskens, P., Shaddad, M. H., Numan, D., Elsir, S., Kudoda, A. M., Zolensky, M. E., et al. (2009). The impact and recovery of asteroid 2008 TC3. *Nature , 458* (7237), 485-488.

Kim, S., Lee, H. M., Nakagawa, T., & Hasegawa, S. (2003). Thermal Models and Far Infrared Emission of Asteroid. *Journal of the Korean Astronomical Society , 36* (1), 21-31.

Konovalova, N. (2010, June 14). Position and velocity vector data for the superbolide of July 23, 2008 (Personal email).

Konovalova, N., Madiedo, J. M., & Trigo-Rodriguez, J. (2010). The trajectory, orbit and preliminary fall data of the superbolide of July 23, 2008 (Abstract). *Abstract Book for Meteoroids 2010* , 135.

Koschny, D., Mc Auliffe, J., & Barentsen, G. (2008). The IMO Virtual Meteor Observatory (VMO): Architectural Design. *Earth, Moon, and Planets* , *102* (1-4), 247-252.

Kovshun, I. N. (1977). A New Meteoroid Mass Scale and Meteor Emissions at Maximum Brightness. *Solar System Research* , *11*, 3.

Lebofsky, L., & Spencer, J. (1989). Radiometry and a thermal modeling of asteroids. *Asteroids II; Proceedings of the Conference, Tucson, AZ, Mar. 8-11, 1988* , 128-147.

Lupishko, D. F., & di Martino, M. (1998). Physical properties of near-Earth asteroids. *Planetary and Space Science* , *46*, 47-74.

Luu, J. X., & Jewitt, D. C. (1989). On the relative number of C types and S types among near-Earth asteroids. *Astron. J.* , *98*, 1905–1911.

McCausland, P. J., Brown, P. G., Hildebrand, A. R., Flemming, R. L., Barker, I., Moser, D. E., et al. (2010). Fall of the Grimsby H5 Chondrite. *41st Lunar and Planetary Science Conference, held March 1-5, 2010 in The Woodlands, Texas.* , p. 2716.

McCrosky, R. E., & Ceplecha, Z. (1969). Photographic Networks for Fireballs. Meteorite Research, Proceedings of a Symposium held in Vienna, Austria, August 7-13, 1968. (P. M. Millman, Ed.) *Astrophysics and Space Science Library* , *12*, 600.

McKinley, D. W. (1961). Meteor science and engineering.

McMillan, R. (2010, June 01). The Spacewatch image catalogue textual log (Personal email).

Meeus, J. (1991). *Astronomical Algorithms.* Richmond, Virginia: Willman-Bell, Inc.

Millard, H. T. (1963). The Rate of Arrival of Meteorites at the Surface of the Earth. *Journal of Geophysical Research* , *68*, 4297.

Morbidelli, A., & Gladman, B. (1998). Orbital and temporal distributions of meteorites originating in the asteroid belt. *Meteoritics & Planet. Sci.* , *33*, 999–1016.

Morbidelli, A., Bottke, W. F., Froeschlé, C., & Michel, P. (2002b). Origin and Evolution of Near-Earth Objects. (W. F. Bottke, A. Cellino, P. Paolicchi, & B. R. P., Eds.) *Asteroids III* , 409-422.

Morbidelli, A., Jedicke, R., Bottke, W. F., Michel, P., & Tedesco, E. F. (2002a). From Magnitudes to Diameters: The Albedo Distribution of Near Earth Objects and the Earth Collision Hazard. *Icarus* , *158* (2), 329-342.

Morrison, D. (1992). The Spaceguard Survey - Protecting the earth from cosmic impacts. *Mercury* , *21* (no. 3, May-June 1992), 103-106,110.

Morrison, D., Chapman, C. R., & Slovic, P. (1994). The Impact Hazard. Hazards due to comets and asteroids, Space Science Series. (T. Gehrels, M. S. Matthews, & S. A., Eds.) 59-91.

Muinonen, K. (1994). Coherent Backscattering by Solar System Dust Particles. (A. Milani, M. Di Martino, & A. Cellino, Eds.) *Asteroids, comets, meteors 1993: proceedings of the 160th International Astronomical Union, held in Belgirate, Italy, June 14-18, 1993* , 271.

Muinonen, K., Piironen, J., Shkuratov, Y. G., Ovcharenko, A., & Clark, B. E. (2002). Asteroid Photometric and Polarimetric Phase Effects. (W. F. Bottke, A. Cellino, P. Paolicchi, & B. R. P., Eds.) 123-138.

Neukum, G. (1983). Variations in Crater Size Distributions: Implications for the Meteoroid Complex. *Meteoritics* , *18*, 362.

Neukum, G., & Ivanov, B. (1994). The Inner Solar System Impact Record: Lunar, Terrestrial-Planet, and Asteroid Size-Frequency Data Comparison. *Abstracts of the 25th Lunar and Planetary Science Conference, held in Houston, TX, 14-18 March 1994* , 991.

Olmstead, & Leies. (1978). Refered to in Revelle (2001a) without a bioblography entry. Unable to locate this work.

Öpik, E. (1933). Atomic Collisions and Radiation of Meteors. *Acta Commentationes Univ. Tartu A26 , 2*, 1-39.

Öpik, E. J. (1951). Collision probability with the planets and the distribution of planetary matter. *Proc. R. Irish Acad. Sect. A , 54*, 165-199.

Opik, E. J. (1958). *Physics of meteor flight in the atmosphere.* New York: Interscience Publishers.

Pecina, P., & Koten, P. (2009). On the theory of light curves of video-meteors. *Astronomy and Astrophysics , 499* (1,2009), 313-320.

Pravec, P., Hergenrother, C., Whiteley, R., Šarounová, L., Kušnirák, P., & Wolf, M. (2000). Fast Rotating Asteroids 1999 TY2, 1999 SF10, and 1998 WB2. *Icarus , 147* (2), 477-486.

Rabinowitz, D. L. (1998). NOTE: Size and Orbit Dependent Trends in the Reflectance Colors of Earth-Approaching Asteroids. *Icarus , 134* (2), 342-346.

Rabinowitz, D. L. (1994). The size and shape of the near-Earth asteroid belt. *Icarus , 111* (2), 364-377.

Rabinowitz, D. L. (1993). The size distribution of the earth-approaching asteroids. *Astrophysical Journal, Part 1 , 407* (1), 412-427.

Rabinowitz, D. L., Bowell, E., Shoemaker, E. M., & Muinonen, K. (1994). Hazards due to comets and asteroids, Space Science Series. (T. Gehrels, M. S. Matthews, & A. Schumann, Eds.) 285.

Rabinowitz, D., Helin, E., Lawrence, K., & Pravdo, S. (2000). A reduced estimate of the number of kilometre-sized near-Earth asteroids. *Nature , 403* (6766), 165-166.

Revelle, D. O. (1980). A predictive macroscopic integral radiation efficiency model. *Journal of Geophysical Research , 85* (Apr. 10, 1980), 1803-1808.

Revelle, D. O. (2001b). Bolide fragmentation processes: single-body modeling versus the catastrophic fragmentation limit. In: Proceedings of the Meteoroids 2001 Conference, 6 - 10 August 2001, Kiruna, Sweden. (B. Warmbein, Ed.) 491-498.

Revelle, D. O. (2001a). Global infrasonic monitoring of large bolides. In: Proceedings of the Meteoroids 2001 Conference, 6 - 10 August 2001, Kiruna, Sweden. (B. Warmbein, Ed.) 483 - 489.

Schmidt, R. M., & Housen, K. R. (1987). Some recent advances in the scaling of impact and explosion cratering. *Int. J. Impact Eng. , 5*, 543-560.

Shkuratov, Y. G., Muinonen, K., Bowell, E., Lumme, K., Peltoniemi, J. I., Kreslavsky, M. A., et al. (1994). A critical review of theoretical models of negatively polarized light scattered by atmosphereless solar system bodies. *Earth, Moon, and Planets , 65* (3), 201-246.

Shoemaker, E. M. (1983). Asteroid and comet bombardment of the earth. *Annual review of earth and planetary sciences , 11*, 461-494.

Shoemaker, E. M., & Wolfe, R. F. (1982). Cratering time scales for the Galilean satellites. *Satellites of Jupiter* , 277 - 339.

Shoemaker, E. M., Shoemaker, C. S., & Wolfe, R. F. (1988). Asteroid and Comet Flux in the Neighborhood of the Earth. Abstracts Presented to the Topical Conference on Global Catastrophes in Earth History: An Interdisciplinary Conference on Impacts, Volcanism, and Mass Mortality. Held October 20-23, 1988, in Snowbi.

Shoemaker, E. M., Weissman, P. R., & Shoemaker, C. S. (1994). Hazards due to comets and asteroids, Space Science Series. (T. Gehrels, M. S. Matthews, & A. Schumann, Eds.) 313.

Shoemaker, E. M., Williams, J. G., Helin, E. F., & Wolfe, R. F. (1979). Earth-crossing asteroids - Orbital classes, collision rates with earth, and origin. *Asteroids* , 253-282.

SOMN. (2009, October 23). *SOMN Fireball event of September 25, 2009*. Retrieved November 1, 2009, from Meteor Physics, University of Western Ontario: http://aquarid.physics.uwo.ca/research/fireball/events/25sept2009/

Spurný, P. (2009, February 27). *State vector for the Bunburra Rockhole meteor (Personal email)* .

Spurný, P. (1997). Exceptional fireballs photographed in central Europe during the period 1993-1996. *Planetary and Space Science , 45*, 541-555.

Spurný, P. (2010, May 13). Recent European Network event tables (Personal email).

Stokes, G. H., Evans, J. B., & Larson, S. M. (2002). Near-Earth Asteroid Search Programs. (W. F. Bottke, A. Cellino, P. Paolicchi, & R. P. Binzel, Eds.) *Asteroids III* , 45-54.

Stuart, J. S. (2001). A near-Earth asteroid population estimate from the LINEAR survey. *Science , 294*, 1691-1693.

Tagliaferri, E., Spalding, R., Jacobs, C., Worden, S. P., & Erlich, A. (1994). Detection of Meteoroid Impacts by Optical Sensors in Earth Orbit. Hazards due to comets and asteroids, Space Science Series. (T. Gehrels, M. S. Matthews, & A. Schumann, Eds.) 199.

Tedesco, E. F., & Gradie, J. C. (2002). Albedos and diameters for 350 asteroids from the IRTF 10 and 20 μm radiometry survey. *Astron. J. , Referenced as to be submitted in Morbidelli et all (2002a) but not found.*

USNO. (2010). *Table of TAI-UTC Differences.* Retrieved Mar 13, 2010, from US Naval Observatory: ftp://maia.usno.navy.mil/ser7/tai-utc.dat

Weissman, P. R. (1982). Cometary impacts on the terrestrial planets. Abstracts of Papers presented to the conference on Planetary Volatiles, held in Alexandria, Minnesota, October 9-12, 1982. Sponsored by the Lunar and Planetary Institute, NASA, and the National Science Foundati. 109.

Weissman, P. R. (1991). The cometary impactor flux at the Earth. In Global Catastrophes in Earth History. (V. L. Sharpton, & P. D. Ward, Eds.) *Geological Soc. of America Special Paper 247* , 171—180.

Werner, S. C., Harris, A. W., Neukum, G., & Ivanov, B. A. (2002). NOTE: The Near-Earth Asteroid Size-Frequency Distribution: A Snapshot of the Lunar Impactor Size-Frequency Distribution. *Icarus , 156* (1), 287-290.

Weryk, R. (2009, 03 10). *ASGARD Introduction*. Retrieved 11 14, 2009, from ASGARD: http://aquarid.physics.uwo.ca/~weryk/asgard/

Weryk, R. J., Brown, P. G., Domokos, A., Edwards, W. N., Krzeminski, Z., Nudds, S. H., et al. (2008). The Southern Ontario All-sky Meteor Camera Network. *Earth, Moon, and Planets , 1002* (1-4), 241-246 .

Wetherill, G. (1985). Asteroidal sources of ordinary chondrites. *Meteoritics , 20*, 1–22.

Wetherill, G. W. (1967). Collisions in the Asteroid Belt. *Journal of Geophysical Research , 72*, 2429.

Wetherill, G. W. (1989). Cratering of the terrestrial planets by Apollo objects. *Meteoritics , 24* (March 1989), 15-22.

Wetherill, G. W., & Shoemaker, E. M. (1982). Collisions of astronomically observable bodies with the Earth. In Geological Implications of Impacts of Large Asteroids and Comets with the Earth, eds. L. T. Silver and P. H. Schultz, Geological Soc. of America Special Paper 190. 1-44.

Whipple, F. L. (1942). Meteors and the Earth's Upper Atmosphere. *Reviews of Modern Physics , 14* (2-3), 139.

Whiteley, R. J. (2001). A compositional and dynamical survey of the near-Earth asteroids. *PhD. thesis, University of Hawaii* , 202 pages.

Whiteley, R. J., & Tholen, D. J. (1999). The UH Near-Earth Asteroid Composition Survey: an Update. *American Astronomical Society , DPS meeting #31*, #11.02.

Wiegert, P., Balam, D., Moss, A., Veillet, C., Connors, M., & Shelton, I. (2007). Evidence for a Color Dependence in the Size Distribution of Main-Belt Asteroids. *The Astronomical Journal , 133* (4), 1609-1614.

Wisniewski, W. Z., Michalowski, T. M., Harris, A. W., & McMillan, R. S. (1997). Photometric Observations of 125 Asteroids. *Icarus , 126* (2), 395-449.

Appendix A – Dynamical Time and UT

Observations of meteor contacts are typically expressed in Universal Time (UT). This time scale is based on the rotation of the Earth, which varies, and generally is slowing. As described in Meeus (1991), Dynamical Time (TD) is a uniform time scale extending from the older Ephemeris Time scale (ET) which was based on planetary motion. There are two variations of TD, Barycentric Dynamical Time (BDT) and Terrestrial Dynamic Time (TDT) which vary due to relativistic effect, and differ by at most .0017 seconds. TD was replaced in 2001 by the equivalent TT (Terrestrial Time). TD is required for accurate positioning of the planets, accurate calculation of nutation, and calculation of the angle of the ecliptic. TT is the time scale utilized by the DE405/DE406 ephemerides. The method of calculation of the adjustment from UT to TD or TT ($\Delta t = \mathrm{TD} - \mathrm{UT}$) varies depending on the epoch in question. For completeness I document the methods of Meeus (1991) for the period before 1620 and the period 1620-1971. For 1972 and beyond, the time period of interest for this project, we use the table USNO (2010) provided by the U.S. Naval Observatory.

For epochs prior to 1620, where JD is the Julian day, Δt may be estimated as follows:

$$\Delta t = -15 + \frac{(JD - 2382148)^2}{41048480} \tag{64}$$

Meeus (1991) documents an uncertainty for this formula of as much as two hours at 4000 B.C.

For epochs from 1620 to 1971, we use the following table derived from Meeus (1991). The table lists values of $\Delta t \times 10$ at the beginning of each year in 2 year increments. One can do a linear interpolation for dates within each date range, although the actual change in Δt is not linear.

Year	0	2	4	6	8	Year	0	2	4	6	8
162(0..8)	1240	1150	1060	980	910	180(0..8)	137	131	127	125	125
163(0..8)	850	790	740	700	650	181(0..8)	125	125	125	125	123
164(0..8)	620	580	550	530	500	182(0..8)	120	114	106	96	86
165(0..8)	480	460	440	420	400	183(0..8)	75	66	60	57	56
166(0..8)	370	350	330	310	280	184(0..8)	57	59	62	65	68
167(0..8)	260	240	220	200	180	185(0..8)	71	73	75	77	78
168(0..8)	160	140	130	120	110	186(0..8)	79	75	64	54	29
169(0..8)	100	90	90	90	90	187(0..8)	16	-10	-27	-36	-47
170(0..8)	90	90	90	90	100	188(0..8)	-54	-52	-55	-56	-58
171(0..8)	100	100	100	100	110	189(0..8)	-59	-62	-64	-61	-47
172(0..8)	110	110	110	110	110	190(0..8)	-27	0	26	54	77
173(0..8)	110	110	120	120	120	191(0..8)	105	134	160	182	202
174(0..8)	120	120	130	130	130	192(0..8)	212	224	235	239	243
175(0..8)	130	140	140	140	150	193(0..8)	240	239	239	237	240
176(0..8)	150	150	150	160	160	194(0..8)	243	253	262	273	282
177(0..8)	160	160	160	170	170	195(0..8)	291	300	307	314	322
178(0..8)	170	170	170	170	170	196(0..8)	331	340	350	365	383
179(0..8)	170	160	160	150	140	197(0..8)	402				

Table A-1. Values for Δt = (TD-UT)×10 for the period 1620 to 1971 from Meeus.

For epochs in 1972 and later, we use a table of adjustments made available online by the US Naval Observatory (USNO, 2010). Table A-2 lists date dependent adjustments between UT and TAI (International atomic time), where the difference between TT and TAI is a constant 32.184 seconds.

```
1972 JAN  1 =JD 2441317.5  TAI-UTC=  10.0      1985 JUL  1 =JD 2446247.5  TAI-UTC=  23.0
1972 JUL  1 =JD 2441499.5  TAI-UTC=  11.0      1988 JAN  1 =JD 2447161.5  TAI-UTC=  24.0
1973 JAN  1 =JD 2441683.5  TAI-UTC=  12.0      1990 JAN  1 =JD 2447892.5  TAI-UTC=  25.0
1974 JAN  1 =JD 2442048.5  TAI-UTC=  13.0      1991 JAN  1 =JD 2448257.5  TAI-UTC=  26.0
1975 JAN  1 =JD 2442413.5  TAI-UTC=  14.0      1992 JUL  1 =JD 2448804.5  TAI-UTC=  27.0
1976 JAN  1 =JD 2442778.5  TAI-UTC=  15.0      1993 JUL  1 =JD 2449169.5  TAI-UTC=  28.0
1977 JAN  1 =JD 2443144.5  TAI-UTC=  16.0      1994 JUL  1 =JD 2449534.5  TAI-UTC=  29.0
1978 JAN  1 =JD 2443509.5  TAI-UTC=  17.0      1996 JAN  1 =JD 2450083.5  TAI-UTC=  30.0
1979 JAN  1 =JD 2443874.5  TAI-UTC=  18.0      1997 JUL  1 =JD 2450630.5  TAI-UTC=  31.0
1980 JAN  1 =JD 2444239.5  TAI-UTC=  19.0      1999 JAN  1 =JD 2451179.5  TAI-UTC=  32.0
1981 JUL  1 =JD 2444786.5  TAI-UTC=  20.0      2006 JAN  1 =JD 2453736.5  TAI-UTC=  33.0
1982 JUL  1 =JD 2445151.5  TAI-UTC=  21.0      2009 JAN  1 =JD 2454832.5  TAI-UTC=  34.0
1983 JUL  1 =JD 2445516.5  TAI-UTC=  22.0
```

Table A-2. Data of interest from USNO. The table lists the delta between TAI and UT and the times of adjustment. TAI differs from TD and TT by 32.184 seconds. Δt = TD-UT is calculated as Δt = TAI – UT + 32.184.

Appendix B – Nutation in Longitude and Obliquity

Nutation is the periodic oscillation of the Earth's instantaneous rotational axis around it's mean pole, which in turn precesses around the pole of the ecliptic. Nutation is expressed in two components, $\Delta\Psi$ is the nutation in longitude, and $\Delta\varepsilon$ is the nutation in obliquity. Nutation is primarily due to the motion of the Moon. The calculation of $\Delta\Psi$ and $\Delta\varepsilon$ is taken directly from Meeus (1991) as follows. Calculate the expressions:

the number of centuries from the epoch J2000 to the desired Julian date expressed in dynamical time (*JD*):

$$T = \frac{JD - 2451545}{36525} \tag{65}$$

the mean elongation of the Moon from the Sun:

$$D = 297.85036 + 445267.111480T - 0.0019142T^2 + T^3/189474.0 \tag{66}$$

the mean anomaly of the Earth with respect to the Sun:

$$M = 357.52772 + 35999.050340T - 0.0001603T^2 - T^3/300000.0 \tag{67}$$

the mean anomaly of the Moon:

$$M' = 134.96298 + 477198.867398T + 0.0086972T^2 + T^3/56250.0 \tag{68}$$

the argument of latitude of the Moon:

$$F = 93.27191 + 483202.017538T - 0.0036825T^2 + T^3/327270.0 \tag{69}$$

and the longitude of the ascending node of the Moon:

$$\Omega = 125.04452 - 1934.136261T - 0.0020708T^2 + T^3/450000 \tag{70}$$

Using the table of periodic term multipliers and coefficients listed in Table B-1, calculate an argument for each periodic term:

$$a_i = D \times C_{D_i} + M \times C_{M_i} + M' \times C_{M'_i} + F \times C_{F_i} + \Omega \times C_{\Omega_i} \qquad (71)$$

The components of nutation are then calculated as the sum of the periodic terms:

$$\Delta\psi = \sum_{i=1}^{63}(C_{sin_i} + C_{sinT_i} \times {}^T/_{10}) \sin a_i \qquad (72)$$

$$\Delta\epsilon = \sum_{i=1}^{63}(C_{cos_i} + C_{cosT_i} \times {}^T/_{10}) \cos a_i \qquad (73)$$

Where $\Delta\Psi$ and $\Delta\varepsilon$ are expressed in units of 0".0001.

Term	C_D	C_M	$C_{M'}$	C_F	C_Ω	C_{cos}	C_{cosT}	C_{sin}	C_{sinT}	Term	C_D	C_M	$C_{M'}$	C_F	C_Ω	C_{cos}	C_{cosT}	C_{sin}	C_{sinT}
1	0	0	0	0	1	-171996	-1742	92025	89	33	0	-1	0	0	1	-12	0	6	0
2	-2	0	0	2	2	-13187	-16	5736	-31	34	0	0	2	-2	0	11	0	0	0
3	0	0	0	2	2	-2274	-2	977	-5	35	2	0	-1	2	1	-10	0	5	0
4	0	0	0	0	2	2062	2	-895	5	36	2	0	1	2	2	-8	0	3	0
5	0	1	0	0	0	1426	-34	54	-1	37	0	1	0	2	2	7	0	-3	0
6	0	0	1	0	0	712	1	-7	0	38	-2	1	1	0	0	-7	0	0	0
7	-2	1	0	2	2	-517	12	224	-6	39	0	-1	0	2	2	-7	0	3	0
8	0	0	0	2	1	-386	-4	200	0	40	2	0	0	2	1	-7	0	3	0
9	0	0	1	2	2	-301	0	129	-1	41	2	0	1	0	0	6	0	0	0
10	-2	-1	0	2	2	217	-5	-95	3	42	-2	0	2	2	2	6	0	-3	0
11	-2	0	1	0	0	-158	0	0	0	43	-2	0	1	2	1	6	0	-3	0
12	-2	0	0	2	1	129	1	-70	0	44	2	0	-2	0	1	-6	0	3	0
13	0	0	-1	2	2	123	0	-53	0	45	2	0	0	0	1	-6	0	3	0
14	2	0	0	0	0	63	0	0	0	46	0	-1	1	0	0	5	0	0	0
15	0	0	1	0	1	63	1	-33	0	47	-2	-1	0	2	1	-5	0	3	0
16	2	0	-1	2	2	-59	0	26	0	48	-2	0	0	0	1	-5	0	3	0
17	0	0	-1	0	1	-58	-1	32	0	49	0	0	2	2	1	-5	0	3	0
18	0	0	1	2	1	-51	0	27	0	50	-2	0	2	0	1	4	0	0	0
19	-2	0	2	0	0	48	0	0	0	51	-2	1	0	2	1	4	0	0	0
20	0	0	-2	2	1	46	0	-24	0	52	0	0	1	-2	0	4	0	0	0
21	2	0	0	2	2	-38	0	16	0	53	-1	0	1	0	0	-4	0	0	0
22	0	0	2	2	2	-31	0	13	0	54	-2	1	0	0	0	-4	0	0	0
23	0	0	2	0	0	29	0	0	0	55	1	0	0	0	0	-4	0	0	0
24	-2	0	1	2	2	29	0	-12	0	56	0	0	1	2	0	3	0	0	0
25	0	0	0	2	0	26	0	0	0	57	0	0	-2	2	2	-3	0	0	0
26	-2	0	0	2	0	-22	0	0	0	58	-1	-1	1	0	0	-3	0	0	0
27	0	0	-1	2	1	21	0	-10	0	59	0	1	1	0	0	-3	0	0	0
28	0	0	0	0	0	17	-1	0	0	60	0	-1	1	2	2	-3	0	0	0
29	2	0	-1	0	1	16	0	-8	0	61	2	-1	-1	2	2	-3	0	0	0
30	-2	2	0	2	2	-16	1	7	0	62	0	0	3	2	2	-3	0	0	0
31	0	1	0	0	1	-15	0	9	0	63	2	-1	0	2	2	-3	0	0	0
32	-2	0	1	0	1	-13	0	7	0										

Table B-1. Argument multiples and coefficients used in calculating the periodic terms of the nutation components ΔΨ and Δε. See the text for the usage of these values.
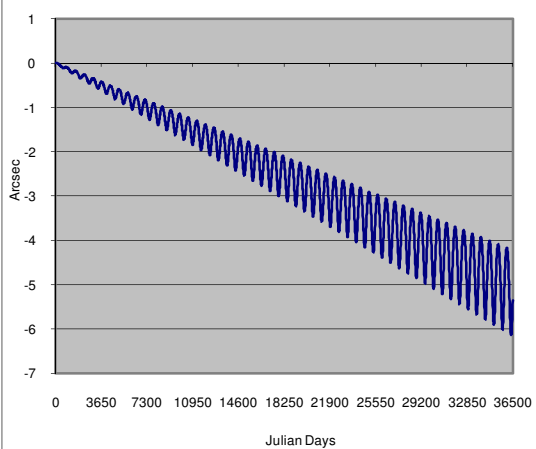
Appendix C – RADAU-15 & DE405/DE406 Comparisons

The following figures detail the differences in solar longitude and solar distance of major solar system objects over 100 years as calculated by the RADAU-15 integrator and as provided by the NASA JPL DE405/DE406 ephemeris.
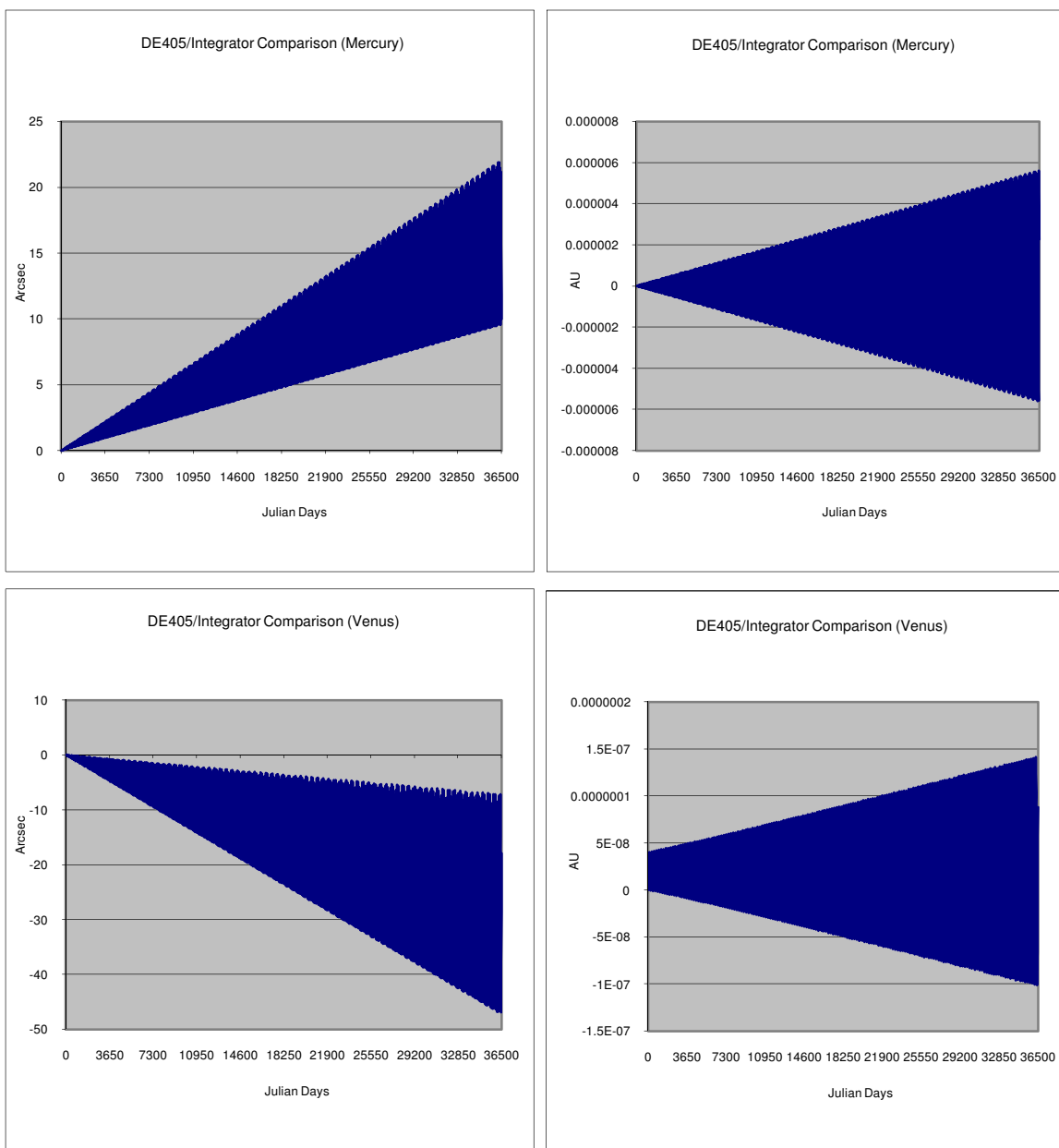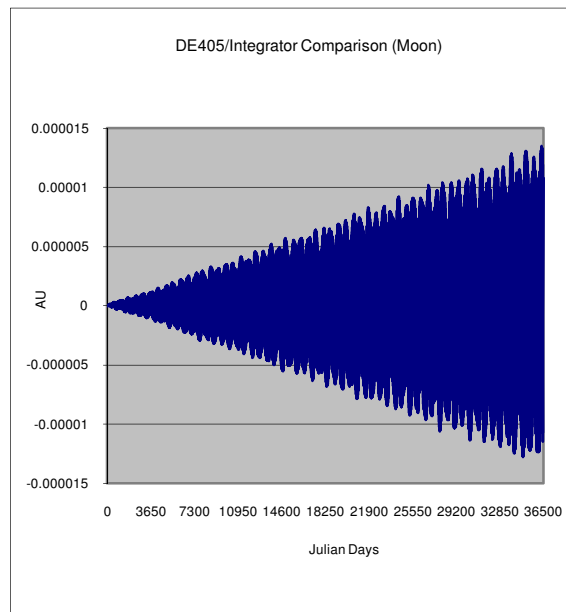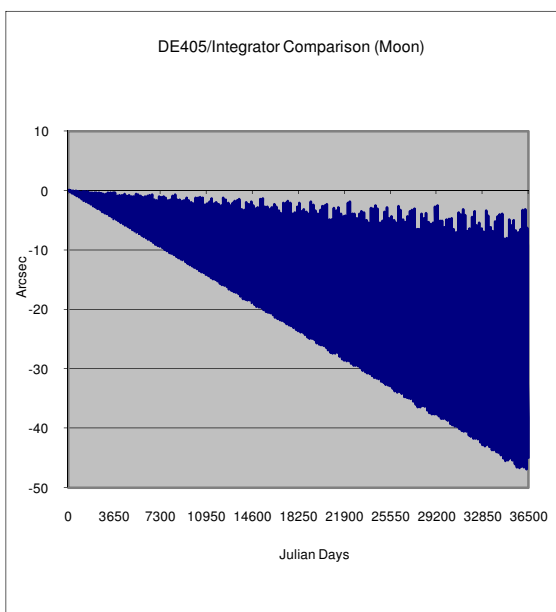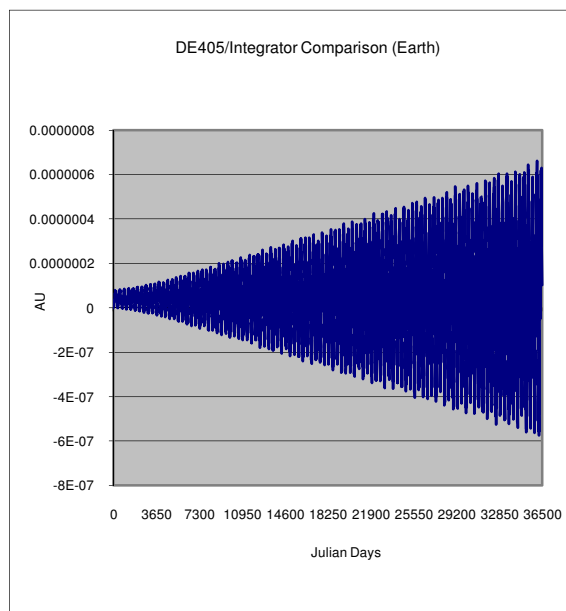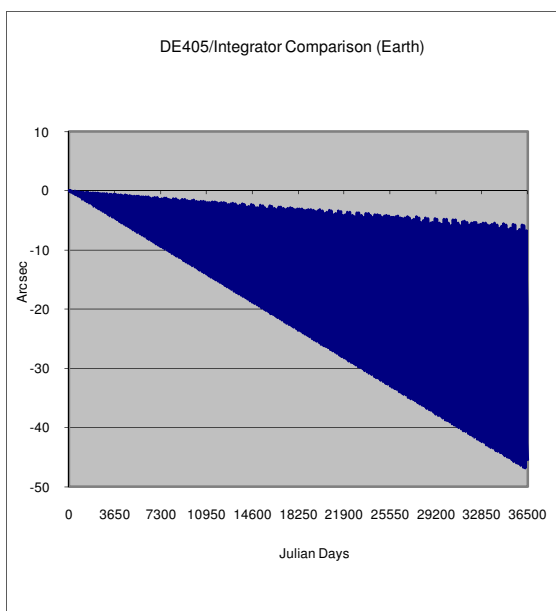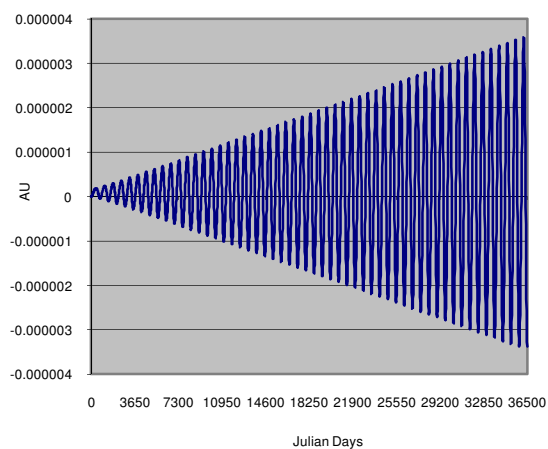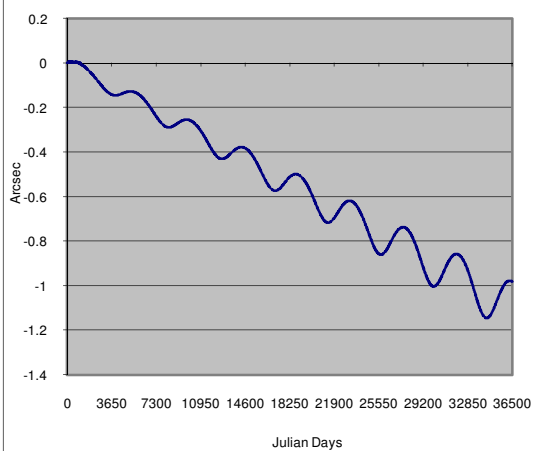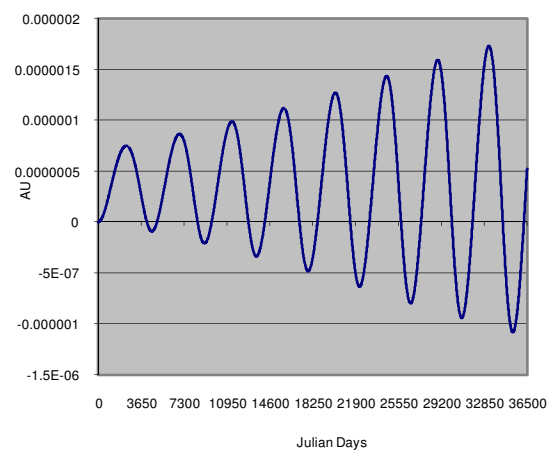
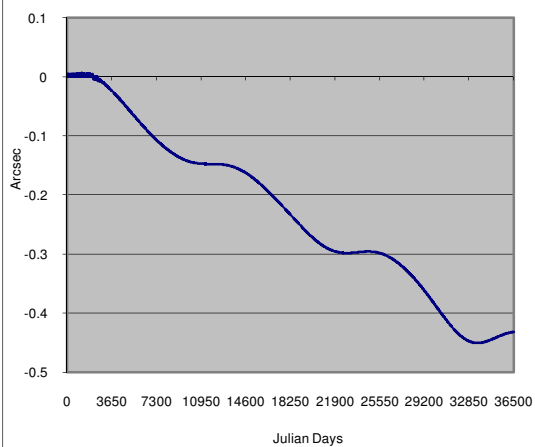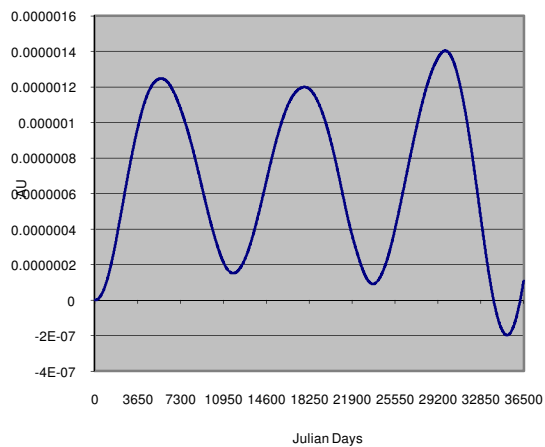DE405/Integrator Comparison (Earth)

DE405/Integrator Comparison (Earth)

DE405/Integrator Comparison (Moon)

DE405/Integrator Comparison (Moon)

DE405/Integrator Comparison (Mars)

DE405/Integrator Comparison (Mars)

DE405/Integrator Comparison (Jupiter)
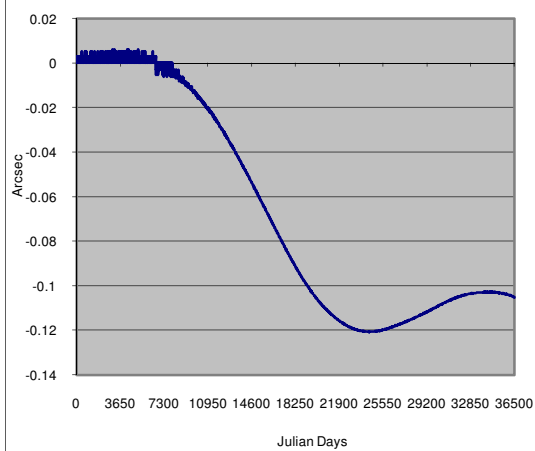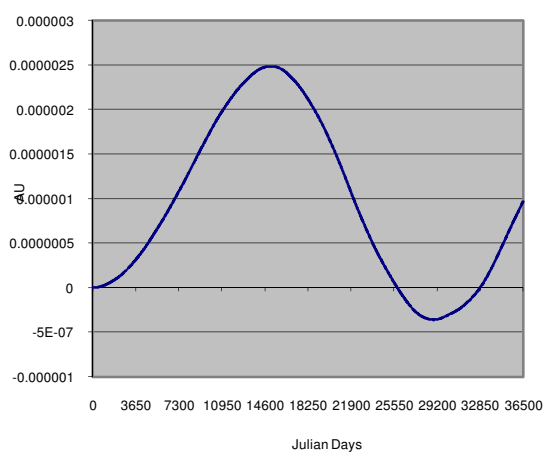
DE405/Integrator Comparison (Jupiter)

DE405/Integrator Comparison (Saturn)

DE405/Integrator Comparison (Saturn)

DE405/Integrator Comparison (Uranus)
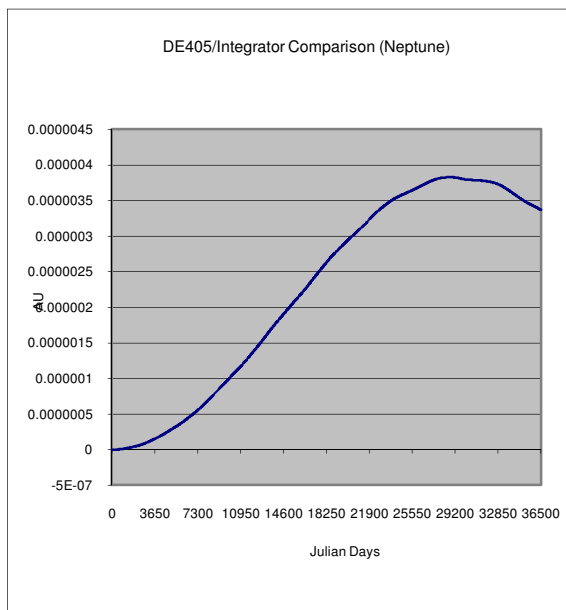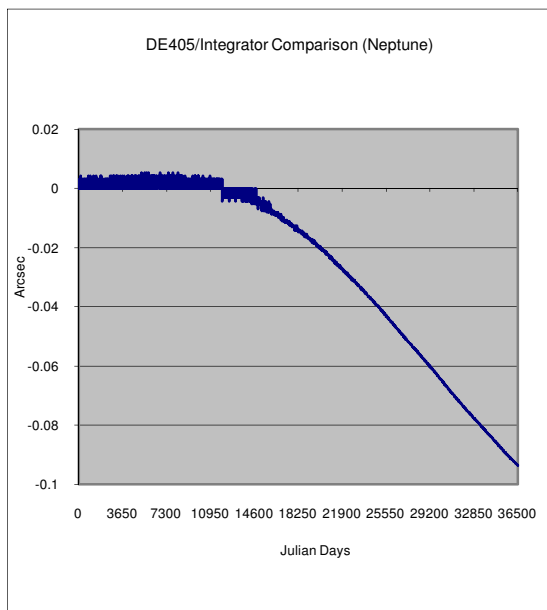

DE405/Integrator Comparison (Uranus)

DE405/Integrator Comparison (Neptune)

DE405/Integrator Comparison (Neptune)

Appendix D – Approach Direction from Bottke / Brown / Morbidelli Modelling

As discussed in Section 3.2, the NEA dynamical model of Bottke et al. (2002a), the fireball size frequency distribution and flux model of Brown et al. (2002), and the albedo model of Morbidelli et al. (2002a) are used to model the visibility of meteoroid objects in the hours prior to contact. An output of this modelling is the frequency distribution of the approach angles of the PFM population, shown in Figure D-1. The understanding of some unexpected asymmetries in this distribution could be considered for future work.
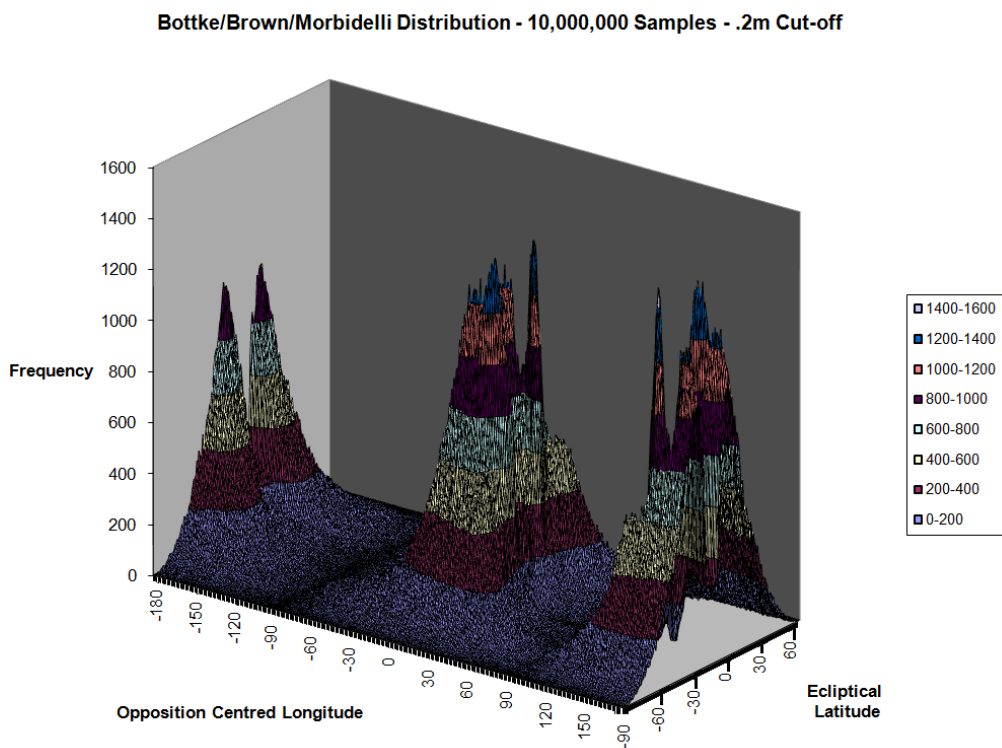

Figure D-1. A plot of meteoroid approach directions 4 hours prior to contact, as generated by Bottke/Brown/Morbidelli modelling. Frequencies by opposition centred longitude and ecliptic latitude are shown, assuming 10,000,000 colliding objects of diameter greater than .2 m. Of interest is the asymmetry in ecliptic latitude. These results require further investigation.

CURRICULUM VITAE

Name:	David L. Clark
Post Secondary Education and Degrees:	University of Waterloo Waterloo, Ontario, Canada 1974-1978 B.Math (Honours, Computer Science)
Honours and Awards:	Dean's List University of Waterloo 1978
Related Work Experience:	Research Assistant The University of Western Ontario 2007-2010